

MASTER OF SCIENCE THESIS

---

# Improving Spatial Resolution of Tomo-PIV using Particle Tracks with Vortex-in-Cell

Piyush Singh

---

22/08/2016

Faculty of Aerospace Engineering · Delft University of Technology



# **Improving Spatial Resolution of Tomo-PIV using Particle Tracks with Vortex-in-Cell**

MASTER OF SCIENCE THESIS

For obtaining the degree of Master of Science in Aerospace  
Engineering at Delft University of Technology

Piyush Singh

22/08/2016



Copyright © Piyush Singh  
All rights reserved.

DELFT UNIVERSITY OF TECHNOLOGY  
DEPARTMENT OF  
AERODYNAMICS

The undersigned hereby certify that they have read and recommend to the Faculty of Aerospace Engineering for acceptance a thesis entitled “**Improving Spatial Resolution of Tomo-PIV using Particle Tracks with Vortex-in-Cell**” by **Piyush Singh** in partial fulfillment of the requirements for the degree of **Master of Science**.

Dated: 22/08/2016

---

Prof. Dr. Ir. Fulvio Scarano

---

Dr. Ir. Knud Erik Meyer

---

Dr. Ir. Carlos Simao Ferreira

---

Ir. Jan Schneiders



---

# Abstract

Tomographic PIV is one of the most recent and advanced tools used in experimental fluid dynamics. Low spatial resolution is currently a problem in large scale tomo-PIV as well in conventional tomo-PIV experiments where certain flow regions have low seeding concentration.

A novel technique is proposed which leverages the temporal information of full Lagrangian particle tracks to improve the spatial resolution of tomo-PIV in low seeded flows. The method produces dense Eulerian velocity field from sparse scattered particle tracks obtained from state of the art particle tracking algorithms. The method is based on a variational principle wherein iterative simulations of Vortex-in-Cell method (Schneiders et al., 2014) are performed to minimise the norm of the difference between simulated and measured velocity of scattered particles. The LBFGS method, which is a gradient based numerical optimisation technique, is utilised to solve this optimisation problem. Gradient of the cost function with respect to the system's degree of freedom is computed using the adjoint method. Initial and boundary conditions are taken from tomo-PIV measurements.

A two dimensional analytical vortex blob is considered for the numerical validation of the proposed method. Both qualitative and quantitative analysis are performed for its detailed assessment. The method demonstrates significantly improved reconstructions as compared to methods which rely on instantaneous information of the particles. It is also revealed that utilising longer particle tracks within the methods framework further improves the reconstruction quality and spatial resolution. The method even shows significant noise reduction capability which enhances when using longer tracks.

The proposed method is also validated in an unsteady and evolving flow field by simulating the Von-Karman shedding in the wake of a long cylinder. Even at very low seeding densities the method successfully reconstructs the main structures of the flow. Providing more temporal information again proves to augment the methods ability to produce more accurate reconstructions.



---

# Acknowledgements

I would like to thank my primary thesis advisor Dr. Fulvio Scarano along with Ir. Jan Schneiders for providing me with an opportunity to work on this project having a nice blend of experimental and computational fluid dynamics. Thanks for consistently allowing me to freely apply myself to the work, but also steering me in the right direction whenever it was required. All the discussions were very motivating and helped me immensely in this work. I thank Jan for his frequent technical inputs throughout the thesis and also for helping me improve my programming skills.

I am grateful to my supervisor from DTU Dr. Knud Erik Meyer for his valuable comments and feedback during the course of this thesis. Special thanks to my friend Jorge Tamayo for helping me with the OpenFOAM simulations of the Von-Karman Shedding test case.

I am greatly indebted to Global Sustainable Electricity Partnership for providing me with the financial support required to carry out this masters study.

Thanks to all my friends for the pleasant moments spent together and creating the wonderful memories. Also, I especially thank my friend Sagar Zade for his support and the technical and general discussions during this work.

I must express my very profound gratitude to my parents for providing me with unfailing support and continuous encouragement. Finally I would like to thank the person whom I dedicate this thesis to, my wife Bhoomika. Thank you Bhoomi for being there and providing your love, care and unconditional support all through the thick and thin of life in these past couple of years.

Delft, The Netherlands  
22/08/2016

Piyush Singh



---

# Contents

<b>Abstract</b>	<b>v</b>
<b>Acknowledgements</b>	<b>vii</b>
<b>List of Figures</b>	<b>xv</b>
<b>List of Tables</b>	<b>xvii</b>
<b>1 Introduction</b>	<b>1</b>
<b>2 Particle Image Velocimetry</b>	<b>5</b>
2.1 Fundamentals of PIV . . . . .	5
2.2 Development of PIV . . . . .	7
2.3 Working of PIV . . . . .	7
2.4 Tracer Particles . . . . .	8
2.4.1 Mechanical Properties and Flow Characteristics . . . . .	9
2.4.2 Light Scattering Properties . . . . .	10
2.5 Light Source . . . . .	10
2.6 Stereoscopic PIV . . . . .	11
2.6.1 Limitations of Stereoscopic PIV . . . . .	11
2.7 Tomographic PIV . . . . .	12
2.7.1 Limitations of Tomo-PIV . . . . .	14
2.8 Large Scale Tomo-PIV . . . . .	15
2.9 Particle Tracking Velocimetry . . . . .	16
2.9.1 Limitations of PTV . . . . .	16
<b>3 State of the Art of Processing Techniques</b>	<b>17</b>
3.1 PIV Processing . . . . .	17
3.2 PTV Processing . . . . .	17
3.3 Scattered Measurement to Grid Data . . . . .	18
3.4 PIV with PTV . . . . .	18

3.5	Solenoidal Flow . . . . .	18
3.6	Navier-Stokes to Fill Gaps in PIV Data . . . . .	19
3.7	Variational Methods and PIV . . . . .	19
3.8	Numerical Optimisation Methods . . . . .	20
<b>4</b>	<b>Vortex-in-Cell</b>	<b>21</b>
4.1	Vortex Methods . . . . .	21
4.1.1	Point Vortex . . . . .	22
4.2	Vortex-in-Cell . . . . .	24
4.2.1	Applications of VIC . . . . .	25
4.2.2	Time Super-Sampling (Pouring Space in Time) . . . . .	25
4.3	VIC+ (Pouring Time in Space) . . . . .	26
4.4	Literature Survey Conclusion . . . . .	27
<b>5</b>	<b>Proposed Method</b>	<b>29</b>
5.1	Theoretical Background . . . . .	29
5.2	Working Principle and Numerical Implementation . . . . .	30
5.2.1	One Time Step . . . . .	31
5.2.2	Multiple Time Step (VIC++) . . . . .	33
5.3	Adjoint Method . . . . .	36
5.3.1	Adjoint Method vs Finite Difference Method . . . . .	37
<b>6</b>	<b>Numerical Assessment</b>	<b>39</b>
6.1	Analytical Vortex Blob . . . . .	39
6.2	Particle Tracks . . . . .	41
6.3	Reconstruction and Error Determination . . . . .	42
6.4	Linear Interpolation, AGW and PIV . . . . .	43
6.5	Grid Size Selection . . . . .	44
6.6	Boundary Conditions . . . . .	45
6.7	Numerical Assessment . . . . .	46
6.8	Comparision of Velocity Profiles . . . . .	51
6.8.1	Linear Interpolation vs VIC++ . . . . .	51
6.8.2	Short vs Long Tracks . . . . .	52
6.9	Tracer Concentration . . . . .	52
6.10	Time Length . . . . .	53
6.10.1	Time Length with Different Grid Size . . . . .	54
6.11	Initial Conditions . . . . .	54
6.12	Analysis with Noisy data . . . . .	57
<b>7</b>	<b>Unsteady Flow Regime</b>	<b>59</b>
7.1	Two Dimensional Cylinder Vortex Shedding . . . . .	59
7.2	Computational Simulation . . . . .	61
7.3	Analysis . . . . .	63
7.3.1	Numerical Assessment with VIC++ . . . . .	63
<b>8</b>	<b>Conclusions and Recommendations</b>	<b>69</b>
8.1	Conclusions . . . . .	69
8.2	Recommendations for Future Work . . . . .	71

References

73

References

73



---

# List of Figures

1.1	Image strips of experiments at different seeding densities (reproduced from Scarano (2013b)) . . . . .	2
2.1	Schematic diagram of PIV system (reproduced from Scarano (2013a)). . .	6
2.2	Jet Flow (a) Flow visualisation, inhomogeneous seeding (b) PIV, homogeneous seeding (reproduced from Westerweel (1997)). . . . .	6
2.3	Cross correlation of two images . . . . .	7
2.4	Tracer particle displacement. (a) Ideal case with same fluid and tracer velocities (b) Real case with some slip between tracer and fluid (reproduced from Sciacchitano (2014)) . . . . .	8
2.5	Schematic diagram of stereoscopic PIV . . . . .	11
2.6	Working of tomo-PIV with images show sequence of the flow field reconstruction (reproduced from Westerweel et al. (2013)). . . . .	12
2.7	Turbulent wake of a flow over a cylinder (reproduced from Scarano and Poelma (2009)). . . . .	13
2.8	Transitional jet captured by time resolved (4D) tomo-PIV. (reproduced from Scarano et al. (2010)). . . . .	13
2.9	Large Scale tomo-PIV setup. Magnified image shows very low seeding density behind the cylinder (adapted from Sacrano et al. (2015)). . . . .	16
3.1	(Left) Identifying gappy region of a PIV experiment performed to investigate an aerofoil. (Right) Filled data with incompressible Navier stokes solver (reproduced from Sciacchitano et al. (2012)) . . . . .	19
3.2	Lower error at initial time instant when assimilating longer measurements (reproduced from Yegavian et al. (2015)) . . . . .	20
4.1	vortex particle advection (left), Initialisation of particle at each time step with shaded area assigned to the black particle (right) (reproduced from Schneiders et al. (2014)). . . . .	24

4.2	Working principle of time super-sampling. (Top) Using measurements at two time instances to produce time slices between them. (Bottom) Time series creation from instantaneous flow field (reproduced from Schneiders et al. (2014)). . . . .	26
4.3	Isosurfaces of Q-Criterion reconstructed using various methods for different seeding concentrations $C$ (particles/ $\delta_{99}^3$ ); (a) DNS reference, (b) PIV, (c) Linear interpolation, (d) AGW, (e) Divergence free regression, (f) VIC+ (reproduced from Schneiders et al. (2015)). . . . .	27
5.1	Schematic diagram of an PTV Lagrangian track and the information used (red) by different methods for reconstruction reconstruction. (a) Linear interpolation (b) VIC+ (c)VIC++ (reproduced from Schneiders et al. (2016)).	30
5.2	Flowchart of the proposed method (reproduced from Schneiders et al. (2016)). . . . .	30
5.3	Schematic diagram of the grid nodes (blue) and the particle positions (red). Contribution of the node $(x_3, y_3)$ depends on $l_x$ and $l_y$ . . . . .	32
5.4	Algorithm of proposed method involving one time step . . . . .	34
5.5	Algorithm of the full VIC++ method . . . . .	35
5.6	Variation of gradient computation time for VIC++ (2 snapshots) using finite difference method(green), adjoint code(red) with respect to the grid size . . . . .	37
5.7	Ratio of gradient computation time using finite differences to that using adjoint code for VIC++ (2 snapshots), varying with respect to the grid size	38
6.1	Profile of the $v$ component of velocity along the x-axis (left), Profile of the $u$ component of velocity along the y-axis (right) . . . . .	40
6.2	Vorticity distribution along the x-axis . . . . .	40
6.3	Reference velocity vector field (left), Analytical Vorticity (right) . . . . .	41
6.4	$u$ component of velocity (left) , $v$ component of velocity (right) . . . . .	41
6.5	Particle tracks with only rotational velocity (left), Particle tracks with rotational and translational velocity (right). . . . .	42
6.6	Damping on various grid size of 10,20 and 100 . . . . .	45
6.7	Padded Boundary Conditions (reproduced from Schneiders et al. (2016a))	46
6.8	Dirichlet Boundary Conditions . . . . .	46
6.9	$u$ component of velocity contours for 10 particles. (a) Analytical (b) Linear Interpolation (c) PIV (d) AGW and (e) to (i) VIC++ for $N_t = 2, 10, 20, 30, 40$ respectively . . . . .	48
6.10	$v$ component of velocity contours for 10 particles. (a) Analytical (b) Linear Interpolation (c) PIV (d) AGW and (e) to (i) VIC++ for $N_t = 2, 10, 20, 30, 40$ respectively . . . . .	49
6.11	Vorticity contours for 10 particles. (a) Analytical (b) Linear Interpolation (c) PIV (d) AGW and (e) to (i) VIC++ for $N_t = 2, 10, 20, 30, 40$ respectively	50
6.12	Comparison of linear interpolation (yellow) and VIC++ $N_t = 2$ (blue). Mean profile (line) along the central y-axis with standard deviation (shaded area) for (a) $u$ velocity (b) $v$ velocity (c) vorticity . . . . .	51

6.13	Comparison of VIC++ $N_t = 2$ (blue) and VIC++ $N_t = 40$ (red). Mean profile (line) along the central y-axis with standard deviation (shaded area) for (a) $u$ velocity (b) $v$ velocity (c) vorticity . . . . .	52
6.14	RMS error (normalised with peak velocity) with varying number of particles for different $N_t$ . . . . .	53
6.15	RMS error (normalised with peak velocity) with varying $N_t$ for different particle densities. . . . .	53
6.16	RMS error (normalised with peak velocity) with varying $N_t$ calculated on a Grid of 15 (left), 25 (right). . . . .	54
6.17	$u$ velocity contours with initial condition computed using linear interpolation. (a) analytical (b) Linear interpolation (c) VIC++ with $N_t = 2$ (d) VIC++ with $N_t = 10$ (5 particles). . . . .	55
6.18	$u$ velocity contours with zero initial condition. (a) analytical (b) Linear interpolation (c) VIC++ with $N_t = 2$ (d) VIC++ with $N_t = 10$ (5 particles). . . . .	56
6.19	Vorticity contours with white Gaussian noise.(a) analytical (b) Linear interpolation (c) PIV (d) AGW (e) VIC++ with $N_t = 2$ (f) VIC++ with $N_t = 10$ (1000 particles). . . . .	57
6.20	$u$ velocity contours with white Gaussian noise.(a) analytical (b) Linear interpolation (c) PIV (d) AGW (e) VIC++ with $N_t = 2$ (f) VIC++ with $N_t = 10$ (1000 particles). . . . .	58
7.1	Flow regimes in a flow around a circular cylinder in a steady flow (reproduced from Sumer and Fredsøe (1997)) . . . . .	60
7.2	Geometry used for the numerical computation . . . . .	61
7.3	Mesh used for the numerical computation . . . . .	61
7.4	Vortex contours of Von-Karman Vortex shedding. Also shown is the section of the flow to be used for the analysis. . . . .	62
7.5	$u$ velocity contours for 10 particles. (a) Numerical (b) Linear Interpolation (c) PIV (d) AGW and (e) to (h) VIC++ for $N_t = 2, 5, 10, 20$ respectively . . . . .	64
7.6	$v$ velocity contours for 10 particles. (a) Numerical (b) Linear Interpolation (c) PIV (d) AGW and (e) to (h) VIC++ for $N_t = 2, 5, 10, 20$ respectively . . . . .	65
7.7	vorticity contours for 10 particles. (a) Numerical (b) Linear Interpolation (c) PIV (d) AGW and (e) to (h) VIC++ for $N_t = 2, 5, 10, 20$ respectively . . . . .	65
7.8	$u$ velocity contours for 25 particles. (a) Numerical (b) Linear Interpolation (c) PIV (d) AGW and (e) to (h) VIC++ for $N_t = 2, 5, 10, 20$ respectively . . . . .	66
7.9	$v$ velocity contours for 25 particles. (a) Numerical (b) Linear Interpolation (c) PIV (d) AGW and (e) to (h) VIC++ for $N_t = 2, 5, 10, 20$ respectively . . . . .	66
7.10	vorticity contours for 25 particles.. (a) Numerical (b) Linear Interpolation (c) PIV (d) AGW and (e) to (h) VIC++ for $N_t = 2, 5, 10, 20$ respectively . . . . .	67
7.11	Mean $u$ velocity profile along the x-axis (at $y=0$ ) of AGW(red), VIC++ $N_t=2$ (green), VIC++ $N_t=20$ (blue) compared with the numerical solution(black). For 25 particles. . . . .	68



---

## List of Tables

6.1	Vortex blob test case simulation parameters . . . . .	47
7.1	Von-Karman shedding test case simulation parameters . . . . .	62
7.2	RMS error of different methods for 25 particles . . . . .	68



---

# Chapter 1

---

## Introduction

Richard Feynman said "Turbulence is the most important unsolved problem of classical physics". It has been described as one of the six most difficult problems of the millennium in mathematics. In order to understand the behaviour of turbulent fluid flow, many experimental and computational methods have been devised over the years. Particle image velocimetry emerged in the 1980s as a method of experimental fluid flow measurement and visualisation. It has gained a lot of popularity because of its non intrusive nature and the ability to measure instantaneous velocity over the entire cross-section of a fluid flow region (Adrian, 1991).

Planar PIV provides accurate two dimensional flow information simultaneously at over  $10^5$  nodes (Westerweel et al., 2013). But two dimensional information is not sufficient to gain the full understanding of the turbulent flows which evolve in the three dimensional space. Only two velocities and four velocity gradients can be determined using the planar PIV (Westerweel et al., 2013). To gain a more complete understanding of the complex turbulent flows, a three dimensional flow measurement technique is required. One of the most recent and advanced 3D PIV techniques is the tomographic PIV (tomo-PIV) (Elsinga et al., 2006). The technique provides all the three components of velocity of the flow in a measurement volume. The tracer particles in a flow are illuminated by a pulsed laser in a control volume. The intensity of the light scattered from the particles are captured by several cameras from different viewing angles simultaneously. Using the images 3D reconstruction of the particles is done and the velocity components are obtained by 3D cross correlation of two exposures.

The spatial resolution in tomo-PIV depends mainly on the concentration of the tracer particles in the flow, or in other words the seeding concentration. For getting a high spatial resolution a high seeding concentration is required, but it cannot be increased beyond a certain limit. This is because too much seeding concentration restricts the transmission of light in the seeded fluid causing the image contrast to go down, refer figure 1.1. Tomographic reconstruction in this case yields a lot of spurious reconstructions Elsinga et al. (2006) which subsequently causes the reconstruction quality to deteriorate.

The limited measurement volume available in tomo-PIV has restricted the technique's application in industrial wind tunnels. Recently helium filled soap bubbles (HFSB) are being used to perform large scale tomo-PIV experiments. Scarano et al. (2015) point out that the spatial resolution for large scaled tomo-PIV experiments with HFSB is mainly restricted by the limited HFSB production rate or seeding concentration in the control volume. Furthermore the increase in measurement volume for tomo-PIV results in the reduction of the maximum seeding concentration curbing its spatial resolution. Along with the aforementioned aspects resulting in low spatial resolution another factor is the existence of some portions of the flow such as vortices, flow near the walls of the test object etc., where it is quite difficult to get the required seeding concentration.

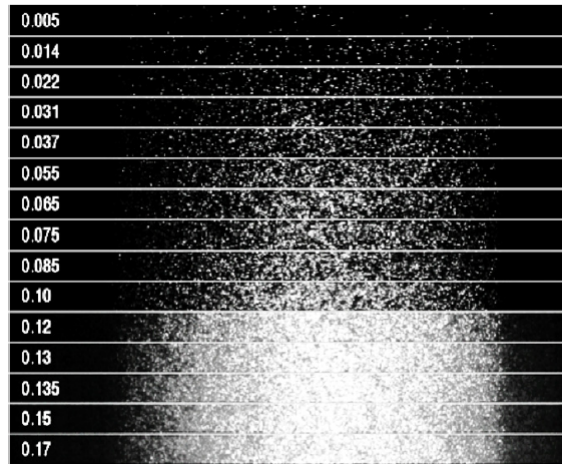


**Figure 1.1:** Image strips of experiments at different seeding densities (reproduced from Scarano (2013b))

Tomo-PIV requires on an average 5 to 10 particles in each interrogation box for good cross correlation (Scarano, 2013b). From these particle only one vector at the center of the interrogation box is generated causing spatial filtering. Flow Cases with low seeding density require large interrogation boxes resulting in further reduction in spatial resolution. The spatial filtering based on interrogation box size can be avoided using particle tracking velocimetry (PTV) which traces individual particles to form their Lagrangian tracks. Considering this aspect, PTV provides better spatial resolution, but the problem with it is that information is available only at positions where the tracer particles are present. Many post processing techniques require the data to be on a Eulerian grid. In order to extract the scattered information on a grid, interpolation techniques have to be utilised. Methods such as linear interpolation, adaptive Gaussian windowing, radial basis functions, splines etc. have been conventionally used for this purpose but they all suffer from spatial filtering. Also, all these methods are mathematical tools and do not impose any physics based constraints on the system.

One of the most recent and advanced method which increases the spatial resolution of tomo-PIV in the cases having limited seeding densities was proposed by Schneiders et al. (2015). The method provides physics based reconstruction of Eulerian velocity field using instantaneous velocity and temporal information of the flow in the form of its material derivative.

Although the material derivative does provide some temporal information, in no way it can be considered to account for full information of the development of flow in time. The present thesis explores the idea, whether providing more temporal information will help in achieving even higher spatial resolution. Thus instead of just using the material derivative the thesis involves devising a method that uses the full particle track information in the VIC+ framework (Schneiders et al., 2015). The proposed method envisages to pour the temporal information of PTV in the spatial domain of tomo-PIV.



# Particle Image Velocimetry

This chapter first introduces the fundamental concepts and working principle of PIV. The state of the art techniques evolved from PIV are discussed and their advantages and limitations analysed.

## 2.1 Fundamentals of PIV

There has been tremendous development in the field of PIV in the last three decades and over the years it has become one of the most used and researched measurement technique in fluid mechanics. The other popular measurement techniques such as hot wire anemometry and laser Doppler velocimetry have their own advantages such as the high signal to noise ratio and high temporal resolution, which has not yet been surpassed by PIV. But PIV has some major advantages of providing velocity vectors simultaneously at around  $10^3$  to  $10^5$  points, visualisation of flow and direct computation of spatial gradients (enabling calculation of vorticity).

The fundamental principle on which particle image velocimetry works is the computation of velocity of a moving particle by measuring its displacement and dividing by the respective time taken. The dynamics of a fluid is studied by putting small particles in the flow which represent the fluid itself and travel along with it without any significant intrusion. Introduction of the particles facilitates the quantitative investigation as well as provides means for qualitative flow visualisation. The movement of the particles is either captured by using single or multiple CCD or CMOS cameras. In order to make the particle visible, they are illuminated by a source of light usually in the form of a double head pulsed laser. Two consecutive images captured within a very short amount of time by the cameras are used to calculate the displacement of the particles, which further is used to compute the velocity of the flow field. The schematic diagram of a PIV system is presented in figure 2.1.

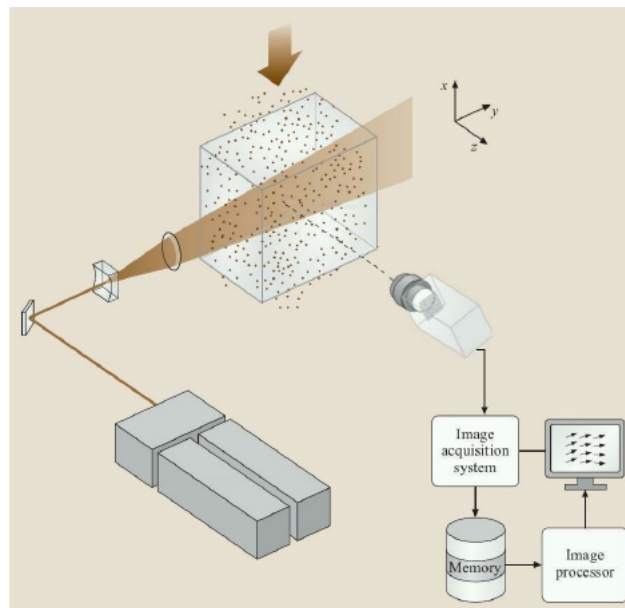


**Figure 2.1:** Schematic diagram of PIV system (reproduced from Scarano (2013a)).

PIV is essentially a non intrusive experimental technique and the overall experimental setup does not alter the fluid flow. But it does require optical access for both the laser to illuminate the measurement volume as well as the cameras to take images. Also as the measurement is performed indirectly using the tracer particles, they are required to be densely and evenly distributed throughout the domain, unlike some visualisation techniques which seed particles intermittently at specific intervals of space and time. Figure 2.2 (a) presents the inhomogeneous seeding used in a jet flow for visualisation while homogeneous seeding in figure 2.2 (b) for a PIV measurement. For the flow visualisation, the seeding is introduced at a particular location to view some specific structures in the flow.

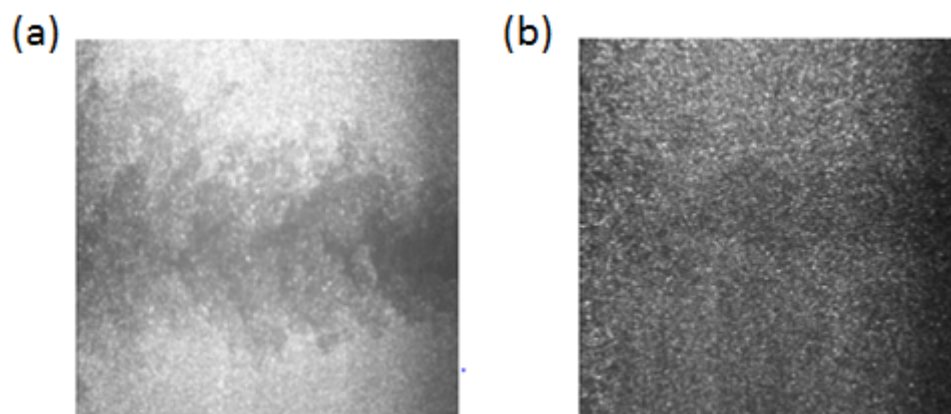


**Figure 2.2:** Jet Flow (a) Flow visualisation, inhomogeneous seeding (b) PIV, homogeneous seeding (reproduced from Westerweel (1997)).

## 2.2 Development of PIV

R J Adrian (1991) mentions that PIV is a subset of a general group called Pulsed Light Velocimetry, where in markers in a fluid flow are lighted by a pulsed source of light and captured on an "optical recording medium". The inception of modern PIV can be traced back to the work of Meynart (1983). The early 1990s saw the introduction of digital particle image velocimetry. High speed lasers and evolved imaging sensor such as CMOS sensor technology lead to the development of time resolved PIV with acquisition frequency reaching up to  $10\text{KHz}$ . The early PIV experiments were performed in a planar domain which was later extended to two dimensional three component system called stereoscopic PIV (Willert, 1997)(Prasad, 2000). Further developments came in the form of tomographic PIV (Elsinga et al., 2006) which is a three dimensional three component system. Introduction of time resolved tomo-PIV added another dimension to the evolving method. For a detailed review the reader is referred to Raffel et al. (2007), Westerweel et al. (2013), Adrian et al. (2005) among others.

## 2.3 Working of PIV

The two images taken between the time interval  $\Delta t$  are divided into numerous sub-domains. These sub-domains or sections are called interrogation windows. The division is followed by a spatial cross-correlation analysis of the respective windows of each image. The distance of the peak of the cross-correlation maps from the center of the interrogation window gives the displacement of particles. The displacement evaluation principle can be seen in figure 2.3.

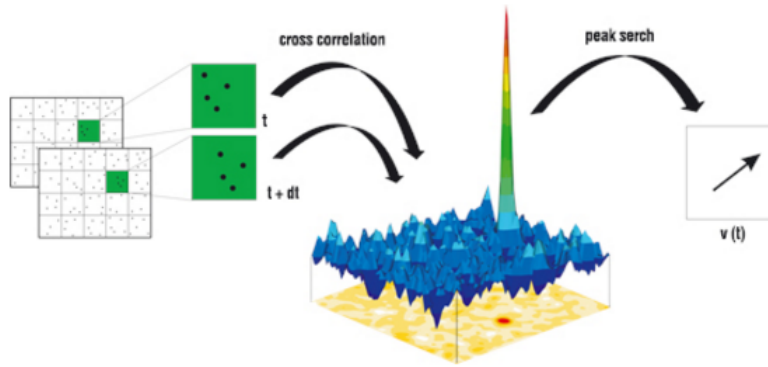


**Figure 2.3:** Cross correlation of two images

As formulated by Westerweel(1997), the displacement of the tracer particles in the time interval  $\Delta t$  is given by

$$D(x, t_1, t_2) = \int_{t_1}^{t_2} v(x, t_1, t_2) dt \quad (2.1)$$

where  $t_2 - t_1 = \Delta t$ ,  $v$  is the tracer particle velocity. For an ideal case the tracer velocity is equal to the fluid velocity  $u(x,t)$ . When the displacement  $D$  is known or in this case measured, the tracer velocity can be calculated by equation (2.2). This velocity is not the instantaneous velocity of the particle at  $t_1$  but rather the averaged velocity over  $t_1$  to  $t_2$ .

If  $\Delta t$  is sufficiently small, or the fluid particle may be assumed to have zero acceleration within this time frame, then it can be conveniently approximated as the instantaneous velocity at  $t_1$  (Sciacchitano, 2014) (Westerweel, 1997).

$$v(x, t_1) \approx \frac{D(x, t_1, t_2)}{\Delta t} \quad (2.2)$$

Figure 2.4 (a) demonstrates the ideal case where the tracer particle is perfectly following the fluid while figure 2.4 (b) shows the practical case where there is some slip between the particle and the fluid. The practical case is suitably represented by equation (2.3). The existing error  $\epsilon$  largely depends on the selection of the tracer particle. It can be negligible or significant based on the tracer particle dynamics and the exposure time between the two images compared to the temporal and spatial scales of the flow. More on this can be read in the work by Adrian (1995).

$$\|D - u\Delta t\| < \epsilon \quad (2.3)$$

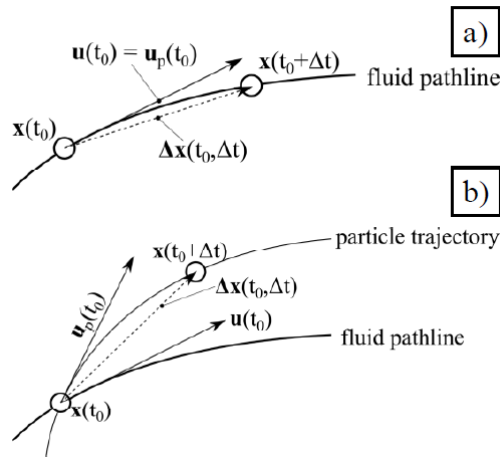


**Figure 2.4:** Tracer particle displacement. (a) Ideal case with same fluid and tracer velocities (b) Real case with some slip between tracer and fluid (reproduced from Sciacchitano (2014))

## 2.4 Tracer Particles

The dependency of PIV on tracer particles to get measurements makes the choice of right particles very important for a successful experiment. It is desired that the disparity between motion of the fluid and tracer particle be kept to a minimum. Apart from the required dynamics of tracers, its light scattering abilities are also equally important to facilitate their detection through the cameras. Some of the other important properties of a tracer particle is that it should not chemically react and alter the fluid properties in any way as well as they should not interact among themselves. The following subsections present a brief discussion on the mechanical and light scattering properties of the seeding particles.

### 2.4.1 Mechanical Properties and Flow Characteristics

Movement of small particle in a fluid is influenced by many forces such as quasi-steady viscous force (stokes drag), gravitational force, electrostatic force etc. For a small particle in a fluid, all forces except the quasi-steady viscous force are negligible. Melling (1997) discusses that the particle dynamics is highly dominated by the stokes drag force and there in the involved properties such as particle diameter  $d_p$ , particle density  $\rho_p$ , fluid density  $\rho$  and fluid dynamic viscosity  $\mu$ . The difference in velocity of the fluid and tracer in a continuously accelerating fluid can be modelled as equation (2.4).

$$u_s = v - u = d_p^2 \frac{(\rho_p - \rho)}{18\mu} \frac{dv}{dt} \quad (2.4)$$

where  $u_s$  is called as the slip velocity. Ideally it is desired that the right hand side of the equation (2.4) is zero so as to make the fluid and particle velocity same. In order to do so or bring it close to zero, two conditions are possible, first the acceleration of the particle is zero i.e.  $\frac{dv}{dt} \approx 0$ . This means that the fluid velocity is steady and for turbulent flows this is impossible, hence would not be discussed further. The second possibility is that the particle is neutrally buoyant which means that  $\frac{(\rho_p - \rho)}{\rho} \ll 1$ . Satisfying the neutrally buoyant condition would result into high fidelity fluid tracking by the tracer particle.

When considering heavy particles in fluid, analogous to the particle immersion in gas flows where particle density is almost two order of magnitude higher than the surrounding fluid, it is evident that particles are far from neutrally buoyant. Hence it is necessary to further look into the response of particle motion with respect to the fluid. For a heavy particle if the fluid velocity suddenly rises to  $u$  from zero then the particle does not attain that velocity immediately and for the step signal it has an exponential response with its velocity varying according to equation (2.5) Raffel et al. (2007).

$$v(t) = u \left( 1 - \exp\left(-\frac{t}{\tau_s}\right) \right) \quad (2.5)$$

$$\tau_s = d_p^2 \frac{(\rho_p - \rho)}{18\mu} \quad (2.6)$$

where  $\tau_s$  is the relaxation time and can be viewed as the ability of particle to track the fluid. As the particle density is very large in comparison to that of the fluid, equation (2.6) can be fairly approximated as

$$\tau_s = d_p^2 \frac{\rho_p}{18\mu} \quad (2.7)$$

The relaxation time  $\tau_s$  is the time required by the particle to reach 63% of the change in velocity of the fluid from  $u_1$  to  $u_2$ . It is required to be kept as low as possible for the high fidelity fluid tracking. It is evident from equation (2.7), that a particle with small diameter has lower relaxation time and is able to follow the flow more faithfully as compared to a particle with same density and higher diameter. The diameter of the

tracer cannot be reduced too much as it would result in the reduction of light scattering properties of the particle. A trade-off between the two aspects has to be made. For a more detailed discussion the reader is referred to Melling and Whitelaw (1973), Humphreys et al. (1993), Meinhart et al. (1993).

The condition of neutral buoyancy is comparatively easy to achieve in high density fluids such as liquids while it is very difficult to achieve in case of gases. The typical range of particles used in gases is  $0.5\mu m$  to  $5\mu m$ , while in liquids particles up to  $500\mu m$  have been used.

#### 2.4.2 Light Scattering Properties

Tracer particles seeded in a flow can only be used to extract information from the fluid flow if they are properly captured by the image acquiring system. A particle having very small relaxation time and high tracking fidelity will be rendered useless if its not able to sufficiently scatter the light it receives from the light source.

The contrast between the illuminated particles and the background is an important factor in dictating the accuracy of PIV. The contrast of an image increases with rise in the scattered light intensity. The scattering properties of a particle depends on a few factors such as its size, shape, relative refractive index of particle to the fluid and the light source. It is also heavily dependent on the direction of reception or observation of the scattered light. Mie's light scattering theory (Mie, 1908) is applicable for particles having diameter larger than the wavelength of illuminating source. According to the findings of the theory larger particle have better scattering properties and contribute to increase in scattered light intensity. Also material having high relative refractive index with respect to the fluid have increased scattering efficiency. The most favourable observation direction is the forward direction of the incoming light source because its intensity is very high as compared to the other direction. Limitations such as the inability to capture depth of the measurement field and problems with optical access render the use of other directions more feasible as compared to the forward direction.

### 2.5 Light Source

The most common illumination sources used in PIV are the double head pulsed laser systems. The lasers provide high intensity, collimated, monochromatic light which can be easily shaped to form sheets acting as the measurement domain. The pulse energy provided by the laser must be such that the scattered light intensity captured by the imaging systems provides sufficient particle to background contrast. The pulse duration of the light source must be much smaller than the time taken by particle to be displaced by a length equivalent to its diameter. This ensure that the particles are imaged as distinct spots rather than streaks.

The Nd:YAG (Neodymium-doped yttrium aluminium garnet) laser is the commonly used source of light for PIV experiments. It has a wavelength of  $532nm$  and pulse energy production lies in the range of  $10mJ$  to  $1J$ . The repetition rate of these lasers are generally less than  $50Hz$ , which is insufficient to perform time resolved PIV experiments. The Nd:YLF (Neodymium-doped yttrium lithium fluoride) have been developed which have very high repetition rate of up to  $5KHz$ , at the cost of reduced pulse energy reaching up to  $30mJ$ .

## 2.6 Stereoscopic PIV

The discussion in the above sections has made it clear that with planar PIV one can only evaluate two components of the velocity field. Moving a step further from the 2D realm of planar PIV, stereoscopic particle image velocimetry was developed (Arroyo & Greated, 1991)(Willert, 1997)(Prasad & Adrian, 1993). The method adds another dimension to the information available on a plane. It is a direct extension of planar PIV obtained by collaborating it with stereoscopy. Two cameras are used to capture images of laser sheet from different viewing angles. By doing this the  $z$  velocity is extracted along with the  $x$  and  $y$  velocity on the measurement plane. For a more detailed review and study on the working principles of the method, reader is referred to Prasad (2000). The schematic diagram of stereo PIV is shown in figure 2.5

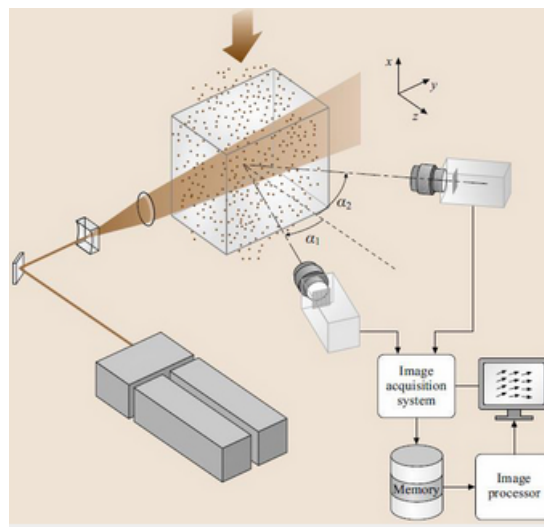


**Figure 2.5:** Schematic diagram of stereoscopic PIV

Stereoscopic PIV enables the calculation of the velocity gradients in the  $x$  direction and the  $y$  direction but as the  $z$  component of velocity is available on a plane, the gradient along the  $z$  direction cannot be obtained. To cater to this issue multi plane stereoscopic PIV was developed (Kähler & Kompenhans, 2000). This method performs stereoscopic PIV on two (Mullin & Dahm, 2005) or multiple parallel planes simultaneously, enabling the computation of the velocity gradient in the out of plane direction.

### 2.6.1 Limitations of Stereoscopic PIV

The limitation of this method is that even though all the components of velocity and their gradients can be computed, they are still computed in a planar domain. For many physical flows acquiring information on a plane is not sufficient to get full understanding of its dynamics. For reconstruction of full 3D domain, Taylor's frozen turbulence hypothesis has to be made and it has to be assumed that the turbulent structures don't vary spatially between the two laser sheets. Scarano (2013) very nicely explains the problem of high reliability of stereoscopic PIV on assumptions, by an analogy stating "The impaired measurement may be compared to that of estimating the properties of a living animal

from its footprints, hearing its voice or echo or watching its shadow projected on the wall". Moreover, the optical arrangement in a multiple plane PIV is more complicated because of the involvement of lasers with different polarisations, illuminating parallel planes.

## 2.7 Tomographic PIV

Tomographic PIV is a three dimensional measurement technique developed by Elsinga et al. (2006), which essentially computes all the velocity components of a flow along with the respective gradients by producing a three dimensional flow field.

The technique involves illumination of a seeded measurement volume with a pulsed laser by increasing width of the laser sheet. The light scattered by the seeded particles are captured using multiple cameras (generally 4) from different viewing angles. The image pairs captured by each camera are utilised by the reconstruction algorithm to reconstruct a virtual three dimensional volume with distributed light intensities. The physical and image space require to be related in order to perform the three dimensional reconstruction. For this a calibration procedure is adopted in line with that of the stereoscopic PIV but requiring a higher precision (less than 0.1 pixels). The reconstructed volumes are then divided into small interrogation volumes, analogous to the interrogation window in planar PIV. The volume pairs are then cross-correlated leading to the computation of the three dimensional velocity field. Figure 2.6 presents the schematic diagram of a typical tomo-PIV system. Also can be seen is the flow chart of its fundamental working principle.

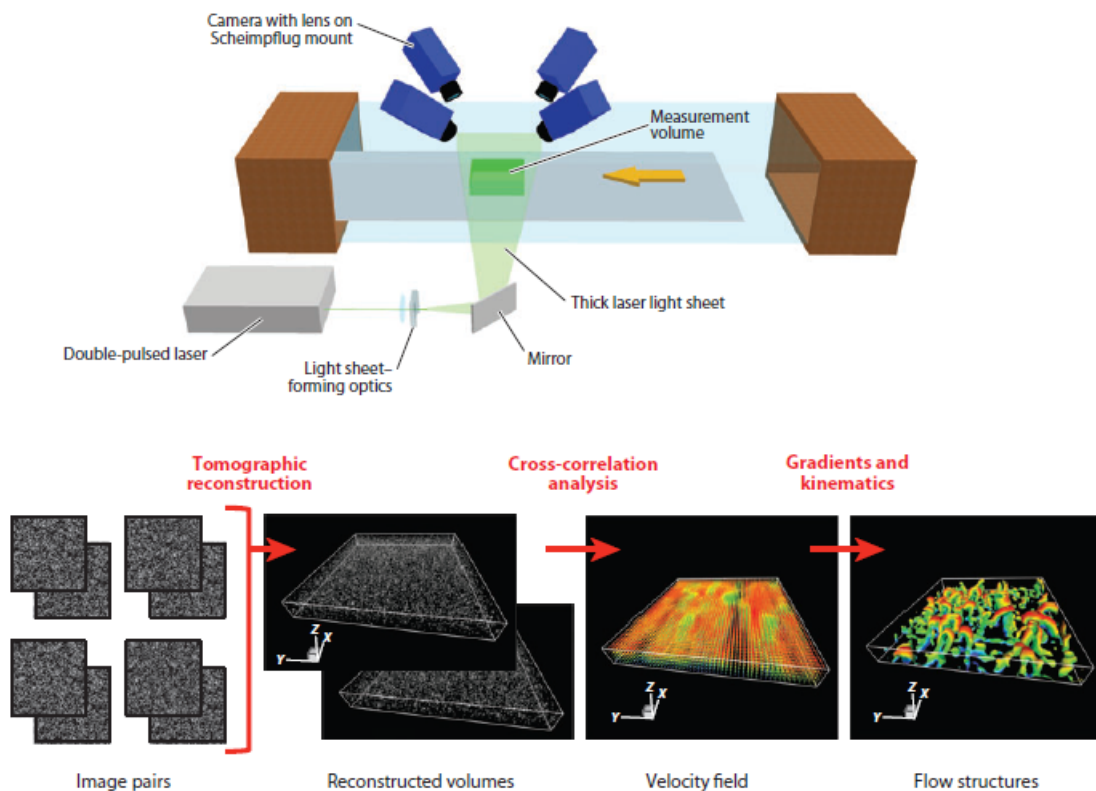


**Figure 2.6:** Working of tomo-PIV with images show sequence of the flow field reconstruction (reproduced from Westerweel et al. (2013)).

The main novelty of this measurement technique is the development of an algorithm to reconstruct the 3D object space by optical tomography (Scarano, 2013b). Elsinga et al. (2006) developed an iterative algorithm named multiplicative algebraic reconstruction technique (MART) to solve the reconstruction problem at hand. This was followed by the development of various modified versions of this method in the coming years. The entire light intensity distribution in the 3D space is discretised and represented by voxels which are synonymous to the pixels used in planar space. The particles constitute only a fraction of the measurement volume and hence there are a very small number of voxels which carry non zero intensity values, rendering more than 90% of the voxels having zero intensity Westerweel et al. (2013). To take advantage of this phenomenon methods like MFG (multiplicative first guess) (Worth & Nickels, 2008) and MLOS (multiplicative line of sight) (Atkinson et al., 2008) were developed. These methods provide single step solution with a lot of computational advantage over MART but the acceptable accuracy is obtained for only low particle density. The low particle density invariably reduces the spatial resolution of the results. These methods have been developed to be used along with MART (MLOS-SMART) to enhance the computational speed considerably, keeping the accuracy similar to the conventional MART algorithm.

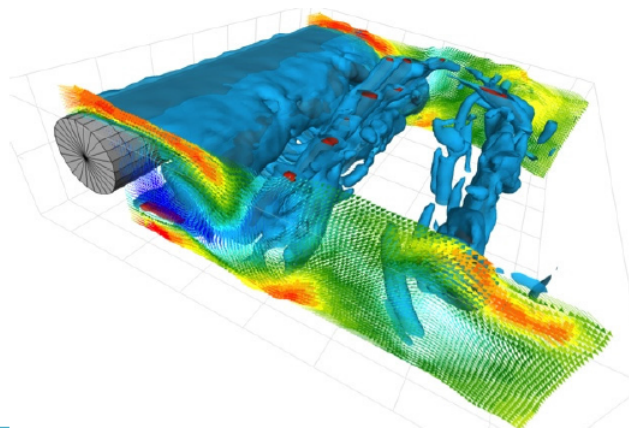


**Figure 2.7:** Turbulent wake of a flow over a cylinder (reproduced from Scarano and Poelma (2009)).

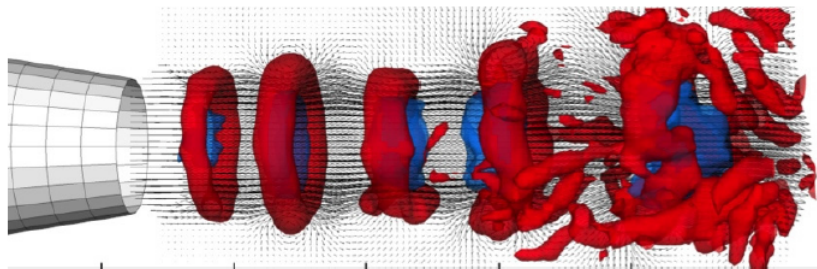


**Figure 2.8:** Transitional jet captured by time resolved (4D) tomo-PIV. (reproduced from Scarano et al. (2010)).

Since its inception, the technique has been widely used in experimental fluid mechanics.

High speed lasers and image capturing systems have made it possible to perform time-resolved tomo-PIV experiments. Tomo-PIV has been used to perform wide range of experiments such as flow over bluff bodies and study of their turbulent wakes (Scarano and Poelma, 2009), (Heine et al., 2011), (David et al., 2011), turbulent boundary layers (Gao et al., 2010), (Humble et al., 2009), (Amili et al., 2009), (Ghaemi et al., 2012), transitional jets (Violato et al., 2011), (Scarano et al., 2010), (Schmid et al., 2012). For a detailed review on the applications and development of the technique, the reader is referred to Scarano (2013), Westerweel et al. (2013).

### 2.7.1 Limitations of Tomo-PIV

Some of the initial drawbacks of tomo-PIV were the requirement of a complicated and highly precise calibration system and large processing time required for the image reconstruction. Both these issues have received ample attention with the former being dealt with the introduction of volume self calibrated technique by Wieneke (2007, 2008). In order to reduce the computational cost, various adaptations of MART such as MLOS-SMART were developed as discussed above. The reconstruction accuracy has also been researched upon and many post-processing techniques have brought significant improvement to it. More on this will be discussed in next chapter.

Even after the great development, tomo-PIV has not been used for industrial applications yet, mainly due to availability of limited measurement volume. The typical measurement volume used in tomo-PIV with high acquisition frequency (1 KHz) ranges below  $100\text{cm}^3$  (Scarano et al., 2015). This scale is mostly suitable for academic studies rather than being used in the industry. Two main factors contributing to this limitations are the image source density and laser pulse energy.

### Image Source Density

The seeding density (particle per pixel) directly affects spatial resolution of a PIV experiment. The spatial resolution of tomo-PIV is lower as compared to that of planar PIV due to the limited number of tracer particles present in the domain. A more general parameter compared to seeding density, which does not depend on particle size is image source density ( $N_s$ ). It is defined as the fraction of the image occupied by the particles. For a four camera system, accurate reconstruction can be done for  $N_s < 0.5$  as reported by Novara et. al. (2010), Scarano (2013b). Beyond this limit transmission of light is offered significant hindrance which leads to the reduction of image contrast and thus the overall reconstruction accuracy.

The seeding concentration  $C$  (*particles/mm<sup>3</sup>*) relates to the image source density  $N_s$ , as given in equation (2.8). When the measurement volume is increased getting the same concentration

$$C = \frac{N_s \cdot D_r^2}{W} \frac{4}{\pi d_\tau^* 2} \quad (2.8)$$

where  $W$  is the width of measurement volume,  $D_r$  is the digital image resolution and  $d_\tau^*$  is the pixel normalised particle image diameter. For a particular type of seeding and image condition, the seeding concentration is directly proportional to the image source

density and inversely proportional to the measurement volume (for a particular length and breadth of measurement). Because of the limit on the image source density, the seeding concentration has to be reduced for an increasing measurement volume. This causes the reduction of available spatial resolution.

### Laser Pulse Energy

The laser pulse energy is also a major factor contributing to the restriction of measurement volume of tomo-PIV. For a same source of illumination, its pulse energy decreases with the increase in volume. Increasing the measurement volume by 100% decreases the peak particle intensity by one order of magnitude (Scarano et al., 2015). The laser repetition rate is inversely proportional to the pulse energy, hence experiments performed with larger measurement volume have lower temporal resolution. For conventional tomo-PIV experiments a solution was developed in the form of application of multi-pass light amplification system (Ghaemi & Scarano, 2010). Larger volume again pose problems for the present laser systems available. One solution to the issue of low illumination intensity in large volume is the introduction of particles having enhanced light scattering properties. Helium filled soap bubbles is one such particle. More on this is described in the next chapter.

## 2.8 Large Scale Tomo-PIV

Large scale tomo-PIV has been recently gaining a lot of attention from the scientific community and its development mainly aim towards making the measurement technique feasible for industrial use. Recently Helium filled soap bubbles (HFSB) have been proposed (Scarano et al., 2015) to be used for large scale tomo-PIV experiments. Scarano et al. (2015) performed time resolved tomo-PIV experiment (greater than 1KHz) for a volume of  $4800\text{cm}^2$ , which is significantly higher compared to other time resolved experiments done till date. They did this by devising a HFSB seeding device which produces tracers at an increased seeding rate. Earlier Kühn et al. (2011) also used HFSB with very large volume, but the experiment was performed in an enclosure. Large scale tomo-PIV is also recently being utilised in the field of sports aerodynamics Sciacchitano et al. (2015), marking the bright future which lies ahead for the method.

Scarano et al.(2015) report that the reconstructed velocity field in the wake of cylinder suffers from low spatial resolution. Although bigger turbulent structure are visible, the smaller sub-structures are filtered out. The reason for this was concluded as low seeding density ( $< 0.01\text{ppp}$ ) achieved in the experiment. This can be viewed in the figure 2.9. The magnified part of the figure specifically shows wake of the cylinder where hardly any particles are seen. With very low seeding densities, larger interrogation windows are required for the cross-correlation process, leading to the spatial filtering. In this study it was shown that the limit on the seeding production rate is currently dictating increase in the tomo-PIV measurement volume.

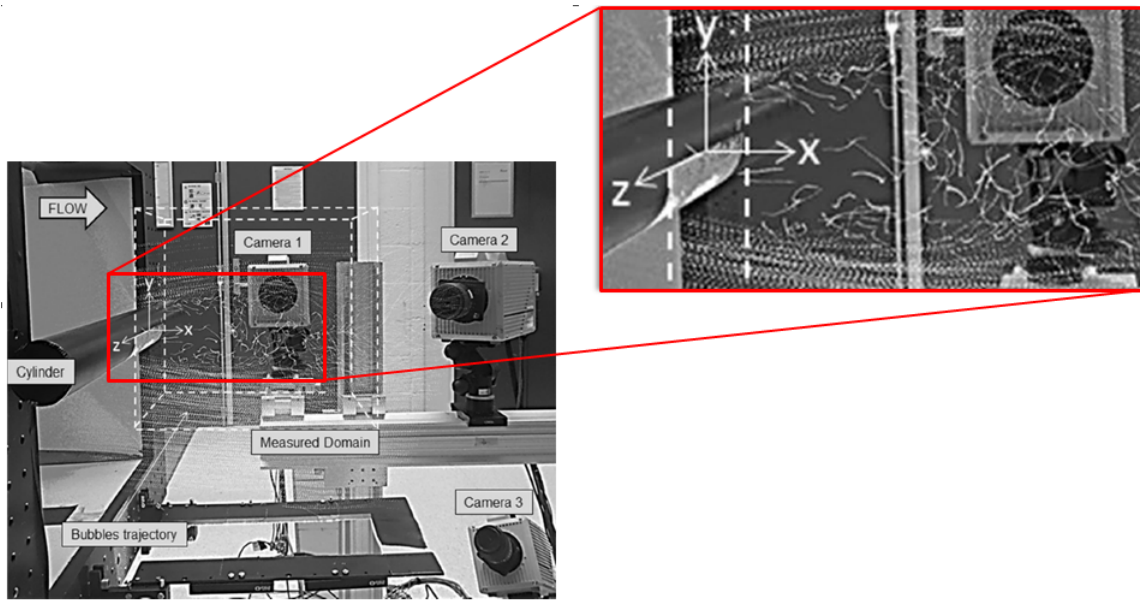


**Figure 2.9:** Large Scale tomo-PIV setup. Magnified image shows very low seeding density behind the cylinder (adapted from Sacrano et al. (2015)).

## 2.9 Particle Tracking Velocimetry

Particle tracking velocimetry is a measurement technique used to track individual particles in a seeded flow and compute their velocities. It follows a Lagrangian approach while PIV follows a Eulerian approach, by calculating velocities on a grid. Three dimensional PTV was introduced in the early nineties (Malik et al., 1993). The method triangulates the position of the particle positions and between two consecutive images, matching occurrences of the particles is formed, thus creating the Lagrangian tracks.

The main advantage with this technique is that it avoids any interrogation based spatial filtering observed in PIV. As the principle of the computation of velocity in PTV does not use cross correlation, the spatial smoothing is prevented. The existence of spurious particles in the reconstruction is largely limited by the method.

### 2.9.1 Limitations of PTV

The Lagrangian nature of the method allows it to provide information only at the particle locations. Thus data cannot be produced directly on a grid, but is done through an interpolation technique. This results in the reduction of spatial resolution. Malik et al. (1993) note that low particle spacing to displacement hinders the particle identification and tracking capability of PTV. This means that large spacing between particles is required which means that the allowable seeding density remains to be very low ( $< 0.005ppp$ ). The maximum seeding density is almost one order of magnitude lower than tomo-PIV. This results in low resolution as well. Currently some postprocessing techniques have been developed which have increased the capability of PTV to handle larger seeding densities. More on this is discussed in the chapter to follow.

# State of the Art of Processing Techniques

The current chapter deals with state of the art processing techniques for both PIV and PTV. The concept of combining the two methods to achieve higher spatial resolution is discussed in section 3.4. This is followed by a brief discussion on the application of numerical techniques such as CFD and variational methods in the realm of PIV. The numerical optimisation methods relevant to this thesis are also pondered over in the last section of this chapter.

### 3.1 PIV Processing

A novel technique of utilising the information contained in multiple images at various times to improve the reconstruction of intensities was introduced in the form of MTE-MART(motion tracking enhancement-MART) by Novara et al. (2010). SMTE(sequential motion tracking enhancement)(Lynch & Scarano, 2015) was later proposed to make MTE computationally efficient. Improvement in the correlation of time resolved tomo-PIV was shown by methods like FTC (fluid trajectory correlation) (Lynch & Scarano, 2012).

Conventional PIV methods use rectangular interrogation windows for cross-correlation. Some methods differed from the regular rectangular window size and adopted its elongated version to increase the spatial resolution in one direction (Scarano, 2003), (Theunissen et al., 2007). Wieneke and Pfeiffer (2010) developed the concept further and introduced the idea of window shape and size variation based on the quality of the image and the local velocity gradient in order to enhance the spatial resolution of reconstructed flow field.

### 3.2 PTV Processing

As discussed in section 2.9, the main problem with PTV has been its inability to handle large seeding concentrations. This has been convincingly dealt with in the recent advancements in the field. Schanz et al. (2014) developed a novel method named 'Shake the box'

which utilizes the temporal information of time resolved PTV to produce highly accurate particle tracks. It does not reconstruct the Lagrangian tracks from scratch but rather uses the 'Iterative particle reconstruction' method proposed by Wieneke (2012) as initial condition. The method produces accurate tracks for high seeding densities of the order that is used in tomo-PIV. The method seems to fail above very high seeding densities of  $0.125ppp$ . The method is reliable and does well as compared to the MLOS-SMART.

### 3.3 Scattered Measurement to Grid Data

The data from Particle Tracking Velocimetry is obtained at the particle locations. As the particles are randomly distributed throughout the measurement domain, the data obtained is also scattered. Now, many post processing softwares and tools require the data to be gridded. Data on a grid helps in better visualisation, ease of gradient calculation as well as facilitates simplification of other post-processing measures. Over the years many methods have been developed for the reconstruction of measured scattered data on a uniform grid. One of the most simplistic and trivial of them is the linear interpolation. A bit more advanced are the higher order polynomial interpolation schemes.

Adaptive Gaussian windowing was proposed by Agüí and Jiménez (1987). The method is quite popular and involves weighted averaging over all the vectors in the observation volume. The method has a disadvantage of smoothing or low pass filtering of the velocity field which in turn reduces the spatial resolution. Other interpolation schemes such as radial basis function interpolation (Casa & Krueger, 2013), splines also suffers from a similar problem of smoothing.

### 3.4 PIV with PTV

An important question which arises when studying PIV and PTV is: can their advantages be utilised together to negate their respective disadvantages? Meaning, whether the tracks produced by PTV can be utilised to increase spatial resolution of particle image velocimetry. This realm was first explored and the concept of super resolution was introduced by Keane et al. (1995), who used the combination of PIV and PTV in order to utilise the advantages of both the methods. This concept was further developed by Sitou and Riethmuller (2011) who proposed a 'hybrid PIV-PTV' method to address the issue of low spatial resolution in PIV. Recently Schneiders et al. (2015) utilised the temporal information available in time resolved tomo-PTV to increase the spatial resolution of data on grid. This method is discussed in more detail in chapter 4.

### 3.5 Solenoidal Flow

Tomo-PIV being a three dimensional measurement technique provides all the nine components of the velocity gradient. Incompressible flows are divergence free by the virtue of mass conservation and the physical constraint can only be applied in cases where all the velocity gradients are available. For planar PIV, the divergence free constraint is not always applicable as information on the out of plane component of velocity is not available.

There have been many advanced numerical techniques which leverage the property of solenoidal velocity flow field to reduce noise and enhance the reconstruction quality. Vedula et al. (2005) discuss an interpolation method working on a variational principle to

get a Eulerian flow field. They impose a regularisation term which ensures divergence free flow field. Azijli et al. (2014,2015) also devise a statistical regression method in order to analytically make the flow solenoidal and show results with better accuracy for methods with enforced divergence free constraint than without it.

### 3.6 Navier-Stokes to Fill Gaps in PIV Data

Sciachhitano et al. (2012) demonstrated a technique to fill the voids in PIV measurements by the use of full incompressible Navier-Stokes solver. The regions of the measurement gaps are selected and the information on the nodes computed through the Navier-Stokes solver. Figure 3.1 (left) shows an aerofoil with measurement gap created due to shadow of the object while the right figure shows the reconstructed field. It has been demonstrated by the author that the significant improvement over the conventional interpolation technique is provided by the method. As the finite volume Navier-Stokes solver required very small integration time steps, the boundary condition of the reconstruction domain have to be created by the advection model. The method will work well only in flow conditions where the model holds true.

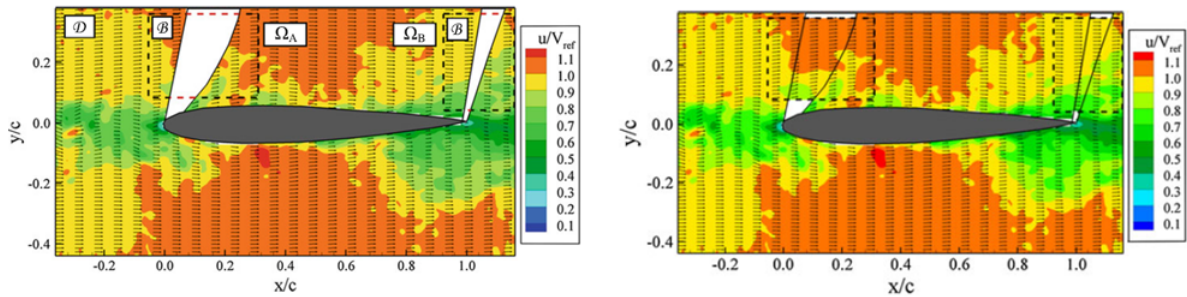


**Figure 3.1:** (Left) Identifying gappy region of a PIV experiment performed to investigate an aerofoil. (Right) Filled data with incompressible Navier stokes solver (reproduced from Sciachhitano et al. (2012))

### 3.7 Variational Methods and PIV

Variational methods are used to improve a noisy data by dynamically modifying it to minimise a cost function based on certain parameters. The field of computer vision has been using the phenomenon and in the past decade it has been adopted in PIV. Corpetti et al. (2005) utilised the continuity equation to enhance the particle motion estimation. More flow physics was utilised by Ruhnau et al. (2007) by utilising the full incompressible Navier-Stokes equation to improve the particle motion estimation. Recently Vlasenko et al. (2008,2010) used the variational methods for denoising the corrupted vector field using the vorticity transport equation and physically consistent regularisation. This concept was further developed into by Vlasenko et al. (2015) to restore flow field data corrupted by noise and gaps.

Lemke and Sesterhenn (2013) discuss a variational method which uses the full compressible Navier-Stokes equation in an adjoint based optimisation process. It minimises the squared difference between the PIV velocities obtained from measurements and numerical

simulations. Although the method aims to find pressure field from velocity data, considering the path of this review, the variational approach is to be focused on. Gronskis et al. (2013) use the adjoint based variational method to improve the output of direct numerical simulation using measurement data.

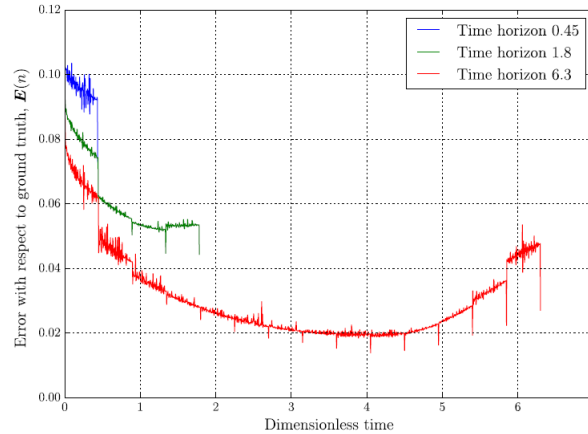


**Figure 3.2:** Lower error at initial time instant when assimilating longer measurements (reproduced from Yegavian et al. (2015))

A similar approach is adopted by Yegavian et al. (2015) to assess the performance of adjoint based data assimilation on the improvement of quality. They specifically point out that when the spatial density of the measurement increases, the quality of results enhances but the measurements temporal density does not play an as effective role. Another important observation is made that when considering measurement over a larger period of time the quality significantly improves. When assimilating longer measurements, the instantaneous error at the initial time instances decrease as shown in figure 3.2.

### 3.8 Numerical Optimisation Methods

Now all the variational methods minimise the cost function using some kind of numerical optimisation scheme. The BFGS (Broyden–Fletcher–Goldfarb–Shanno) method is one of the most popular Quasi-Newton numerical optimisation techniques. The main disadvantage of using the BFGS technique when handling very large amount of data is that it stores a dense inverse Hessian matrix and the methods becomes computationally inefficient. The LBFGS method was developed by Liu and Nocedal (1989) to approximate the BFGS method with a limited computer memory. As it consumes less memory it is computationally quite efficient as well.

The BFGS is a gradient based method. The gradient can be calculated using finite difference method but it faces the issue of being highly computationally expensive. Automatic differentiation (AD) methods have been developed to tackle the problem. The tangent linear method and adjoint method are the forward and reverse AD methods respectively. Their computational expense depends on the number of inputs and outputs of the system. If there are less input and more output parameter then the tangent linear is more efficient while for the other way round the adjoint method is superior.

# Vortex-in-Cell

The present chapter begins with an overview of the vortex methods and the theoretical concepts involved. This is followed by a discussion on the Vortex-in-Cell method in section 4.2. Hereafter the applications of the VIC method are presented, with two of the applications relevant to this thesis examined in more detail. At last a brief summary of the literature review is incorporated.

### 4.1 Vortex Methods

The Vortex methods are basically particle methods which have been formulated on the principle of approximation of the continuous vorticity field into discrete particles. Each vortex particle has certain strength and influences the velocity field in the domain. Particle methods in general have a Lagrangian form and same goes for the vortex methods. One of the advantages of the vortex methods is the exclusion of the pressure term which makes it of simplistic nature as compared to the full Navier-Stokes equations and reduces the complexity involved in solving them. Cottet et al. (2000) mention that the issue which arise due to the discretisation of the convective terms in the Navier-Stokes equations as well as their stability constraints, can be eliminated due to the Lagrangian form used by the methods. Furthermore the numerical representation of vortex dynamics of the fluid flow is done in a better way by using the vortex methods (Kudela, 1999)(Schneiders et al., 2014). They also provide direct and computationally efficient method for analysis of vortical features present in a flow thus making them a very useful tool to analyse the turbulent flows.

The vortex methods use the discrete version of the vorticity transport equation which is obtained by taking the curl of the Navier-Stokes momentum equation. The vorticity transport equation for an incompressible viscous flow is given by equation (4.1).

$$\frac{\partial \omega}{\partial t} + (u \cdot \nabla) \omega = (\omega \cdot \nabla) u + \nu \Delta \omega + \nabla \times f \quad (4.1)$$

In the absence of body force  $f$ , equation (4.1) reduces to

$$\frac{\partial \omega}{\partial t} + (u \cdot \nabla) \omega = (\omega \cdot \nabla) u + \nu \Delta \omega \quad (4.2)$$

As the vorticity transport equation is derived for incompressible Navier-Stokes momentum equation, the velocity field is divergence free as shown in equation (4.3).

$$\nabla \cdot u = 0 \quad (4.3)$$

The left hand side of equation (4.2) represents the rate of change of vorticity while the first term on the right represents the vortex stretching term and denotes the deformation of the vortices in three dimensional flows. The second term on the right hand side of equation (4.2) is the viscous term and represents the viscous diffusion of vorticity. When considering a simplified two dimensional inviscid problem the vortex stretching term in the vorticity transport equation drops out and it further reduces to equation (4.4).

$$\frac{\partial \omega}{\partial t} + (u \cdot \nabla) \omega = \nu \Delta \omega \quad (4.4)$$

Further assumption of the flow being inviscid renders the right hand side of the equation to be 0. Hence for an incompressible, inviscid and two dimensional flow, the vorticity transport equation is given by (4.5). This assumption will be used for one of the test cases to be presented in the later chapters.

$$\frac{\partial \omega}{\partial t} + (u \cdot \nabla) \omega = 0 \quad (4.5)$$

#### 4.1.1 Point Vortex

As discussed in the above sections, vortex methods deal with the discretisation of the continuous vortex field into discrete elements. Now these elements can take various forms such as small filaments, blobs (Chorin, 1973)(Chorin & Bernard, 1973), point vortices. The origin of the vortex methods can be traced back to the early part of the twentieth century where Rosenhead (1931) discretized the vortex field into elements represented by point vortices. Birkhoff and Fisher (1959) attempted the same approach with higher number of point vortices and better computational techniques. Some of the other literature about the development of the vortex can be found in Leonard (1980,1985).

$$\omega(x, t) = \sum_{j=1}^{N_p} \Gamma_j \delta[x - x_j(t)] \quad (4.6)$$

where  $\delta$  is the Dirac delta function while  $x_j$  represents the position of point vortices at time  $t$ . The variable  $\Gamma_j$  is the vectorial circulation of the point vortices or vortex particles. For a region  $S$  in a domain,  $\Gamma$  is given by equation (4.7).

$$\Gamma_S = \int_S \omega dx \quad (4.7)$$

The point vortices or the vortex particles can be viewed as fluid particles and are assumed to have displacement according to the magnitude and direction of velocity at their respective positions. The relation between the position and the velocity is given by the ordinary differential equation (4.8).

$$\frac{dx_p}{dt} = u(x_p(t), t) \quad (4.8)$$

In order to compute the displacement of the particles, the velocity field needs to be evaluated. The Poisson equation gives the relation between the velocity and vorticity field. The solution of the Poisson equation gives the velocity field.

$$\Delta u = -\nabla \times \omega \quad (4.9)$$

The solution of the Poisson equation (4.9) can be obtained using various methods. One of the ways is with the mesh free methods which provide an advantage of reducing the numerical dissipation or the smoothing observed in the conventional grid based solvers. The classical vortex methods use this mesh free approach as well. They have a form of a N body problem and each particle interacts with every other particle in the domain. This causes the computational cost to steeply rises with the increase in the resolution of the system (Morgenthal & Walther, 2007). In order to improve on this disadvantage, Greengard and Rokhlin (1987) introduced the Fast Multipole Methods which treats a group of vortex particles close to each other as a single source or entity. The computational expense for the mesh free method is of the order of  $O(N_p^2)$  while that for the FMM technique is  $O(N)$ (Morgenthal & Walther, 2007)(Greengard & Rokhlin, 1987) . For inspecting some of the implementations of FMM, the reader can refer to Strain (2996,1997) (Ploumhans, Winckelmans & Salmon, 1999) for two dimensional flows and (Bernard, 1999)(Najm et al., 1999) for three dimensional flows.

The velocity field in a mesh free system is usually calculated using the Bio-Savart law. If the assumption is made that the fluid is at rest at an infinite distance from the vortex particle and the flow is two dimensional then equation (4.10) gives the solution of the Poisson equation (4.9). This solution is obtained from the influence of one vortex particle, similarly the resultant velocity field has contributions from all the vortex particles in the domain.

$$u(x, t) = -\frac{1}{2\pi} \int \frac{(x - x') \times \hat{e}_z \omega(x', t) dx'}{|x - x'|^2} \quad (4.10)$$

The hybrid methods are the other class of methods and feature the usage of the Eulerian grid for solving the Poisson equation while retaining the benefits of Lagrangian form of the mesh free methods. They have been developed to essentially reduce the computational cost involved in evaluating the velocity by the Bio-Savart integration when involving high density system with large number of vortex particles (Leonard, 1980). The Vortex-in-Cell methods belongs to the family of the hybrid methods and is discussed in detail in the next chapter.

## 4.2 Vortex-in-Cell

The Vortex-in-Cell method was first introduced by Christiansen (1973) in order to solve the two dimensional incompressible inviscid flows. He adopted a hybrid approach where in the Poisson equation is solved on a regular computational grid. The vortex particles are advected in a similar fashion as done in equation (4.8) for the classical vortex methods but the difference is that they are interpolated back to a grid after each time step. This phenomenon is nicely depicted in figure 4.1(left) where the black dots represent the advected vortex particles while the white one represent the grid nodes. Once the calculation of the velocity field is done, it is interpolated to the particle locations in order to find the local velocities. Based on the local velocities, the particles are again advected and this process is repeated for all the time instances. For the conservation of moment, interpolation kernels of higher order (Monaghan, 1985)(Cottet & Koumoutsakos, 2000)(Kudela, 1999) are used in order to project the vorticity field on to the grid as well as find the velocity at the particle locations, so that the method is more accurate (Morgenthal & Walther, 2007).

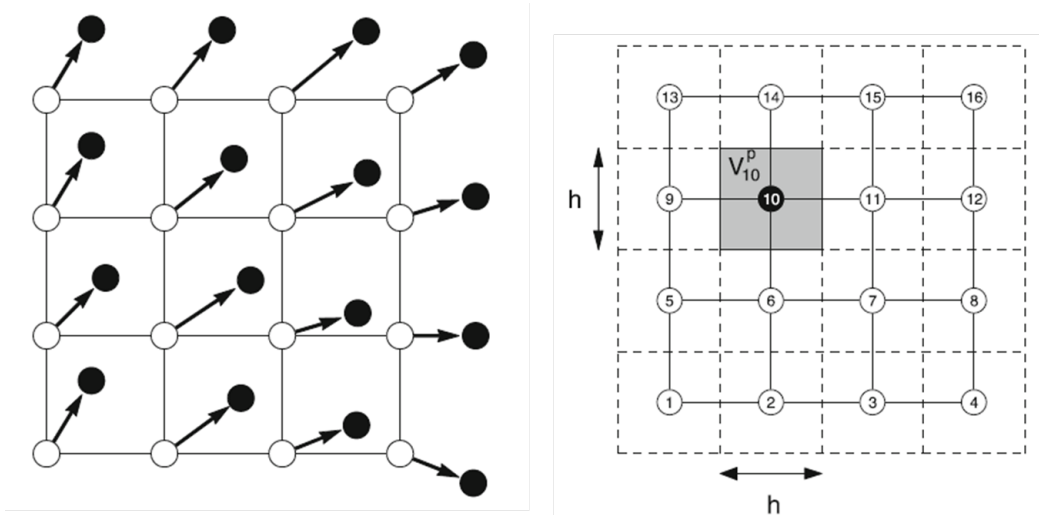


**Figure 4.1:** vortex particle advection (left), Initialisation of particle at each time step with shaded area assigned to the black particle (right) (reproduced from Schneiders et al. (2014)).

In Christiansen's approach the Poisson equation is written in terms of the stream function (4.11). Wherein for a two dimensional flow the vorticity and stream function are considered as scalars  $\omega = (0, 0, \omega)$ ,  $\Psi = (0, 0, \Psi)$ . The Poisson equation can be solved using multiple techniques available for solving differential equations on a Eulerian grid. For simple geometries the usage of Fast Fourier Transform provides accurate solution with low computational expense (Hockney, 1970)(Burrige & Temperton, 1979). The computational cost involved is of the order of  $O(N_p)$  (Morgenthal & Walther, 2007), which is one order of magnitude lower than that of the mesh free method.

$$\nabla^2 \Psi = -\omega \quad (4.11)$$

where,

$$\omega = \nabla \times u, \quad u = \nabla \times \Psi \quad (4.12)$$

Schneiders (2014) points out that the advantage of using the stream function is more profound in case of two dimensional flows where it reduces the number of equations to be solved for getting the velocity field. But when considering 3D flows equation (4.11) and (4.9) need similar computational effort to get the solution. For PIV experiments as the velocity field is readily available, it is better to use the formulation of Poisson equation which uses velocity directly rather than the stream function. For the present thesis, this phenomenon has been taken into consideration.

### 4.2.1 Applications of VIC

The vortex in cell method has been extensively used in the field of computational fluid dynamics offering a wide range of applications. VIC has been used to study problems such as two dimensional Kelvin-Helmholtz instability (Tryggvason, 1989)(Ribeiro & Kroo, 1995), turbulent flows (Abdolhosseini & Milane, 1996)(Cottet et al., 2002), two dimensional step (Savoie et al., 1996), vortex rings(Kudela & Kosior, 2011)(Couet et al., 1981)(Couet, Buneman & Leonard, 1981), flows near wall (Liu, 2001). Mohammadian and Marshall (2010) presented its application for the modelling of oceanic and atmospheric flows. It has been recently utilised for the direct numerical simulations of turbulent flows (Uchiyama et al., 2014)(Uchiyama & Yoshii, 2015).

VIC found its way into PIV applications when Schneiders et al. (2014) used it for increasing the temporal resolution of time resolved tomo-PIV. The method was further utilised to increase the spatial resolution of tomo-PIV data (Schneiders et al., 2015) with the use of adjoint based data assimilation. Schneiders et al. (2016) also devised a method to use the VIC framework to calculate the pressure measurement from instantaneous single snapshots of tomo-PIV. Some of the other possible applications (suggested by Schneiders et al. (2014)) of the VIC method for PIV are noise reduction of the PIV measurements and computation of material derivative from single snapshots or instantaneous velocity fields.

The proposed technique in this thesis will be developed from the VIC+ technique, which again utilises the time integration proposed in the time super-sampling method. Hence, it is relevant to discuss both the methods in greater detail.

### 4.2.2 Time Super-Sampling (Pouring Space in Time)

Time super-sampling method was introduced by Schneiders et al. (2014) to improve the temporal resolution of time resolved PIV data. The method is based on the VIC method and utilises the spatial information available to increase temporal information of the flow provided by PIV. The method is essentially applicable to incompressible flows and provides accurate time slices between two measurements sampled at a frequency lower than that defined by the Nyquist criterion.

The method solves the unsteady Navier-Stokes equation using the Vortex-in-Cell method, with the PIV measurement providing the initial conditions of the simulation. It assumes the viscous dissipation in a flow to be negligible considering the short integration time. This allows for the backward integration to be possible, enabling computation of the flow

field going back in time. When flow measurements at two time instances  $T_1$  and  $T_2$  are available then it performs forward time integration from  $T_1$  to  $T_2$  as well as backward time integration from  $T_2$  to  $T_1$ . The super-sampled time slices are a weighted average of both the integration, thus enforcing temporal continuity of the solution. This working principle is very well depicted in figure 4.2.

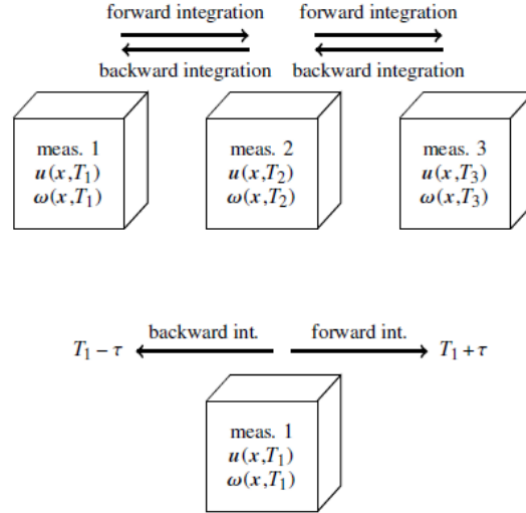


**Figure 4.2:** Working principle of time super-sampling. (Top) Using measurements at two time instances to produce time slices between them. (Bottom) Time series creation from instantaneous flow field (reproduced from Schneiders et al. (2014)).

Temporal reconstruction of fields from instantaneous snapshots can also be done, but the possible constraint being that the reconstructed field is only as apart in time till the assumption of neglecting the viscous dissipation holds. An experimental assessment of a sub-sampled measurement of a transitional jet (Schneiders et al., 2014) demonstrated that the method perform highly accurate reconstruction as compared to the advection model proposed by Scarano and Moore (2011).

### 4.3 VIC+ (Pouring Time in Space)

The VIC+ method was introduced by Schneiders et al. (2015) to use the temporal information available in time resolved tomo-PTV data to increase the spatial resolution of instantaneous Eulerian flow field.

This method adopts an iterative gradient based numerical optimisation technique to minimise a cost function  $J$  consisting of terms containing instantaneous spatial data and temporal information of the fluid. The temporal information is provided in the form of the material derivative of velocity, which in turn is made available from the particle tracking algorithm (tomo-PTV). The initial field is obtained from the measurement values while the velocity field for subsequent time instances after the initiation of the optimisation process are computed from time super-sampling technique Schneiders et al. (2014).

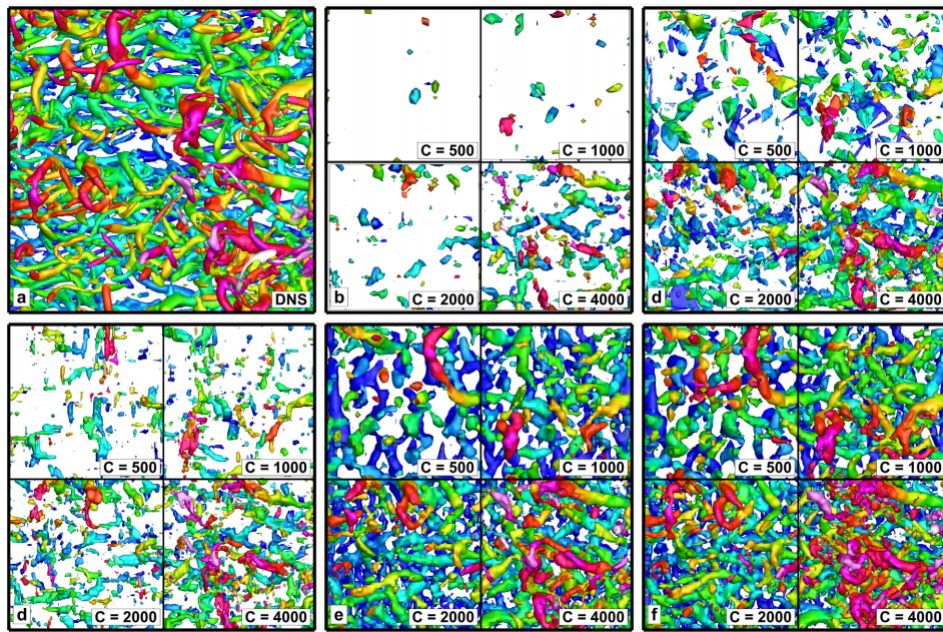


**Figure 4.3:** Isosurfaces of Q-Criterion reconstructed using various methods for different seeding concentrations  $C$  (particles/ $\delta_{99}^3$ ); (a) DNS reference, (b) PIV, (c) Linear interpolation, (d) AGW, (e) Divergence free regression, (f) VIC+ (reproduced from Schneiders et al. (2015)).

The ability of the method to increase spatial resolution was demonstrated by Schneiders et al. (2015) through numerical assessment of a turbulent boundary layer produced by direct numerical simulation. VIC+ was found to produce higher resolution velocity fields as compared to trilinear interpolation, AGW and solenoidal filtering. An experimental analysis (Schneiders et al., (2016a)) on the turbulent boundary layer concluded similar outcomes with the method producing accurate vorticity dynamics in the boundary layer. A recent comparative study of different pressure computing techniques in PIV (Blinde et al., 2016), depicted that the VIC+ method produced highly accurate instantaneous pressure fields as compared to the cross correlation based methods.

#### 4.4 Literature Survey Conclusion

Firstly it would be important to discuss the findings of Yegavian et al. (2015), who show that increase in the length of the time series obtained from experiments enhanced the quality of the results obtained by numerical simulation. This is a good basis to hypothesize that the proposed method would prove out to produce positive results.

It was pointed out in chapter 2 that PTV does not suffer from interrogation window based filtering as opposed to PIV. On the other hand PTV does not directly evaluates gridded information. The advantages of both the methods can be combined to negate their disadvantages. Due to the recent advancements in the field of Lagrangian particle tracking algorithms (Schanz et al., 2014), creation of long and accurate particle tracks in densely seeded flows has become feasible. The accurate temporal information available from these tracks can be leveraged and 'poured into space' to increase the spatial resolution of the

tomo-PIV data on a grid. A variational framework along with a flow solving technique is required to take advantage of the temporal information available through PTV.

The Vortex-in-Cell method provides a computationally efficient and robust way of computing the velocity field on a grid as compared to the conventional Navier-Stokes solvers. These methods can help overcome the limited use of the iterative data assimilation methods on real three dimensional measurement data. The solenoidal flow field is enforced by solving the Poisson equation in this method. This as discussed in section 3.5, also helps to reduce noise and improve the overall quality of the reconstructed flow field.

In order to solve a variational problem, choice of right numerical optimisation method is essential. The disadvantages of the BFGS method are discussed in section 3.7. As tomo-PIV generates huge amount of data LBFGS numerical optimisation method would be the logical choice. Also a method involving a long time series would be computationally expensive so the choice of numerical optimisation has to be taken keeping the same into consideration. At last the different gradient finding methods have also been discussed. The adjoint method would be most appropriate for the present case primarily because the number of inputs in the optimisation would be very large while the output is just the cost function. As said in the previous section, with more inputs and less outputs the adjoint method is superior when computational expense is concerned.

# Proposed Method

*Part of the work published in the 8<sup>th</sup> International Symposium on the Application of Laser and Imaging Techniques of Fluid Mechanics, Lisbon, Portugal (Schneiders et al., 2016b).*

This chapter describes the theoretical aspects about the proposed method. It is followed by the discussion on the working principle of the method and its numerical implementation. The algorithm of the method is also presented and the chapter is culminated by a brief discussion on the gradient calculation using the adjoint code and its comparison with the finite difference method from the perspective of the proposed method.

### 5.1 Theoretical Background

The ability of the VIC+ method to improve the spatial resolution of the tomo-PTV data interpolated on a grid was discussed in the previous chapter. Information of the flow in the form of the instantaneous velocity and its material derivative is utilised by the method. For the present work it is proposed to utilise full particle tracks obtained from tomo-PTV in the VIC+ framework. The rationale behind this proposal is that when full tracks are used, the flow information at all the time instances is to be leveraged which in turn should result in the better reconstruction of the instantaneous Eulerian flow field. The proposed method is an extension of the VIC+ method and for convenience will also be named as 'VIC++' method along with the already mentioned term 'proposed method' in the rest of the document.

A schematic diagram to show the information used by different methods including the proposed method is presented in figure 5.1. The grey lines depict the particle tracks found from PTV while the blue dots represent the particle positions at different time instances. The red dots represent the particles and the vectors indicate the information used for the reconstruction of the velocity field. The linear interpolation just uses the instantaneous velocity measurements at the particle location. It linearly fits a curve which

passes through these points. The VIC+ method on the other hand uses the instantaneous velocity as well as the material derivative to produce the velocity on a fine Eulerian grid (represented by the yellow lines). The VIC++ method however leverages the velocity information of the full particle tracks and is expected to reconstruct data with even higher spatial resolution.

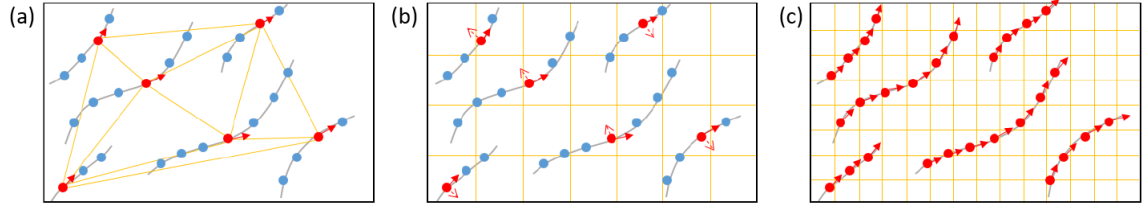


**Figure 5.1:** Schematic diagram of an PTV Lagrangian track and the information used (red) by different methods for reconstruction. (a) Linear interpolation (b) VIC+ (c)VIC++ (reproduced from Schneiders et al. (2016)).

## 5.2 Working Principle and Numerical Implementation

The method is based on the iterative gradient based numerical optimisation technique and involves the VIC time integration, applied to the PIV measurement data in a similar fashion as is done in Schneiders et al. (2014). Figure 5.2 presents a coarse flow chart on the working of the method. The detailed algorithm is presented in the chapters to follow.

The method requires the tomo-PIV data as an input to the system. The data is used for the initial guess for the method, but more importantly for the boundary conditions at all the time instances during the time integration. As the method involves numerical optimisation, a good initial guess will result into faster convergence of results. The method primarily needs the Lagrangian tracks obtained directly from tomo-PTV which involves voxel based approach to find the particle trajectories and the particles corresponding velocity information. The tracks used can also be obtained using the advanced particle tracking algorithms such as IPR (Wieneke, 2012) and STB (Schanz et al., 2014).

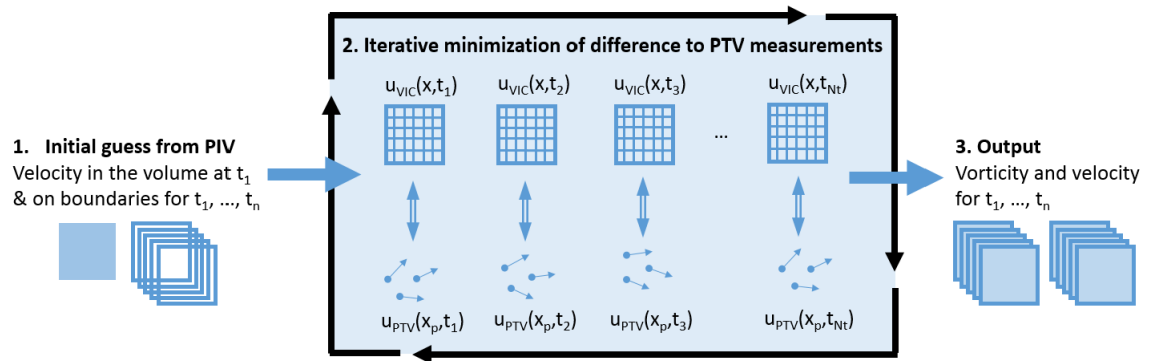


**Figure 5.2:** Flowchart of the proposed method (reproduced from Schneiders et al. (2016)).

The Lagrangian data of the particle tracks act as a reference in the optimisation procedure. This has a serious implication that the method at best can only be as good as the PTV

data. If there are some inherent errors in the PTV data then are directly transferred to the reconstructed flow field.

### 5.2.1 One Time Step

For the detailed discussion on the steps involved in the VIC++ method, it would be better to start with a simpler algorithm and then extend it to achieve the desired goal. Firstly an algorithm which involves leveraging information at two time instances or one time step is presented in figure 5.4. This algorithm is expanded to include more time steps and form the VIC++ method.

The method starts with the input of the tomo-PIV velocity vectors at time instant  $t_i$ . This velocity field is available on a regular grid and is named as  $\bar{U}_{g_i}$ , where the subscript  $i$  denotes the velocity at the time instant  $t_i$ . This velocity field is used to calculate the vorticity field  $\bar{\omega}_{g_i}$  by simply taking its curl. The vorticity field instead of the velocity field is used further in the numerical optimisation process because it assists in the automatic dampening of the peaks in the output field which emerge due to the unconstrained optimisation used in the method.

The VIC forward time integration is applied on the vorticity field to obtain the field corresponding to the next available time slice of the particle tracks. It is important to note that the time integration is only performed at the grid nodes inside the domain and not at the boundary. The boundary conditions are taken from the tomo-PIV data. Also the integration time step is much smaller than the time between adjacent tomo-PTV time slices ( $t_i$  and  $t_{i+1}$ ) and is decided based on the criteria mentioned by Schneiders et al. (2014), as discussed in chapter 4. The vorticity field found as an output of the VIC time integration will be referred to as  $\bar{\omega}_{VIC}$ . The VIC time integration performed on  $\bar{\omega}_{g_i}$  gives the vorticity field at the next time instant ie.  $\bar{\omega}_{VIC_{i+1}}$ . This corresponding velocity field  $\bar{U}_{VIC_{i+1}}$  at  $t_{i+1}$  is calculated by solving the Poisson equation (4.9).

Now in order to compare this gridded velocity field to the reference velocity of the particles, it is linearly interpolated to the particle locations to compute  $\bar{U}_{VIC_{s_{i+1}}}$ . Figure 5.3 presents the schematic diagram representing the grid nodes (blue dots) and the particle positions (red dots). A bi-linear interpolation is performed and the value of velocity at the particle location is computed based on the contribution from the velocity at the nodes surrounding the particle. The contribution of a velocity at a grid node depends on and is inversely proportional to the distance of the particle from the node. For example the contribution of node  $(x_3, y_3)$  in figure 5.3 linearly depends on  $l_x$  and  $l_y$ . Smaller the value of  $l_x$  and  $l_y$  higher is the velocity contribution of  $(x_3, y_3)$  at  $(x_p, y_p)$ .

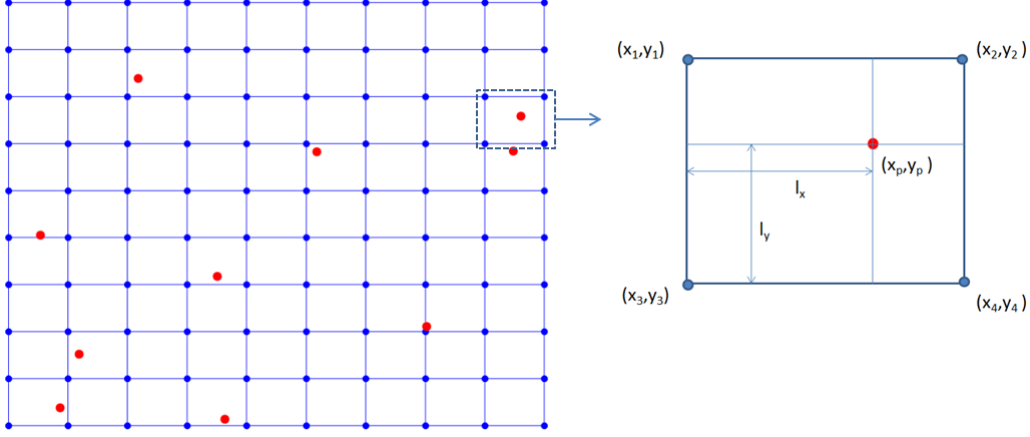


**Figure 5.3:** Schematic diagram of the grid nodes (blue) and the particle positions (red). Contribution of the node  $(x_3, y_3)$  depends on  $l_x$  and  $l_y$

A non linear optimisation problem is formed to compare the particle velocities  $\bar{U}_{PTV}$  to that with the one found from the linear interpolation of  $\bar{U}_{VIC}$  to the respective particle position  $\bar{X}_{ptv}$ . In this regard a cost function is developed with its value being equal to the norm of the difference of the velocities at the time instant  $t_{i+1}$ . The cost function is the linear combination of the individual cost functions of all the  $N_p$  particles. The optimisation problem deals with the minimisation of the cost function by varying the vorticity field at time  $t_i$ .

$$J = \sum_{j=1}^{N_p} \left( \bar{U}_{VICs_{i+1}}^j - \bar{U}_{PTV_{i+1}}^j \right)^2 \quad (5.1)$$

In order to regularise the optimisation problem the velocity field at time  $t_i$  is also interpolated to  $\bar{X}_{PTV_i}$  and compared with  $\bar{U}_{PTV_i}$ . This enforces the regularisation of the initial condition of the problem. After every iteration when  $\bar{\omega}_{g_i}$  is varied, the corresponding velocity field is computed by solving the Poisson equation (4.9). The introduction of the term corresponding to the initial condition in the cost function modifies it to equation (5.2).

$$J = \sum_{j=1}^{N_p} \left( \bar{U}_{VICs_{i+1}}^j - \bar{U}_{PTV_{i+1}}^j \right)^2 + \sum_{j=1}^{N_p} \left( \bar{U}_{g_i}^j - \bar{U}_{PTV_i}^j \right)^2 \quad (5.2)$$

In order to solve the non linear optimisation problem posed to minimise the cost function in equation (5.2), a gradient based optimisation method is utilised. From the myriads of techniques the LBFGS method proposed by Liu and Ncedal (1989) is used for the problem. A discussion on the choice of the technique is presented in chapter 3. A gradient based method requires the calculation of the gradient of the cost function with respect to the degree of freedom in every iteration. The degree of freedom of the optimisation problem are the variables which are iteratively varied by the method to minimise the cost function and are stored in a vector  $\zeta$ . The gradient  $\frac{dJ}{d\zeta}$  can be calculated by finite

differences but the computational cost involved rises exponentially with the number of degree of freedom involved in the system. The degree of freedom corresponds to the number of grid nodes in the computational domain and for a three dimensional domain has the size of  $(N_x \times N_y \times N_z)$ . The optimisation problem performs the time integration as many times to find the gradient with respect to each degree of freedom in the vector  $\zeta$ . In order to solve this issue in a computationally efficient way, automatic differentiation methods have been looked upon. The adjoint method is used in the present algorithm to compute the gradient and results in a hugely reduced computational effort with just one time integration required for the calculation. This is really important with respect to the computational feasibility of the proposed method. The advantage of the reduced computational cost is accompanied with the issue large usage of memory for the adjoint code. When the time integration considered is longer, this constraint becomes more significant. For the present method, time sequences of the order of 40 snapshots are used and the memory related drawback has a limited impact.

In the entire optimisation process, finding the gradient through the adjoint method is one of the most difficult parts to execute. Hence a detailed discussion of the process will be presented in the section to follow.

The termination of the iterative process of optimisation is done on reaching a specified tolerance level either based on the value of the cost function  $J$  or the change in the degree of freedom  $\Delta\zeta$ . For the present scenario the second option is chosen and the iteration stops when the change in the degree of freedom is less than the tolerance of  $\zeta_{con}$ .

### 5.2.2 Multiple Time Step (VIC++)

The full VIC++ method is an extension of the one time step algorithm discussed in the previous sub section. Detailed algorithm of the VIC++ method is presented in figure 5.5. The time resolved tomo-PTV data to be used has a time length of  $N_t$  snapshots. The nomenclature followed in this case is same as for the one step method.

The algorithm starts similarly with the tomo-PIV gridded data and particle tracks as inputs. The cost function  $J_1$  is found in the same manner as done in equation (5.1) but is not the final cost function to be used for the numerical optimisation. It rather is a contributor to the main cost function and represents the infusion of flow information at time  $t_{i+1}$ . The velocity field found at time  $t_{i+1}$  is further used as an initial condition for the VIC time integration and the Eulerian field is computed at time  $t_{i+2}$ . Again using this velocity and the tomo-PTV particle velocities at  $t_{i+2}$  a partial cost function  $J_2$  is computed. This procedure is repeated till the partial cost function  $J_{N_t-1}$  has been calculated. The main cost function  $J$  is then computed as the linear combination of all the partial cost functions.

$$J = \sum_{k=1}^{N_t-1} J_k + \sum_{j=1}^{N_p} \left( \bar{U}_{g_i}^j - \bar{U}_{PTV_i}^j \right)^2 \quad (5.3)$$

where,

$$J_k = \sum_{j=1}^{N_p} \left( \bar{U}_{VIC_{s_{i+1}}}^j - \bar{U}_{PTV_{i+1}}^j \right)^2 \quad (5.4)$$

Again the initial condition regularization term is included in the cost function as shown in equation (5.3). The vorticity field at time  $t_i$  is updated after every iteration with a goal of reducing the cost function. Ultimately when the change in the vorticity field is less than a specified tolerance level, the program is terminated. The output of the entire optimisation process is a vorticity field on a regular grid at time  $t_i$  which in turn is used to compute the velocity field at that time instant.

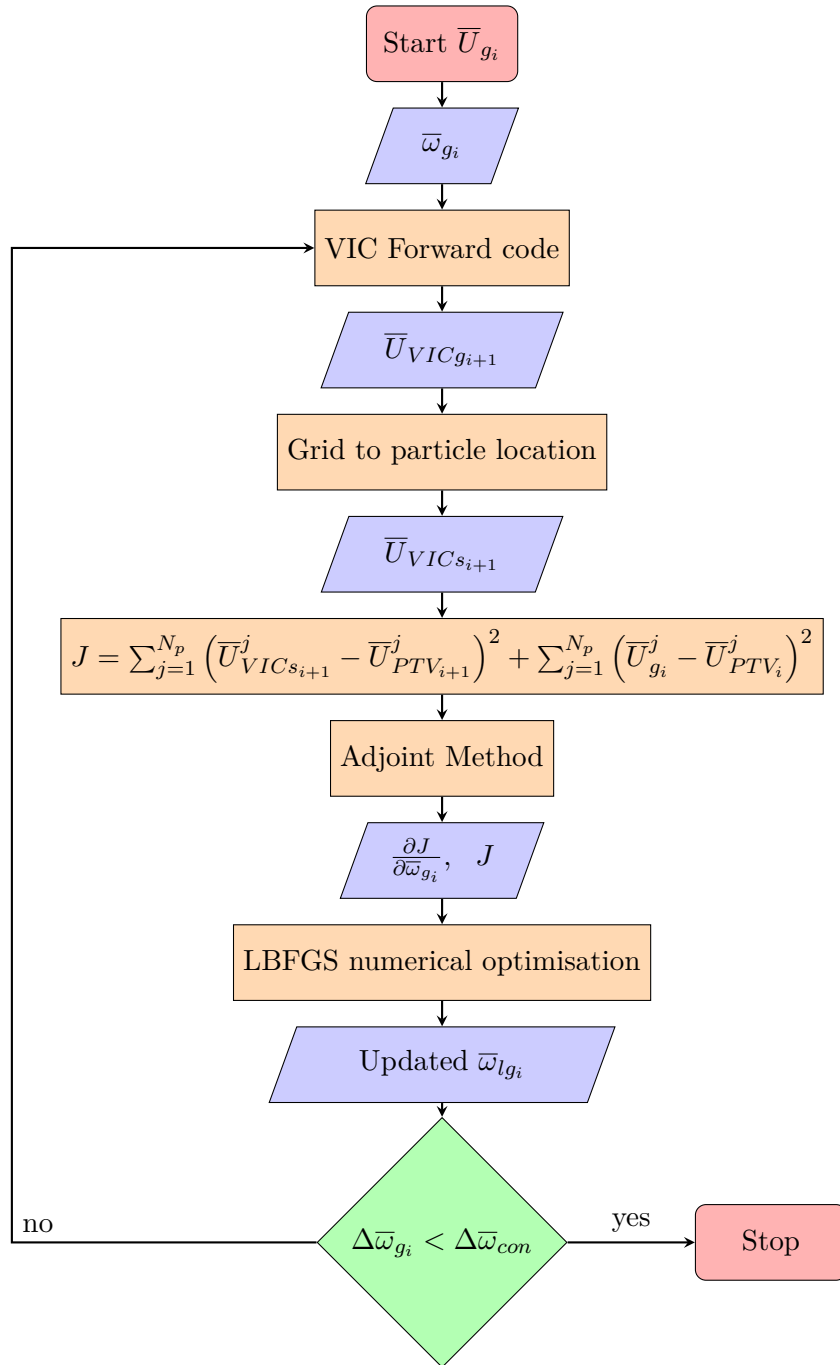


Figure 5.4: Algorithm of proposed method involving one time step

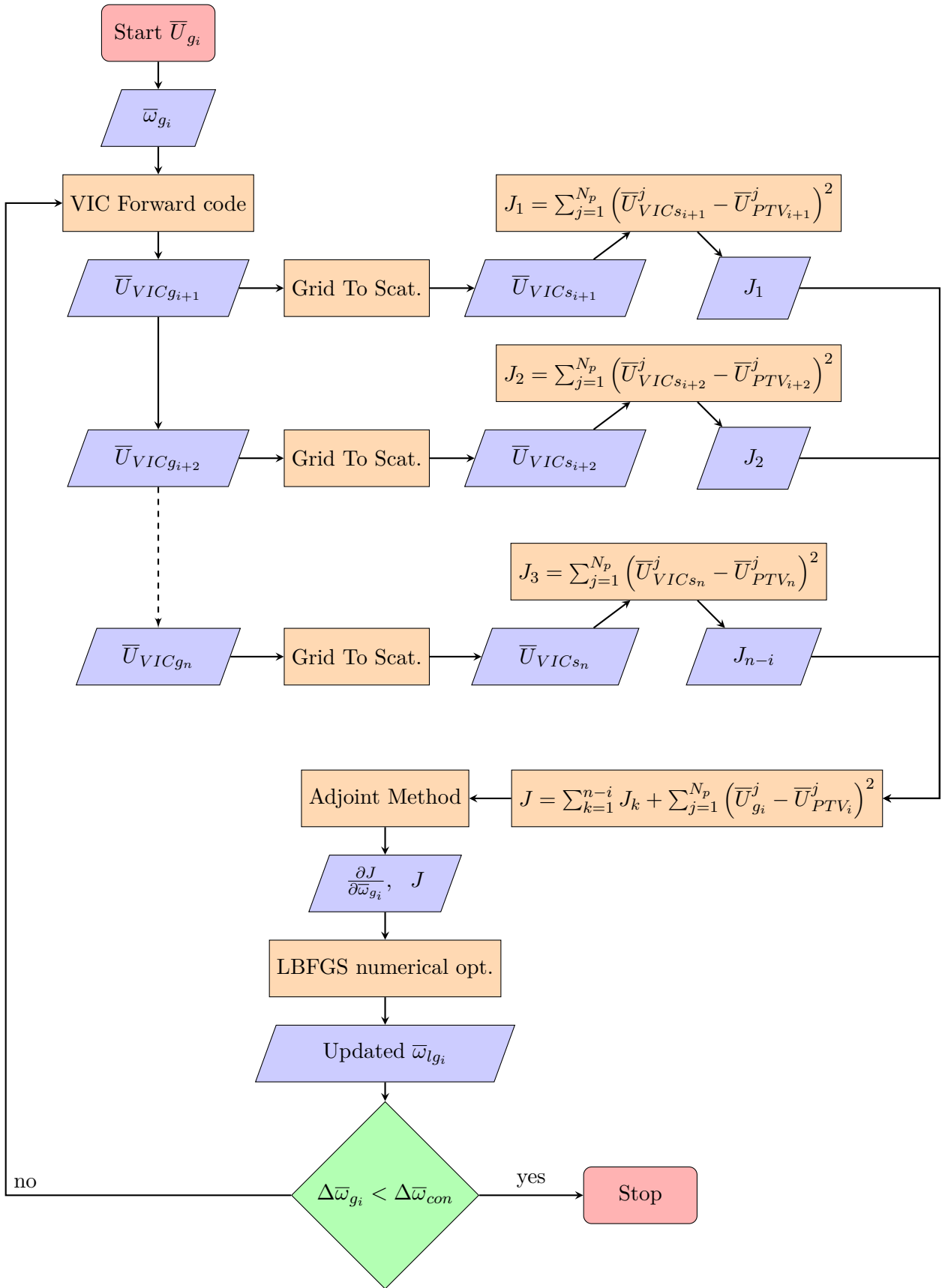


Figure 5.5: Algorithm of the full VIC++ method

### 5.3 Adjoint Method

The adjoint method is a numerical approach which is used for the efficient evaluation of gradient of a cost function in an optimisation problem. The advantage of using adjoint method over the conventional finite difference method is twofolds, one being the exact computation of gradient devoid of the presence of any truncation error in contrast to the finite differences. The other benefit being large reduction in the computational cost. The gradient of the cost function with respect to the input variables represents the sensitivity of the system to the change in its input. This is why gradient computation is also termed in the literature as sensitivity analysis.

Adopting the formulation presented by Marta et al. (2007), a general representation of the adjoint method is discussed. Cost function  $J$  is a function of the output of the governing equations and the input variables  $\zeta$ . The input variables are also referred to as the degree of freedom of the system. The governing equations are denoted by equation (5.6). For the present case it is the vorticity transport equation.

$$J = J(u(\zeta), \zeta) \quad (5.5)$$

$$R = R(\zeta, u(\zeta)) = 0 \quad (5.6)$$

Now using the chain rule, gradient of the cost function can be written as equation (5.7). The most expensive term of the equation is  $\frac{\partial u}{\partial \zeta}$  (Marta et al., 2007).

$$\frac{dJ}{d\zeta} = \frac{\partial J}{\partial \zeta} + \frac{\partial J}{\partial u} \frac{\partial u}{\partial \zeta} \quad (5.7)$$

The governing equation can also be written in a similar form. As the input variables satisfy the equations, the gradient of  $R$  with respect to  $\zeta$  should also be equal to zero.

$$\frac{dR}{d\zeta} = \frac{\partial R}{\partial \zeta} + \frac{\partial R}{\partial u} \frac{\partial u}{\partial \zeta} = 0 \quad (5.8)$$

Using equation (5.8), The cost function gradient can be written as

$$\frac{dJ}{d\zeta} = \frac{\partial J}{\partial \zeta} - \frac{\partial J}{\partial u} \left[ \frac{\partial R}{\partial u} \right]^{-1} \frac{\partial R}{\partial \zeta} \quad (5.9)$$

Defining an adjoint vector  $\lambda^T = \frac{\partial J}{\partial u} \left[ \frac{\partial R}{\partial u} \right]^{-1}$ . Thus the gradient of the cost function  $J$  can be defined by

$$\frac{dJ}{d\zeta} = \frac{\partial J}{\partial \zeta} - \lambda^T \frac{\partial R}{\partial \zeta} \quad (5.10)$$

With,

$$\left[ \frac{\partial R}{\partial u} \right]^T \lambda = \left[ \frac{\partial J}{\partial u} \right]^T \quad (5.11)$$

This adjoint formulation enables the computation of gradient using  $N_J$  linear system of equations. As for the present case the cost function results in only one numerical value, hence requiring only one set of equations to be solved. The partial derivative involved in the equation are obtained by the reverse automatic differentiation method.

### 5.3.1 Adjoint Method vs Finite Difference Method

Inspection of the advantage provided by the adjoint code in the view of the VIC++ method can be done by comparing its computational cost with its conventional counterpart. For this the VIC++ method with 2 snapshots is considered with varying grid size. The gradient of the cost function  $J$  with respect to the degree of freedom  $\zeta$  is computed by both the methods. The variation of the time taken by the two methods with respect to the grid size is shown in figure 5.6. It can be seen that the computational time of finite difference method rises steeply and goes to around 350 seconds for a  $30 \times 30$  grid, on the other hand the adjoint code for the same grid size requires approximately 0.5 seconds. The finite difference curve has a higher slope as compared to the adjoint method meaning that the expense rises more rapidly in the former case.

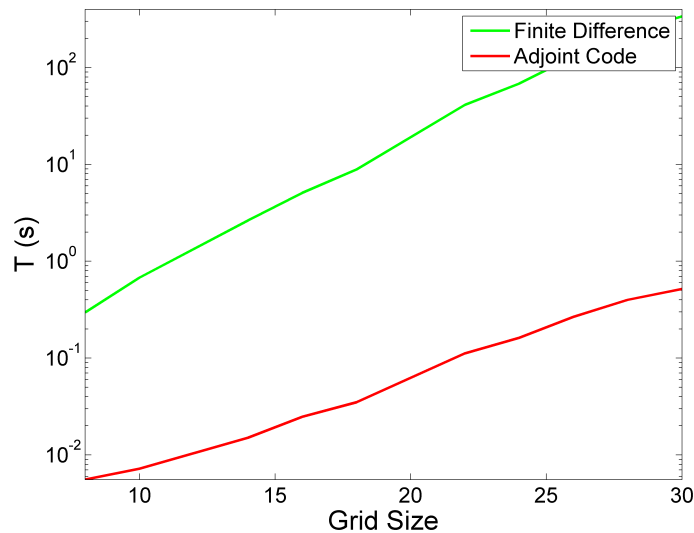


**Figure 5.6:** Variation of gradient computation time for VIC++ (2 snapshots) using finite difference method (green), adjoint code (red) with respect to the grid size

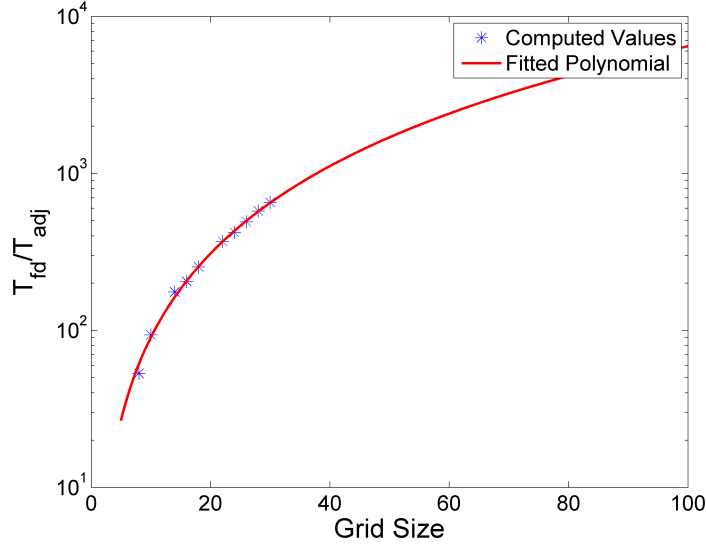


**Figure 5.7:** Ratio of gradient computation time using finite differences to that using adjoint code for VIC++ (2 snapshots), varying with respect to the grid size

To put things into better perspective, the ratio of time consumed by the two methods, i.e.  $\frac{T_{fd}}{T_{adj}}$  is plotted with different grid sizes. For a  $30 \times 30$  grid, the adjoint code is almost 700 times faster. A polynomial is fitted to relate the increasing trend of ratio of computational time of the two methods. It is observed that  $\frac{T_{fd}}{T_{adj}}$  vs grid size follows a quadratic trend shown by equation (5.12).

$$\frac{T_{fd}}{T_{adj}} = p_1 N^2 + p_2 N + p_3 \quad (5.12)$$

Where  $p_1, p_2, p_3$  are the coefficients of the quadratic equation and  $N$  is the grid size. For the present case the coefficients were found out to be  $p_1 = 0.61, p_2 = 3.57, p_3 = -6.48$ . The important thing to observed is that  $\frac{T_{fd}}{T_{adj}}$  scales with  $O(N^2)$ . Thus proving that it is tremendously cost effective to use the adjoint code for the computation of the cost function gradient at the expense of increased memory usage.

# Numerical Assessment

The detailed numerical validation of the proposed method is presented through a synthetic test case of a two dimensional vortex blob. Various aspects of the method are analysed to assess its working and robustness under a range of conditions. The method is compared with some conventional interpolation methods as well as introspected on qualitative and quantitative scales.

### 6.1 Analytical Vortex Blob

A translating 2D vortex blob is being considered for the synthetic test case. This test case have been previously used by de Kat R and van Oudheusden (2014), Lynch and Scarano (2014), Schneiders et al. (2016a). As the translating vortex blob does not feature any viscous dissipation, the viscosity term in the vorticity transport equation is neglected. The flow field defined in this synthetic test case is a linear combination of uniform advecting velocity and a Gaussian vortex blob. Both the components of translating velocity can be modified to control the movement of the blob in the computational domain. The vortex core radius  $r_c$  is defined as the distance from the core center where the tangential velocity achieves its peak. Figure 1.1 presents the distribution of the two components of tangential velocity. The rotational velocity of the particles is given by equation (6.1).

$$V_{rot} = \frac{\Gamma}{2\pi r} \left( 1 - e^{-\frac{r^2}{c_\theta}} \right) \quad (6.1)$$

$$c_\theta = \frac{r_c^2}{\gamma} \quad (6.2)$$

where  $\Gamma$  is the circulation,  $r$  is the distance of a particle from the center of the vortex blob.  $c_\theta$  is a factor of scaling and constant  $\gamma$  is chosen such that the peak velocity of the flow is at a distance of  $r_c$  from the vortex core center. The total velocity of a particle is given by the summation of the rotational as well as translational velocities.

$$V_{particle} = V_{rot} + V_{translational} \quad (6.3)$$

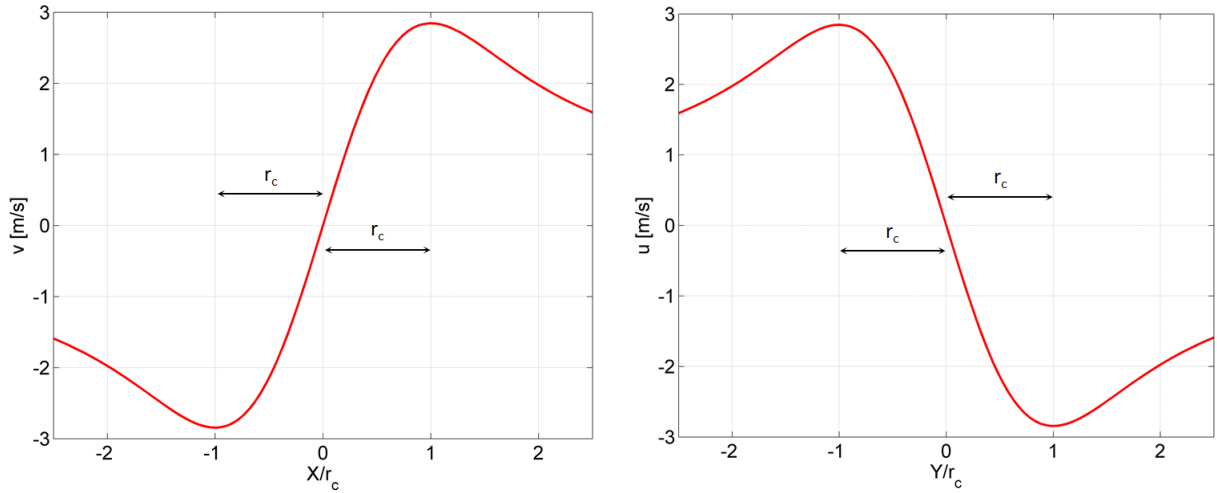


**Figure 6.1:** Profile of the  $v$  component of velocity along the x-axis (left), Profile of the  $u$  component of velocity along the y-axis (right)

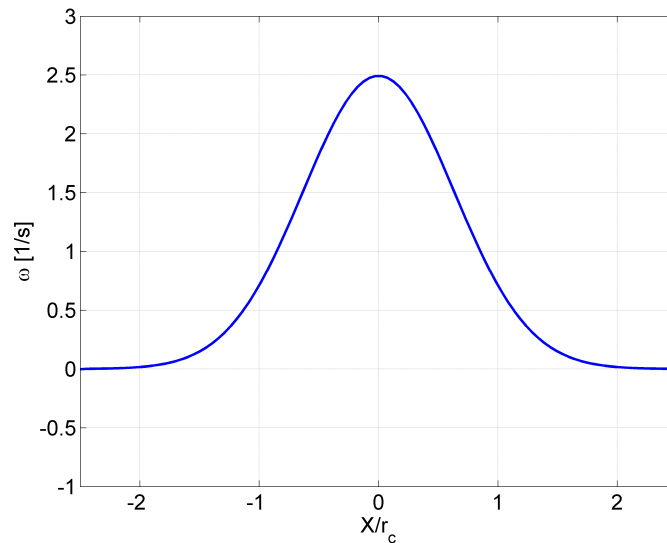


**Figure 6.2:** Vorticity distribution along the x-axis

As mentioned before the vorticity distribution for the vortex blob is of the Gaussian form. Figure 6.3 presents the vorticity distribution of the blob along the normalised x-axis. As observed from the figure 6.3 the vorticity reaches its maximum value at the central point of the vortex core. It reduces as one moves away from the core center ultimately attaining a zero value. This means that when the vorticity becomes zero the vortex blob does not have any effect on the particles i.e. they don't have any rotational velocity and their movement becomes purely translational.

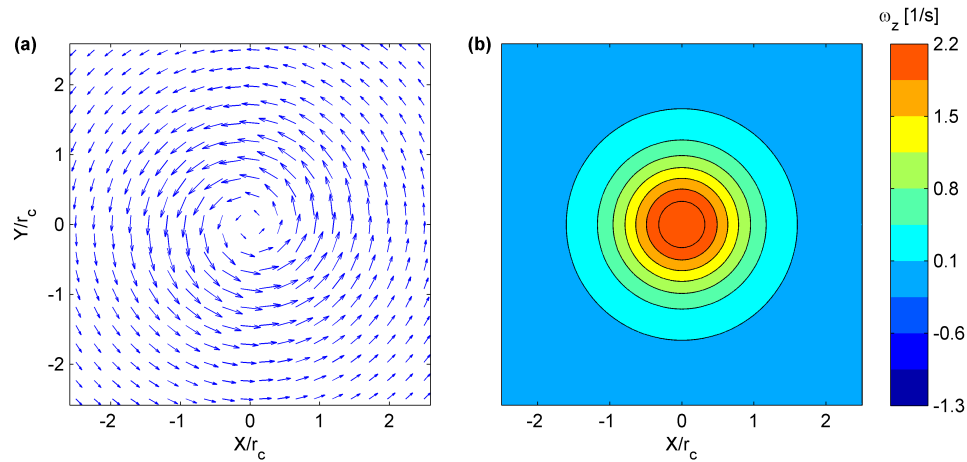


**Figure 6.3:** Reference velocity vector field (left), Analytical Vorticity (right)

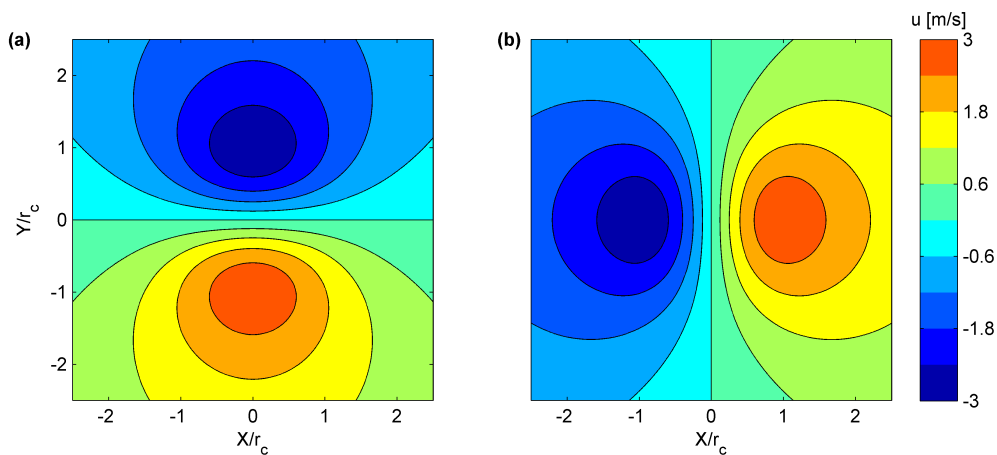


**Figure 6.4:**  $u$  component of velocity (left) ,  $v$  component of velocity (right)

The contour plot of the vortex field is shown in figure 6.3 (right). It shows concentric vortex rings around the centre of the vortex. This means that the vorticity of any point equidistant from the vortex center is the same which in turn says that the rotational velocity of any point equidistant from the vortex center is same. The respective vector field of velocity can also be observed in figure 6.3. Figure 6.4 presents the contour plot of the  $u$  and  $v$  components of velocity. The rotational velocity at the center of the core is zero, attains a peak at  $r_c$  then again goes back to zero.

## 6.2 Particle Tracks

The creation of flow field is followed by the introduction of random particles in the domain and creating the tracks. The tracks are analogous to the Lagrangian tracks obtained through tomo-PTV. The velocity of the particles are calculated from analytical equation

(6.1) and (6.3). The advancement of the particles in time can be found out by many methods. The two dimensional explicit Runge-Kutta fourth order time integration scheme is used for the current case.

$$\begin{aligned} x_{n+1} &= x_n + \frac{1}{2} (k_1 + 2k_2 + 2k_3 + k_4) \delta t \\ y_{n+1} &= y_n + \frac{1}{2} (m_1 + 2m_2 + 2m_3 + m_4) \delta t \end{aligned} \quad (6.4)$$

where,

$$\begin{aligned} k_1 &= u(x_n, y_n, t_n), & m_1 &= v(x_n, y_n, t_n) \\ k_2 &= u\left(x_n + \frac{1}{2}k_1\delta t, y_n + \frac{1}{2}m_1\delta t, t_n\right), & m_2 &= v\left(x_n + \frac{1}{2}k_1\delta t, y_n + \frac{1}{2}m_1\delta t, t_n\right) \\ k_3 &= u\left(x_n + \frac{1}{2}k_2\delta t, y_n + \frac{1}{2}m_2\delta t, t_n\right), & m_3 &= v\left(x_n + \frac{1}{2}k_2\delta t, y_n + \frac{1}{2}m_2\delta t, t_n\right) \\ k_4 &= u\left(x_n + \frac{1}{2}k_3\delta t, y_n + \frac{1}{2}m_3\delta t, t_n\right), & m_4 &= v\left(x_n + \frac{1}{2}k_3\delta t, y_n + \frac{1}{2}m_3\delta t, t_n\right) \end{aligned}$$

The Lagrangian tracks of 5 particles with only rotational velocity and with both rotational as well as translational velocity shown in figure 6.5. Two movement of the vortex core can be distinctly noticed in both the figures.

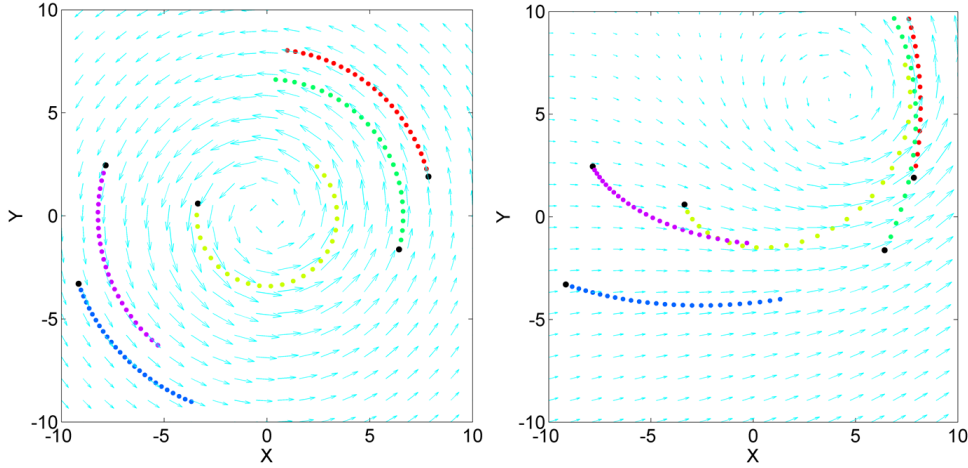


**Figure 6.5:** Particle tracks with only rotational velocity (left), Particle tracks with rotational and translational velocity (right).

### 6.3 Reconstruction and Error Determination

The infusion of particles and creation of their tracks is followed by the reconstruction of the velocity and vorticity fields using various methods. The fields need to be reconstructed from the scattered particle tracks to a uniform grid. The methods which are used in the present test case to be compared to the VIC++ method are listed below:

- Linear Interpolation
- Adaptive Gaussian Windowing
- Particle Image Velocimetry

The reconstruction quality of each method is inspected by using qualitative as well as quantitative analysis techniques. Qualitative analysis is done by the inspection of velocity and vorticity contour plots while the quantitative analysis is done by computing the error of the reconstructed velocity field with respect to the analytical velocity field. The error is calculated by the  $L^2$  norm of the difference between reconstructed and analytical fields as demonstrated in equation (6.5).

$$\epsilon_{rms} = \sqrt{\left(\frac{\sum_{i=1}^N (|u_{R_i} - u_{A_i}|)^2}{N}\right)} \quad (6.5)$$

where  $u_A$ ,  $u_R$  are the analytical velocity field and the reconstructed velocity field respectively with  $N$  being the number of computational grid nodes.

#### 6.4 Linear Interpolation, AGW and PIV

Linear interpolation is one of the most trivial methods to get gridded data from scattered data. The method fits a linear curve with values passing through the scattered points to find the values on the grid. The main issue with the method is that it does not perform any kind of noise filtering in the data. So if the data is noisy then it is not expected to reconstruct with good quality. As currently exact data is being used for scattered values, its reconstruction quality is expected to be fine.

The AGW method is a bit more advanced as compared to the linear interpolation. This method applies a Gaussian filter and can handle noisy data to some level. According to the original method proposed by Agüí and Jiménez (1987) AGW method involves weighted averaging over all the vectors in the observation volume with the weight depending on the distance of the particle from the local origin. A slightly modified AGW method is used in the present work on lines of the method suggested by Stuer and Blaser (2000) and uses particles in an interpolation window for getting the interpolated value on each node of the grid. The interpolation window was chosen to have on an average 10 particles in it. The velocity at the  $i^{th}$  node is given by equation (6.6).

$$u_i(x_c) = \frac{\sum_{n=1}^{N_v} \alpha^n u_i^n}{\sum_{n=1}^{N_v} \alpha^n} \quad (6.6)$$

$$\alpha^n = \exp\left(\frac{-(x_c - x^n)^2}{H^2}\right) \quad (6.7)$$

where  $\alpha^n$  is the weight applied on the vector based on the distance from the position of the center of the window i.e.  $x_c$ . According to Agüí and Jiménez (1987) the Gaussian window width  $H$  has an optimum value of  $1.24\delta V$  with a mention that it can be adjusted according to the flow field. In the current case  $H = 1.24\delta$  is chosen where  $\delta$  is the mean distance between particles and is defined as equation (6.8). Where  $A_I$  is the area of the

interpolation window and  $N$  is the number of velocity vectors ie. the number of particles in the window.

$$\delta = \sqrt{\frac{A_I}{N}} \quad (6.8)$$

For the PIV method an approximate approach has been adopted in which the velocity vectors in an interrogation window are averaged and the value allotted to the center of the window. The size of the interrogation window has been chosen such that on an average 8 particles are present in each interrogation window. Also in order to keep the grid size same in all the methods, an overlap is set such that the center of each window is on the node prescribed grid size.

## 6.5 Grid Size Selection

Considering the computational expense involved in numerical problems, deciding a grid size is an important step. The grid size decides the number of variables in the system and the number of nodes where the solution has to be computed. It must be such that the desired spatial structures are not filtered out while not being too large to unnecessarily increase the computational expense. In short its size has to be a compromise on the spatial resolution and computational budget. In order to decide on the grid to be used, a parameter is defined which represents spatial resolution achieved in the reconstructed field. It is called as the damping of the reconstructed field and is defined as the ratio of the reconstructed vorticity peak to that of the analytical vorticity peak, as shown in equation (6.9).  $D$  is always less than 1 because a numerical method always provides an approximate solution of the analytical flow.

$$D = \frac{\omega_{Rpeak}}{\omega_{Apeak}} \quad (6.9)$$

Figure 6.6 presents the variation of the damping with respect to the number of particle in the measurement domain. The damping has been calculated based on the reconstructions of the linear interpolation method. It has been plotted for grid sizes of  $100 \times 100$ ,  $20 \times 20$  and  $10 \times 10$ . The grid size of  $100 \times 100$  is a very fine mesh containing 10000 nodes in the computational domain. As the number of infused particles in domain increase, the reconstruction quality improves there by increasing  $D$ . The curve rises steeply for low number of particles but flatten out for large seeding densities. For the  $100 \times 100$  grid, the curve flattens and reaches  $D \approx 1$  for more than 1000 particles. This indicates that the linear interpolation reconstruction almost fully resolves spatial structures for more than 1000 particles when computed on a  $100 \times 100$  grid. For smaller grid sizes the maximum value of  $D$  attained is smaller indicating smaller resolution capacity. For a  $20 \times 20$  grid, maximum  $D$  is approximately 0.9 while for  $10 \times 10$  grid the maximum reaches at  $D \approx 0.7$ . This can also be interpreted as, at high seeding densities the  $20 \times 20$  grid provides a resolving capacity of 90% while the  $10 \times 10$  resolves 70% of the peak vorticity.

The computational expense generally increases with  $N$  (number of grid point) at an order of  $O(2)$ . This essentially means that the  $100 \times 100$  grid is more than 25 times expensive

as compared to the  $20 \times 20$ . Hence, the  $20 \times 20$  grid size is chosen which provides large computational benefits compared with a loss of not so significant spatial resolution. It should also be noted that the present study will be more focused towards the lower seeding densities where the disparity in resolution capacity between  $20 \times 20$  and  $100 \times 100$  is even less.

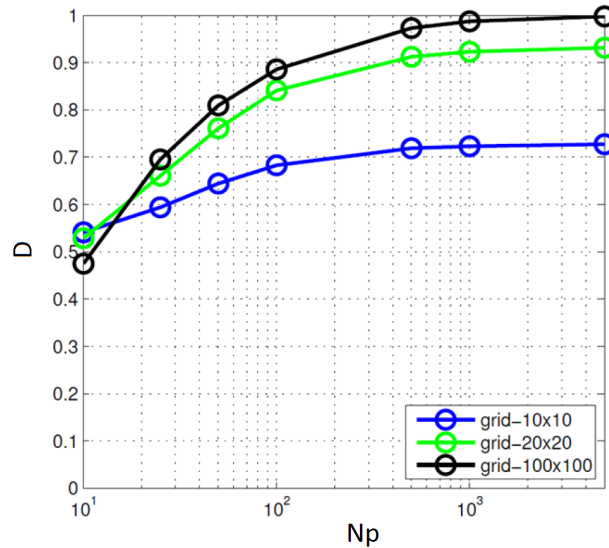


**Figure 6.6:** Damping on various grid size of 10,20 and 100

## 6.6 Boundary Conditions

The discussion on the boundary condition in chapter 4 clearly points out that the proposed method does not take the domain boundary into consideration and computes the optimised field only at the inner nodes. It has also been proposed that the boundary conditions at all time instances are to be taken from the input tomo-PIV flow fields at the respective times. For the present synthetic test case, no such measurement exist and the input of the analytical boundary condition would be too trivial and would unfairly play an enhancing role in the flow field optimisation.

An alternate solution to the issue of the domain boundary conditions can be solved by increasing the computational domain so that the boundary of the measurement domain is inside the computational one. For the present study, homogeneous padding type boundary conditions are applied with a padding of 30% of the side of the domain. The imposed boundary condition is similar to that used by Schneiders et al. (2016a) shown in figure 6.7.

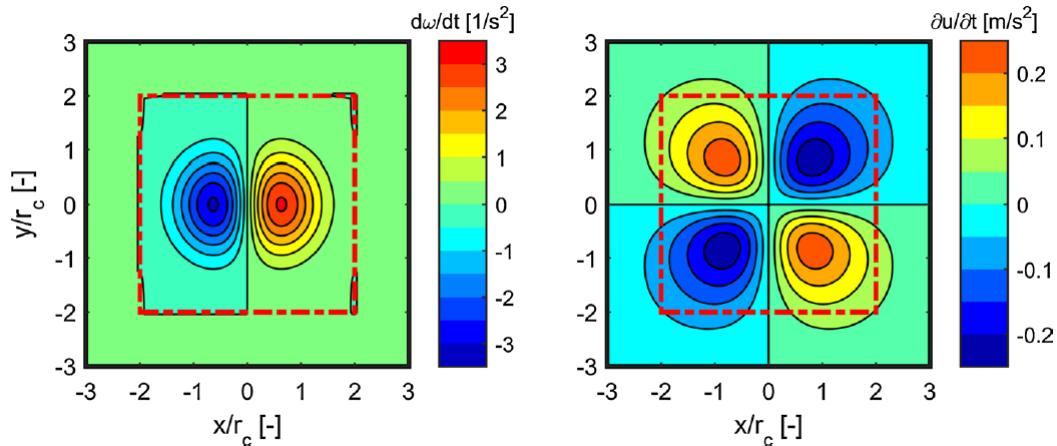


**Figure 6.7:** Padded Boundary Conditions (reproduced from Schneiders et al. (2016a))

The velocity boundary conditions for the computational domain is a simple Dirichlet boundary condition with the velocity components being equal to that of the free stream. This is shown in figure 6.8 where the red area is the measurement domain while the blue one is the padded region.

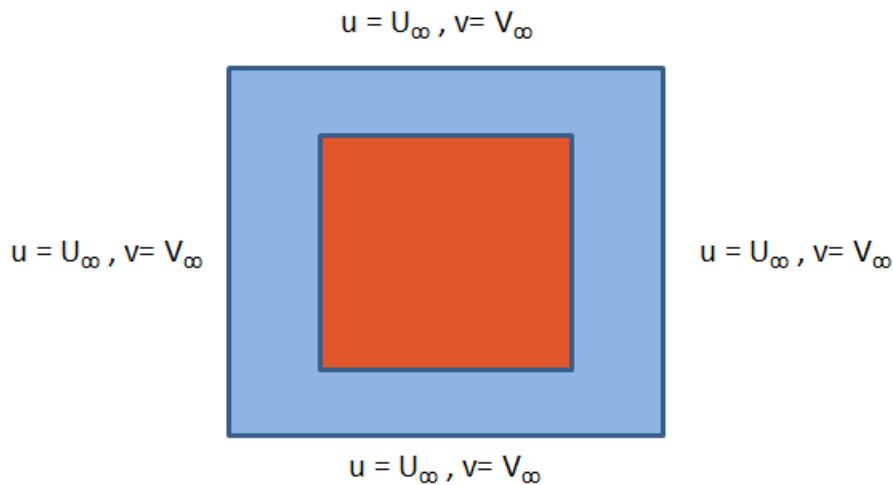


**Figure 6.8:** Dirichlet Boundary Conditions

## 6.7 Numerical Assessment

The parameters used for the numerical assessment of the synthetic vortex blob are presented in table 6.1. A detailed parametric study is done in the following chapters and some of the parameters presented here may be altered as required. The measurement domain is chosen to be a square with each side having length  $L$ . The size of the vortex blob is selected such that the side of domain is  $5r_c$  and at the initial time the blob is centrally located in the domain. The size of the vortex blob is intentionally kept significantly large, in order to facilitate the visual inspection of the different contours of the theoretical as well as

reconstructed fields. Also for simplicity, no translational velocity is considered. A number of synthetic snapshots are generated by calculating the scattered velocity measurements at particle locations from the analytical flow field. The time separation between two snapshots is  $dt = 0.2s$  and the total time used for the measurement is  $T = 20s$ , amounting to  $N_t = 40$  snapshots. For the present assessment 10 tracer particles have been introduced in the flow field. A grid size of  $20 \times 20$  is used for reconstruction using all the methods.

**Table 6.1:** Vortex blob test case simulation parameters

Parameter	Value	Unit
$\Gamma$	100	$cm^2/s$
$\gamma$	1.256	-
$dt$	0.2	s
$T$	20	s
$u_t$	0	cm/s
$v_t$	0	cm/s
$L$	20	cm
$r_c$	4	cm
<i>Padding</i>	30	%

The investigation is done to compare linear interpolation, AGW and PIV with the VIC++ method with respect to the reconstruction quality of the respective methods. Initially a qualitative assessment is done by comparing the contour plots of the instantaneous velocity fields. The contours of  $u$  component of velocity is shown in figure 6.9. The red dots represent the particle tracks used for reconstruction of a particular method. The linear interpolation AGW and PIV method use just instantaneous data, hence instead of tracks just the particle locations are shown. The reconstruction using linear interpolation produces exact values at the particle locations but between the locations the reconstruction quality is highly influenced by the low seeding concentration. The two distinct peaks visible in the analytical case are not reproduced by the linear interpolation and even the overall contour shape is also distorted. The approximate PIV method adopted in here filters most of the contours. The interrogation window in this case is quite large due to the presence of very small number of particles, which in turn results in this spatial filtering effect. This is in accordance to the discussion in the preceding section. Similar output is expected of the AGW and although it is a bit better than the PIV, visually it seems worse than the linear interpolation.

The instantaneous reconstruction of the Eulerian flow using the VIC++ method has been done using particle tracks of varying time length, ranging from  $N_t = 2$  to  $N_t = 40$  snapshots. The case with  $N_t = 2$ , involves integration over just one time step which means that still not much of flow information is provided to the method. In this case the method largely enforces and produces a divergence free flow field. As the VIC++ method is based on a physics based reconstruction, much better and accurate results are expected on the nodes between the particle locations. This is quite evident from figure 6.9(d), where the contours are much more regularised as compared to the other methods. When more information about the flow field is provided to the method in the form of more snapshots or longer time lengths, even further improvement in the accuracy and

shape regularization is expected. This can be observed in the contour plot of VIC++ with  $N_t = 5$  to  $N_t = 40$  as shown in figure 6.9(e) to (h).

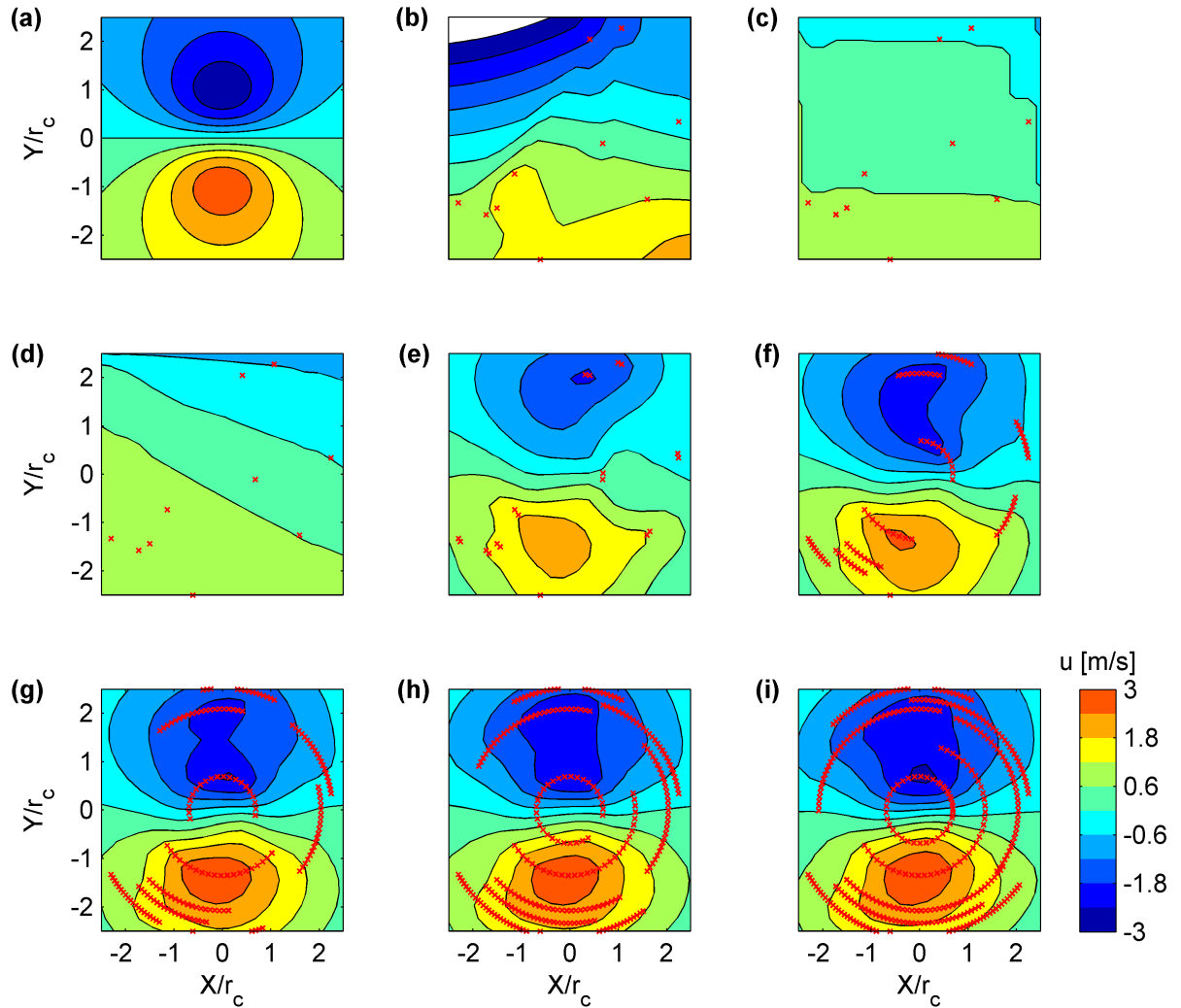


**Figure 6.9:**  $u$  component of velocity contours for 10 particles. (a) Analytical (b) Linear Interpolation (c) PIV (d) AGW and (e) to (i) VIC++ for  $N_t = 2, 10, 20, 30, 40$  respectively

For  $N_t = 40$  the velocity contours are almost symmetric about the centre line, which is the case in the analytical flow. The flow velocity around the edges of the domain have lower velocity as compared to the reference case, this is because of the absence of particles around these locations. Also the boundary conditions applied are approximate which causes the accuracy to drop near the boundary edges. A more closer analysis will be presented in chapter 7. A similar trend to the  $u$  contour plots is also observed for the contour plots of the  $v$  component of velocity presented in figure 6.10 with the quality of VIC++ being higher than the other methods and producing more accurate and regularised results with increasing time lengths.

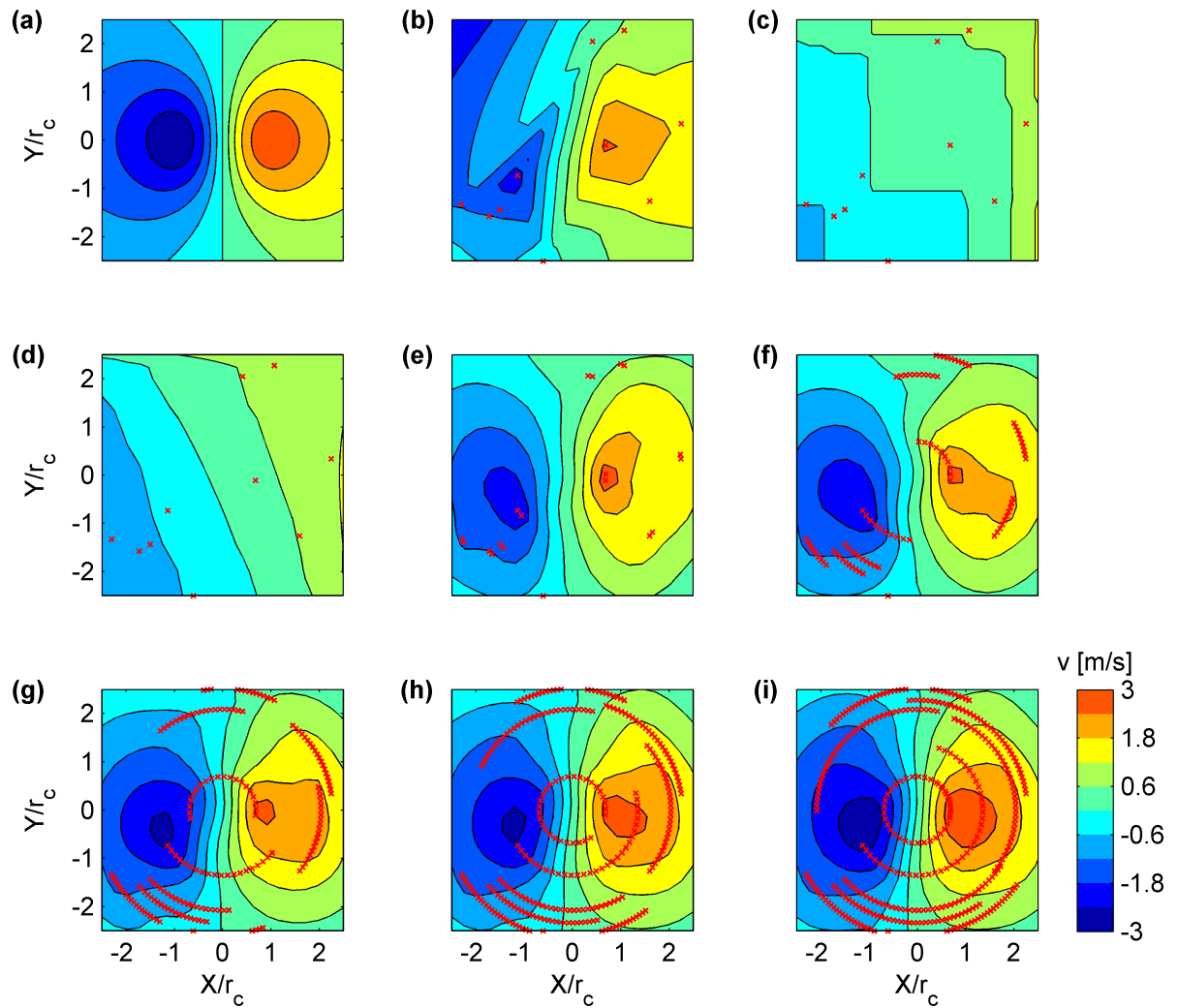


**Figure 6.10:**  $v$  component of velocity contours for 10 particles. (a) Analytical (b) Linear Interpolation (c) PIV (d) AGW and (e) to (i) VIC++ for  $N_t = 2, 10, 20, 30, 40$  respectively

The vorticity contour plots are shown in figure 6.11. Again the AGW and approximate PIV method perform not so well and filter out almost all the contour lines. The linear interpolation as well fails miserably to reconstruct the blob. When the VIC++ method for  $N_t = 2$  is used, some contours of the blob are visible, still the reconstruction is not so regular. The main reason behind this improvement as compared to linear interpolation, AGW and PIV is because the method uses vortex methods which enable it to reconstruct the vortical structures. Similar to the velocity contours, the vorticity contours also regularises and become more accurate for VIC++ method with larger values of  $N_t$  and becomes almost synonymous for  $N_t = 40$ . Some negative vorticity can be observed around the boundary in the VIC++ reconstructions which mainly arise due to homogeneous fixed boundary conditions.

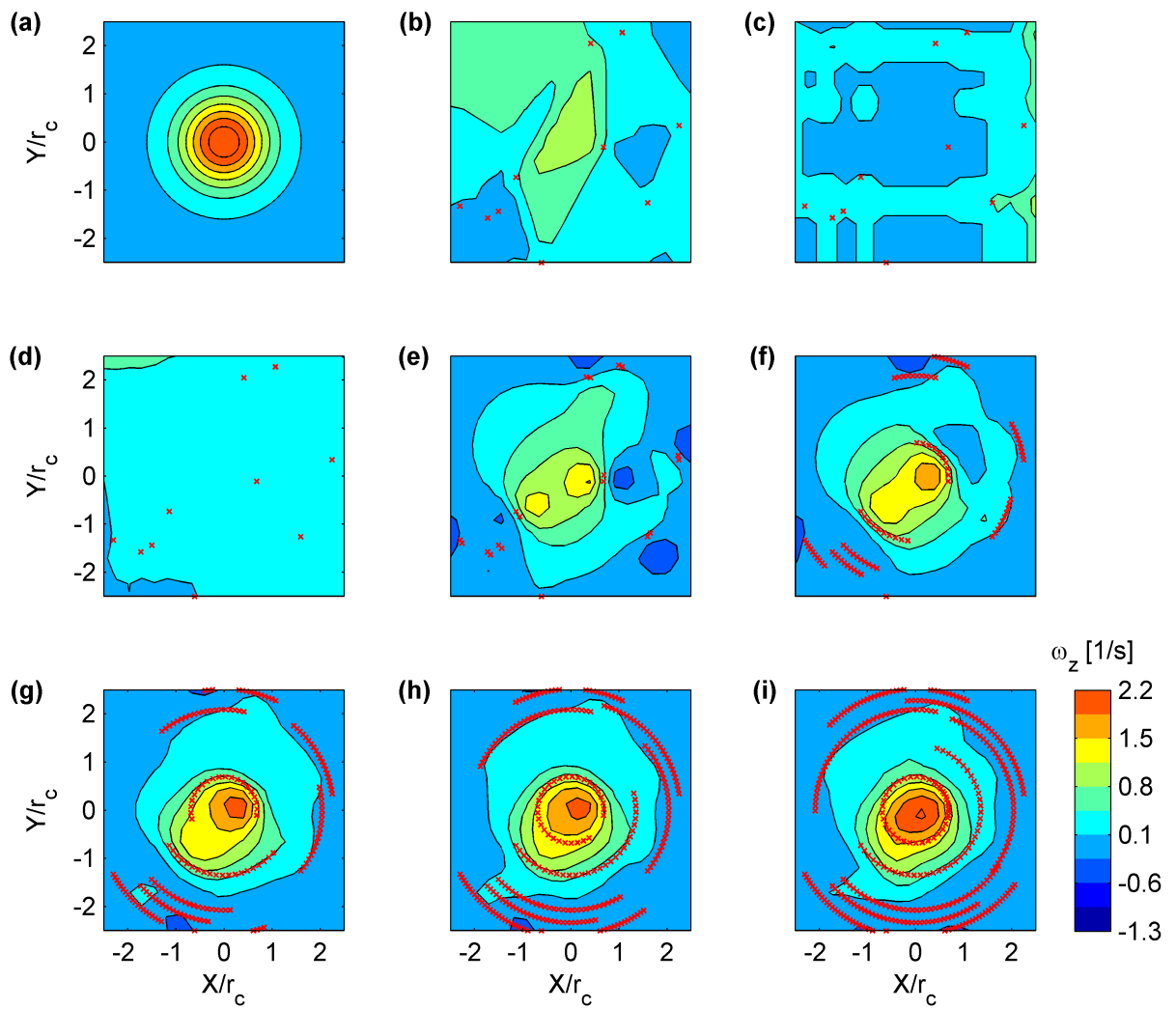


**Figure 6.11:** Vorticity contours for 10 particles. (a) Analytical (b) Linear Interpolation (c) PIV (d) AGW and (e) to (i) VIC++ for  $N_t = 2, 10, 20, 30, 40$  respectively

## 6.8 Comparison of Velocity Profiles

It is important to note that the comparison done above are for one realisation or sample, i.e. one set of particle tracks. Thus it is not fair to completely judge the methods based on one case. A more closer comparison is done by plotting the profiles of  $u$ ,  $v$  velocity and the vorticity along the central lines of the domain as shown in figure 6.13. In order to plot these profiles 100 random samples have been considered with 10 tracer particles. Firstly the profiles of linear interpolation method and the VIC++ methods with  $N_t = 2$  are compared. Linear interpolation is chosen over AGW and PIV for the comparison because it fares well in the analytical case over the other two methods. The profiles for this comparison is plotted in figure 6.14. Next the VIC++ method with shorter tracks ( $N_t = 2$ ) is compared to the one using long tracks ( $N_t = 40$ ) in figure 6.13. In all the three subfigures (a),(b) and (c) of figures 6.13 and 6.14 the black line represents the profile of the analytical or reference case. The line represents the mean profile of the reconstructed field over 100 samples while the shaded area shows the standard deviation of the results from their respective mean profiles.

### 6.8.1 Linear Interpolation vs VIC++

The blue colour represents the VIC++ method with  $N_t = 2$  snapshots while the profiles linear interpolation methods is displayed in yellow. When inspecting the  $u$  velocity and  $v$  velocity profiles, it is observed that the linear interpolation method hardly captures the velocity peaks. In both the sub-figures the linear interpolation profiles are almost a straight line. On the other hand, the velocity profiles of the VIC++ method with  $N_t = 2$ , represent the analytical case in much improved way. Even though the peak velocity is still not fully captured, it follows the curvature of the analytical case much more faithfully than the linear interpolation case. The standard deviation (shaded area) associated with the linear interpolation is larger for both the velocity profiles, indicating more robustness and lower sensitivity to particle location for the VIC++ method with  $N_t = 2$ . The vorticity profile compared in figure 6.14(c) reveals that the spatial resolution achieved in the VIC++ method is higher than what achieved through the linear interpolation.

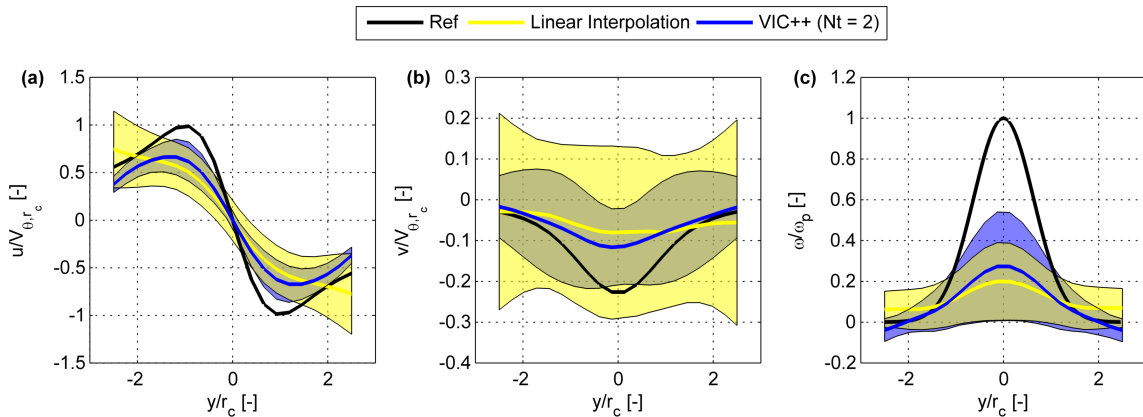


**Figure 6.12:** Comparison of linear interpolation (yellow) and VIC++  $N_t = 2$  (blue). Mean profile (line) along the central  $y$ -axis with standard deviation (shaded area) for (a)  $u$  velocity (b)  $v$  velocity (c) vorticity

### 6.8.2 Short vs Long Tracks

VIC++ method with  $N_t = 2$  is again represented by blue colour while VIC++ with  $N_t = 40$  is represented by red. It can be clearly be observed that the red line closely follows the reference black line as compared to the blue one which means that VIC++ with longer particle track is able to reconstruct more accurate velocity as well as vorticity field. Another notable point is the higher peak values observed for the red curve which emphasizes on higher resolution attained by the method using longer tracks. Even the standard deviation for  $N_t = 40$  case is much lower and shows that the methods accuracy is less particle position dependent and the robustness of the method increases when using longer tracks.

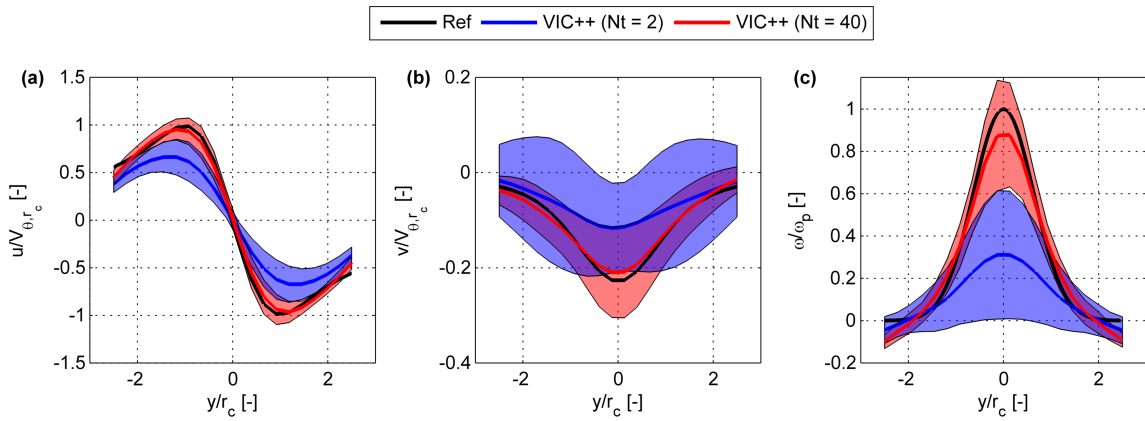


**Figure 6.13:** Comparison of VIC++  $N_t = 2$  (blue) and VIC++  $N_t = 40$  (red). Mean profile (line) along the central  $y$ -axis with standard deviation (shaded area) for (a)  $u$  velocity (b)  $v$  velocity (c) vorticity

## 6.9 Tracer Concentration

When using higher seeding concentration, the root mean square (RMS) error shows a declining trend, which is expected because more data is available for the reconstruction on the same grid. The VIC++ method fares much better compared to the linear interpolation, AGW and PIV. The RMS error for the VIC++ method with  $N_t = 2$  is approximately **25%** lower than the linear interpolation method when using 10 particles in the measurement volume. The VIC++ with larger  $N_t$  produces reconstructions with reduced error. The relative error between the reconstruction of the VIC++ method using different time lengths decreases with increasing number of particles, meaning that the relative advantage of using the method with longer tracks diminishes with the increase in the particle densities.

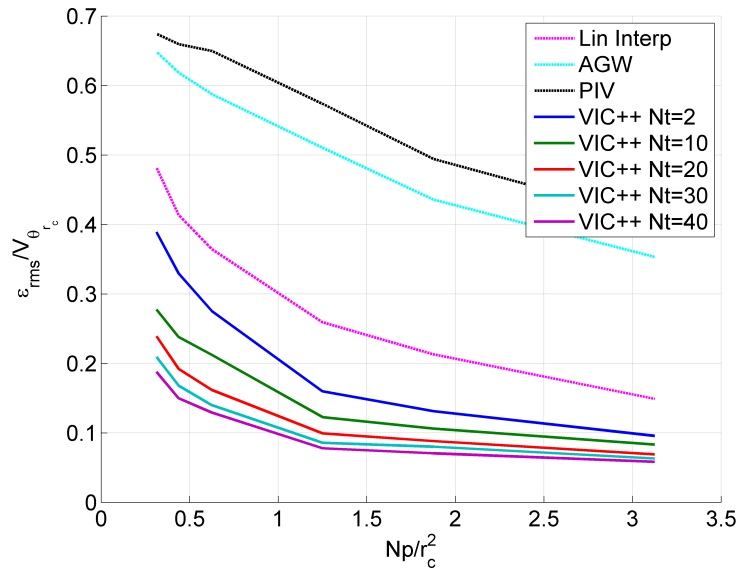


**Figure 6.14:** RMS error (normalised with peak velocity) with varying number of particles for different  $N_t$ .

## 6.10 Time Length

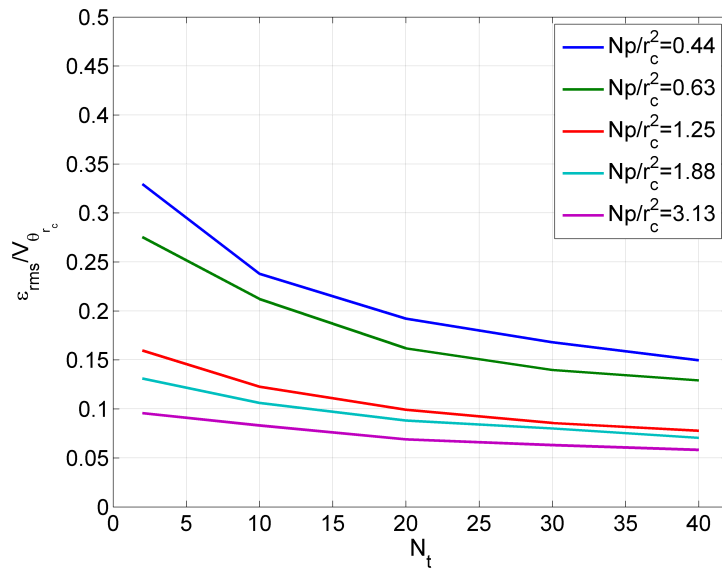


**Figure 6.15:** RMS error (normalised with peak velocity) with varying  $N_t$  for different particle densities.

In figure 6.16 the RMS error is shown with the increasing snapshots provided to and utilised by the VIC++ method for the instantaneous flow field reconstruction. This plot is made for different particle densities. It is observed that the RMS error decreases when using longer particle tracks as an input to the proposed method. Another interesting

aspect which is observed is that the slope of the curve is high in the low  $N_t$  region while it gradually starts to show a flattening behavior when considering large time lengths. This behavior becomes more pronounced when considering the case with higher seeding concentration. This signifies that even though increasing time length decreases the error, the benefit gradually reduces with the addition of more snapshots as an input to the method. Also when higher values of  $N_t$  are considered the computational cost rises significantly. Thus the ultimate result will be a trade-off between the accuracy desired and the computational expense budget. The flattening effect can also be attributed to the finite grid size opted for the computations.

### 6.10.1 Time Length with Different Grid Size

The RMS error with increasing time lengths is presented in figure 6.16 for two grid sizes, namely a grid of 15(left) and 25(right). As compared to the previous section (grid size of  $20 \times 20$ ) all the parameters involved in the numerical simulation except the grid size are same. The most important thing to be observed is the slope of the curve for larger grid is more i.e. the flattening effect observed for large values of  $N_t$  is more prominent in case of the smaller grid. For the same seeding density the relative gain in the reconstruction quality for longer tracks is higher.

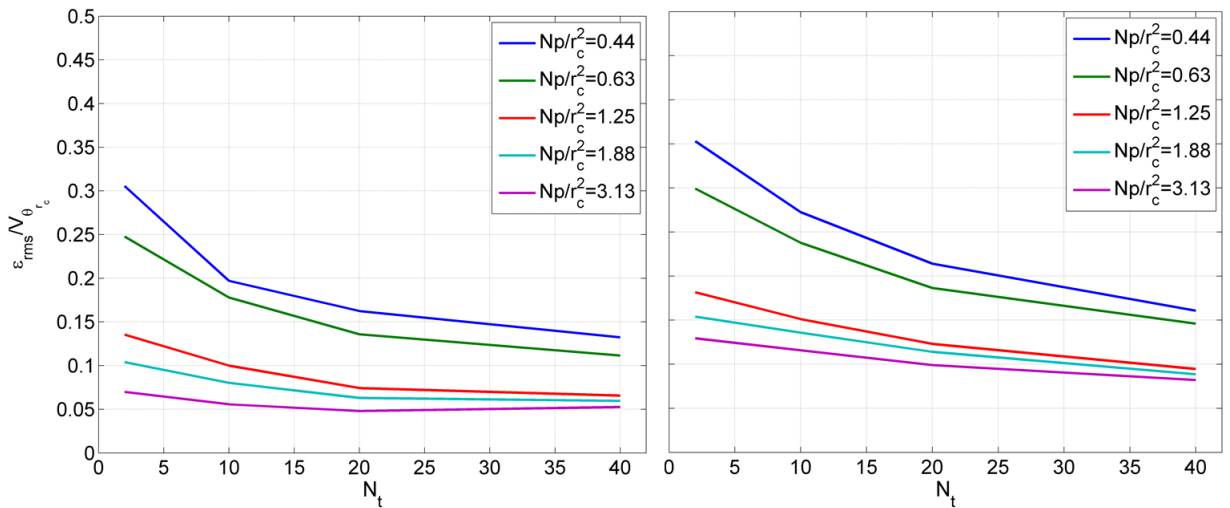


**Figure 6.16:** RMS error (normalised with peak velocity) with varying  $N_t$  calculated on a Grid of 15 (left), 25 (right).

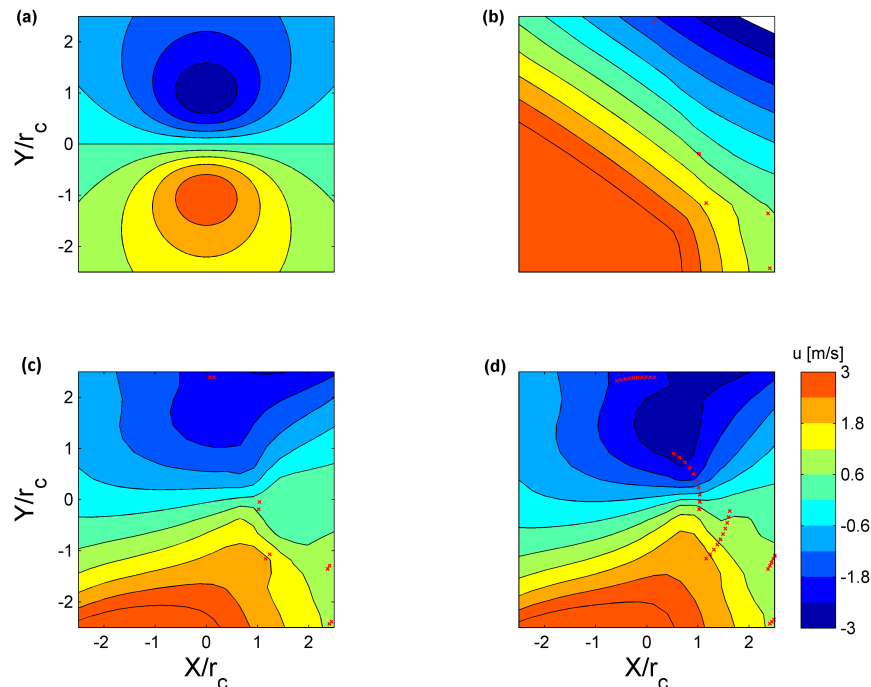
## 6.11 Initial Conditions

The initial condition of an optimisation problem is extremely important for the output as well as the computational cost involved. A good initial condition can greatly reduce the computational expense required and produce better results while a bad initial condition does the opposite. As stated in earlier sections the VIC++ method intends to use the gridded tomo-PIV data as the initial condition. For the present case with very low particle densities and synthetically produced data it is not available. Also as mentioned earlier the linear interpolation produces better results as compared to other conventional

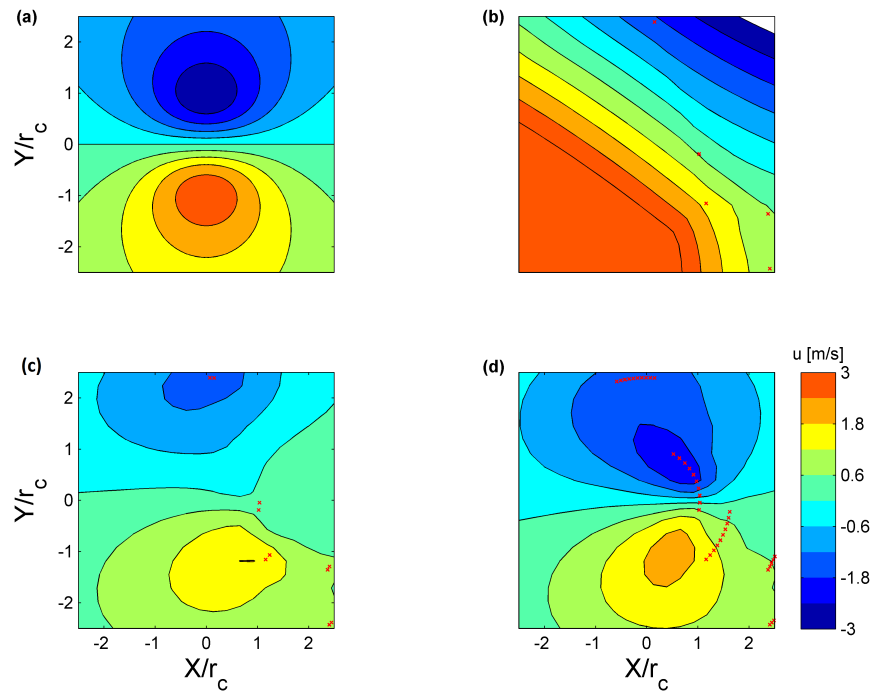
methods for the analytical case and its reconstructed flow field can be used as the initial condition.

Figure 6.17 shows the VIC++ reconstructions with the initial condition taken from the linear interpolation data. It is observed that even though the reconstructions improve with the increasing time lengths, they are highly influenced by the initial condition which in this case is provided by linear interpolation. As the velocity field predicted by the linear interpolation is poor, the VIC++ optimisation process start with the poor and erratic field and changes it.

The optimisation problem at hand is an ill posed problem, meaning that the solution sensitivity to the changes on the initial conditions is very high. This further means that a bad initial guess may deem the solution to be erratic as well. Instead of going for the poor linear interpolation initial condition, it was decided to use the initial filed of all zeros i.e. zero initial condition. It is expected that optimisation results will be devoid of the local erratic peaks present in the linear interpolation velocity field at time  $t_0$ . To validate this the VIC++ velocity fields were again computed using the same particle tracks and tolerance but with zero initial condition, as shown in figure 6.18. It can be observed that the reconstructed fields computed by the VIC++ using zero initial condition is much more regularised in the overall shape of the contours as compared to when using linear interpolation initial conditions. It is also free of the local peaks observed in the former case. All the optimisation process in the document follow the zero initial conditions.



**Figure 6.17:**  $u$  velocity contours with initial condition computed using linear interpolation. (a) analytical (b) Linear interpolation (c) VIC++ with  $N_t = 2$  (d) VIC++ with  $N_t = 10$  (5 particles).



**Figure 6.18:**  $u$  velocity contours with zero initial condition. (a) analytical (b) Linear interpolation (c) VIC++ with  $N_t = 2$  (d) VIC++ with  $N_t = 10$  (5 particles).

## 6.12 Analysis with Noisy data

The assessment done above is without consideration of any noise in the input velocity of the particle tracks. This section focuses on the scrutiny of the performance of different methods (especially the VIC++) under the presence of noise in the input reference field. For this a white Gaussian noise is added to the particle velocity. Around 1000 particles are introduced in the flow and reconstruction of the velocity and vorticity fields is done by different methods. Such a high seeding density is purposefully considered so that the effect of noise is prominently visible in the contours. In the absence of noise, at such seeding density, all the methods produce highly accurate fields. It is interesting to gauge their ability for a noisy data set.

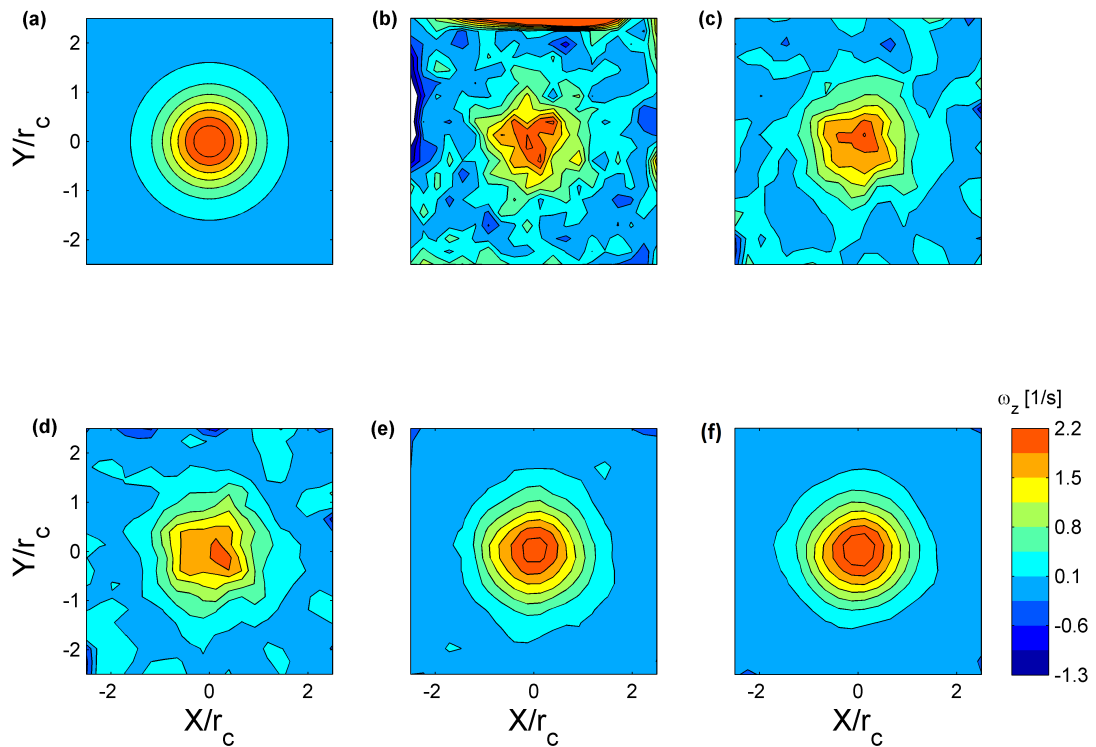


**Figure 6.19:** Vorticity contours with white Gaussian noise.(a) analytical (b) Linear interpolation (c) PIV (d) AGW (e) VIC++ with  $N_t = 2$  (f) VIC++ with  $N_t = 10$  (1000 particles).

The vorticity field contours for linear interpolation, PIV, AGW and VIC++ reconstructions with  $Nt = 2$  and 10 are plotted in figure 6.19. The linear interpolation produces worst results in this case with very noisy reconstruction. This is consistent with the discussion made in the previous section 6.4 regarding the inability of linear interpolation to handle noisy data because it just fits data through the points and does not apply any filtering technique. The PIV does comparatively better and filters out some noise. Its reconstruction quality is excelled by the AGW method which produces more regularised

field. The weighted averaging involved in the method provides further filtering. Still a lot of aberrations is seen in the reconstructed field of both the methods. This is essentially because the aforesaid methods are mathematical tool and do not consider the flow physics involved.

The VIC++ method is a flow physics based technique, which enforces the divergence free criteria in each integration time step. It filters out almost all the noise present in the input velocity and reconstructs highly regular vorticity contours. The reconstruction is further improved when long tracks are considered and the resultant vorticity contours almost exactly match with the analytical case. A similar observation is followed in the reconstruction of  $u$  velocity contours as shown in figure 6.20. This test case proves the noise reduction ability of the VIC++ method

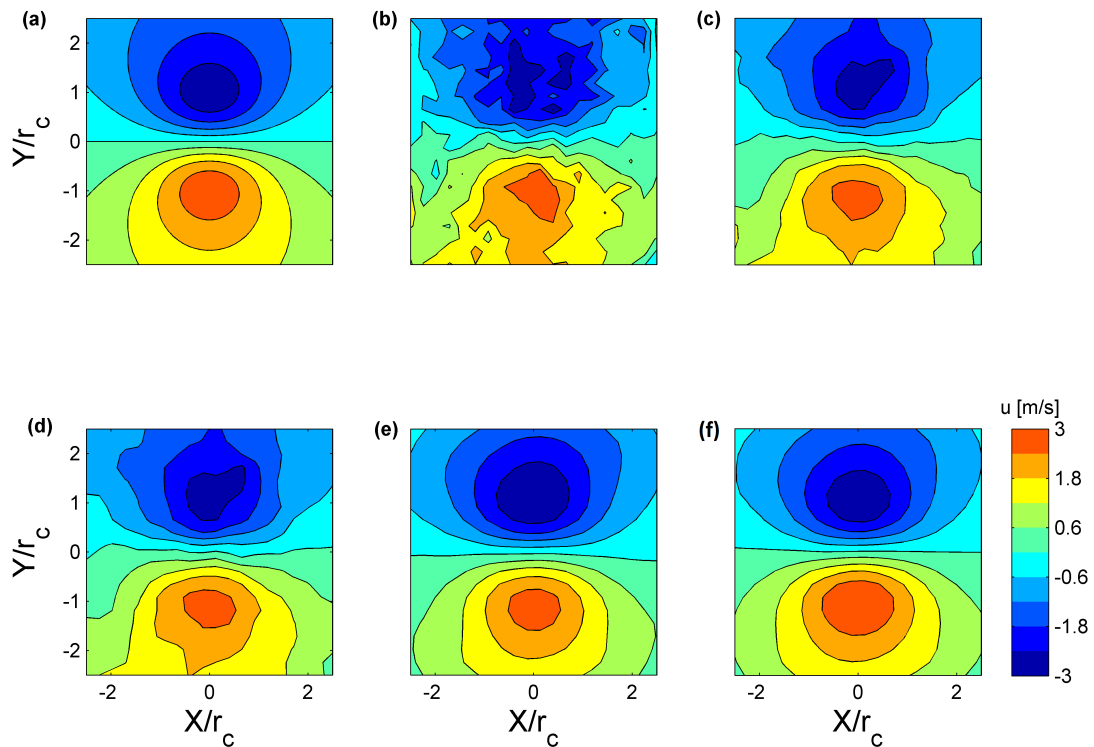


**Figure 6.20:**  $u$  velocity contours with white Gaussian noise. (a) analytical (b) Linear interpolation (c) PIV (d) AGW (e) VIC++ with  $N_t = 2$  (f) VIC++ with  $N_t = 10$  (1000 particles).

# Unsteady Flow Regime

The numerical assessment in the previous sections is performed on the vortex blob which is representative of steady flow case because of the unvarying shape of the blob. This chapter presents an implementation of the proposed method in the unsteady flow regime. As the 3D extension of the method could not be done in the available time frame, this case is also concerned with a two dimensional flow. For this purpose a laminar Von-Karman shedding resulting due to the flow over a long cylinder is investigated. The study does not intend to look upon the physics involved in the flow itself but rather study the application of the method to reconstruct the instantaneous data. This would give a more thorough test to the method, as it would deal with flow with evolving vortexes.

### 7.1 Two Dimensional Cylinder Vortex Shedding

Flow over a cylinder has been extensively studied from the early part of the twentieth century. A detailed overview of most of the experimental as well as numerical analysis of different forms of the case is presented in Zdravkovich (1997). These type of flows can be characterised into various regimes as presented in figure 7.1. For flows in the range of  $Re$  40 to 200, laminar and periodic vortex shedding is observed. Flow in this region essentially behaves like a two dimensional flow with no variation in the span-wise direction, as pointed out by Williamson (1989) amongst others (Sumer & Fredsøe, 1997)(Rajani et al., 1997). Beyond this regime, primary instabilities are induced in the cylinder's wake, which cause the span-wise component of flow to amplify. Due to the evolution of this component, the over all structures of the flow are altered which renders the flow to be not accurately represented by the solution provided from two dimensional flow solvers.

The present work will be focusing in the laminar regime where the flow can be represented faithfully using a two dimensional model. The specific details of the computational simulation is discussed in the following section.

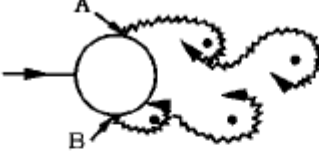
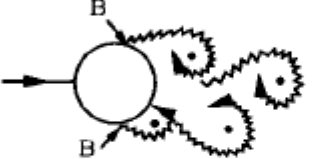
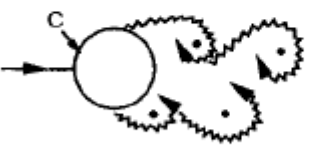
a) 	No separation. Creeping flow	$Re < 5$
b) 	A fixed pair of symmetric vortices	$5 < Re < 40$
c) 	Laminar vortex street	$40 < Re < 200$
d) 	Transition to turbulence in the wake	$200 < Re < 300$
e) 	Wake completely turbulent. A: Laminar boundary layer separation	$300 < Re < 3 \times 10^5$  Subcritical
f) 	A: Laminar boundary layer separation B: Turbulent boundary layer separation; but boundary layer laminar	$3 \times 10^5 < Re < 3.5 \times 10^5$ Critical (Lower transition)
g) 	B: Turbulent boundary layer separation; the boundary layer partly laminar partly turbulent	$3.5 \times 10^5 < Re < 1.5 \times 10^6$  Supercritical
h) 	C: Boundary layer com- pletely turbulent at one side	$1.5 \times 10^6 < Re < 4 \times 10^6$ Upper transition
i) 	C: Boundary layer comple- tely turbulent at two sides	$4 \times 10^6 < Re$ Transcritical

Figure 7.1: Flow regimes in a flow around a circular cylinder in a steady flow (reproduced from Sumer and Fredsøe (1997))

## 7.2 Computational Simulation

The experiment was performed in a numerical domain using the incompressible Navier-Stokes solver provided by OpenFOAM. The inlet flow to the domain is laminar with the free stream velocity as  $3 \times D$  m/s, where  $D$  is the diameter of the cylinder. The geometry of the test case along with the boundary conditions is presented in figure 7.2. All the dimensions in the figure are expressed in term of the cylinder diameter. The parameters of the numerical simulation are shown in table 7.1. The flow Reynolds number of the flow was chosen to be 150 in order to induce the laminar and periodic Von-Karman vortex shedding as discussed in the previous section. The computational mesh used is displayed in figure 7.3 and a zoomed in version of the mesh around the cylinder is also shown.

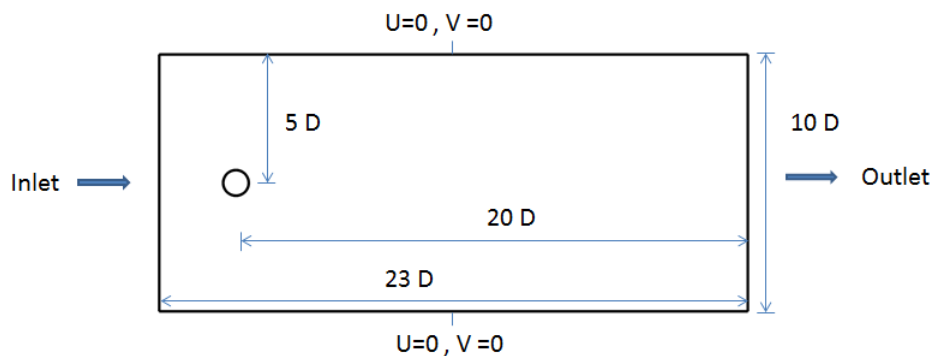


Figure 7.2: Geometry used for the numerical computation

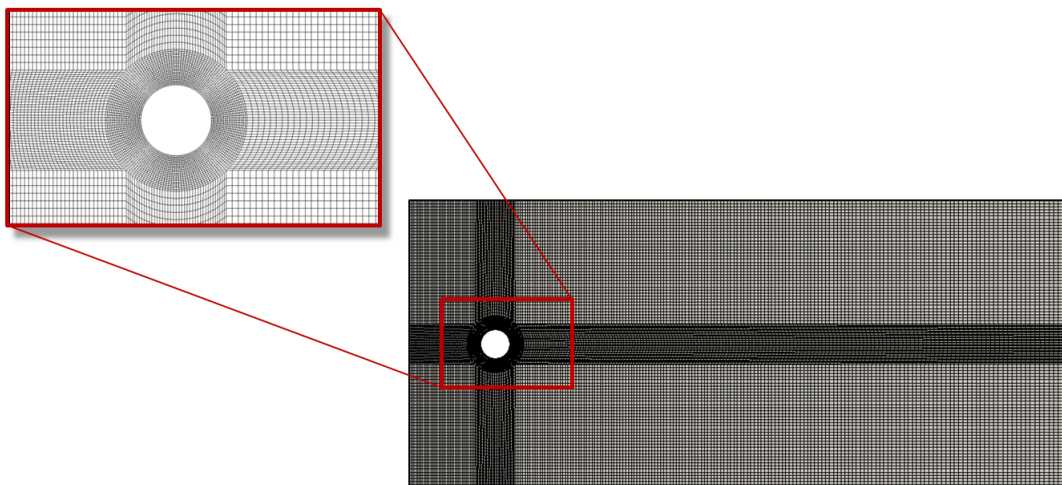
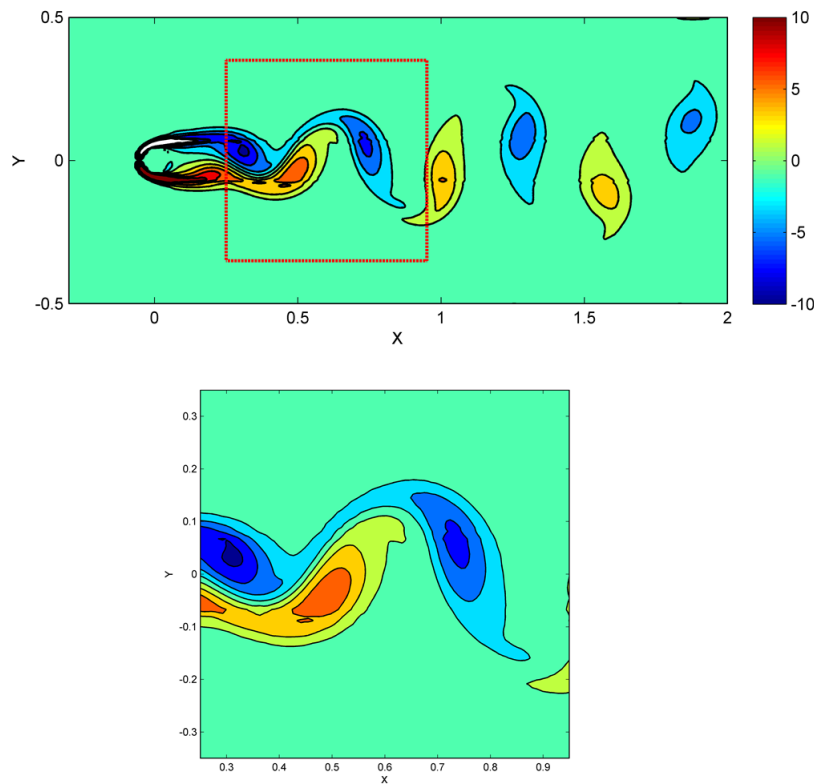


Figure 7.3: Mesh used for the numerical computation

**Table 7.1:** Von-Karman shedding test case simulation parameters

Parameter	Value	Unit
Re	150	-
$D$	0.1	m
$U_\infty$	0.3	m/s
$V_\infty$	0	m/s
$\nu$	$2 \times 10^{-4}$	$\text{m}^2/\text{s}$
No of nodes	30840	-

**Figure 7.4:** Vortex contours of Von-Karman Vortex shedding. Also shown is the section of the flow to be used for the analysis.

The reference velocity fields are available at very high temporal resolution, but for the present case, a sub-sampled data at time spacing of  $0.02\text{s}$  is extracted. At very high temporal resolution, representation of a substantial movement of particles would require large number of time slices. Considering the computational costs involved in the proposed method, approximately 50 time slices are taken into account. This temporal resolution is chosen such that the displacement of particles during the total time interval is around 3 to 4 times the cylinder diameter.

The flow is allowed to be fully developed and the periodic oscillations of the wake to be established. A fully developed oscillatory flow is considered as the initial condition

of the flow for the reconstruction. The vorticity contours of the computed flow at time  $t_0$  is shown in figure 7.4. The region of interest for the current work is in the wake of the cylindrical structure and thus it is unnecessary to consider the entire domain for further analysis. A square domain of dimension  $7D \times 7D$  at a distance of  $1D$  behind the cylinder is considered. This would enable the analysis of smaller scales of the wake. The domain is not chosen to be very close to the cylinder in order to avoid any influence of the fluid structure interaction and focus only on the evolution of the vortices in the wake. The velocity field in this domain is considered as the reference velocity field for the investigation of application of the proposed method to the unsteady flow test case.

### 7.3 Analysis

The analysis pattern remains same as done for the 2D vortex blob. Certain number of particles are introduced in the flow and the Lagrangian tracks computed. As the present case does not involve any analytical solution, the velocities at the particle locations are found from the velocities available at the fine mesh nodes using linear interpolation. These data sets at particle positions are synonymous to the PTV measurements.

The instantaneous velocity and vorticity field are reconstructed by linear interpolation, PIV, AGW and the VIC++ with different track lengths. The reconstruction is compared by first investigating the velocity and vorticity contours of various reconstructions, followed by the computation of the root mean square error of the respective reconstructed velocity fields with respect to the reference velocity field. For all the cases, a computational grid of  $30 \times 30$  is considered.

#### 7.3.1 Numerical Assessment with VIC++

The assessment is performed at very low seeding densities, where the currently available methods struggle to reconstruct at the required spatial resolution. For the first test case only 10 particles are infused in the flow and their information at all the time instances is computed. The instantaneous Eulerian flow field at time  $t_0$  for all the aforementioned methods have been computed.

A qualitative analysis is presented. Figure 7.8 presents the contour plots of the  $u$  component of velocity. The contours of the reference velocity field are shown in figure 7.8 (a) depicting the blobs of high velocity concentration alternately distributed around the low velocity central contours representing the vortex shedding. The reconstructed velocity field from the linear interpolation, PIV and AGW shown in figure 7.8 (b),(c) and (d) respectively, entirely fail to capture the reference velocity contours and the field is highly dominated by the free stream velocity, filtering almost entirely the velocity contours. This is expected because of the immensely low seeding concentration. The reconstruction of the VIC++ method utilising information provided by 2,5,10 and 20 snapshots are respectively shown in figure 7.8 (e),(f),(g) and (h). When looking at the VIC++ method with 2 snapshots, a significant improvement can be noticed as compared to its conventional counterparts. Some contours along the stream-wise direction of the cylinder can be observed to be reconstructed. Further regularisation is observed when adding more snapshots for the method, with the contours looking visually more similar to the reference field.

When observing the  $v$  velocity contours in figure 7.6, a similar trend as the  $u$  velocity is observed in accordance to the expectations. Three distinct structures are observed in the reference field which are only observable in the VIC++ reconstruction. The number of contour levels increase with leveraging of longer time series data, thus proving the better reconstruction ability of the VIC++ method with more flow information at its disposal.

The vorticity of field of a Von-Karman shedding comprises of alternate blobs of negative and positive vorticity being translated in the flow. The comparison of the respective vorticity field contours are presented in the figure 7.7. The linear interpolation method reconstructs a very small region of positive vorticity while totally ignoring the presence of any positive vorticity structures. These is highly influenced by the position of the particles in the domain. The AGW and PIV completely miss out every vortex and produce a highly filtered reconstruction. The VIC++ with short time lengths produce multiple small blobs of negative and positive vorticity and also some unwanted vorticity peaks. These become more and more regularised with the inclusion of longer tracks and only the required blobs are enlarged eliminating the local peaks.

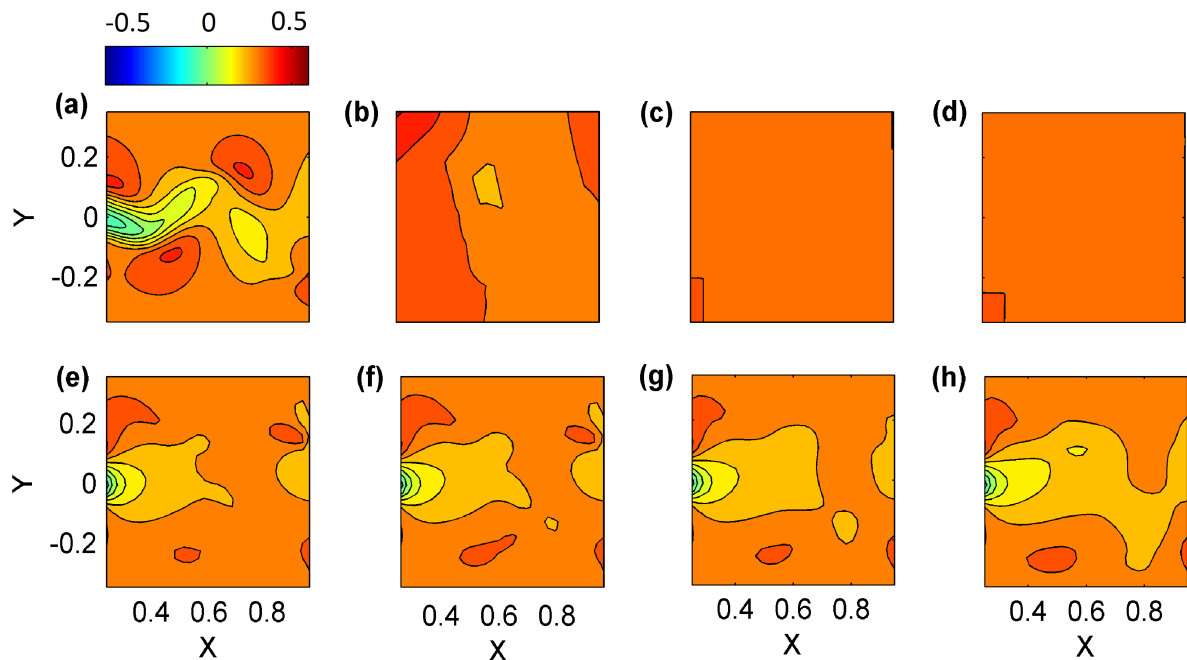


**Figure 7.5:**  $u$  velocity contours for 10 particles. (a) Numerical (b) Linear Interpolation (c) PIV (d) AGW and (e) to (h) VIC++ for  $N_t = 2, 5, 10, 20$  respectively

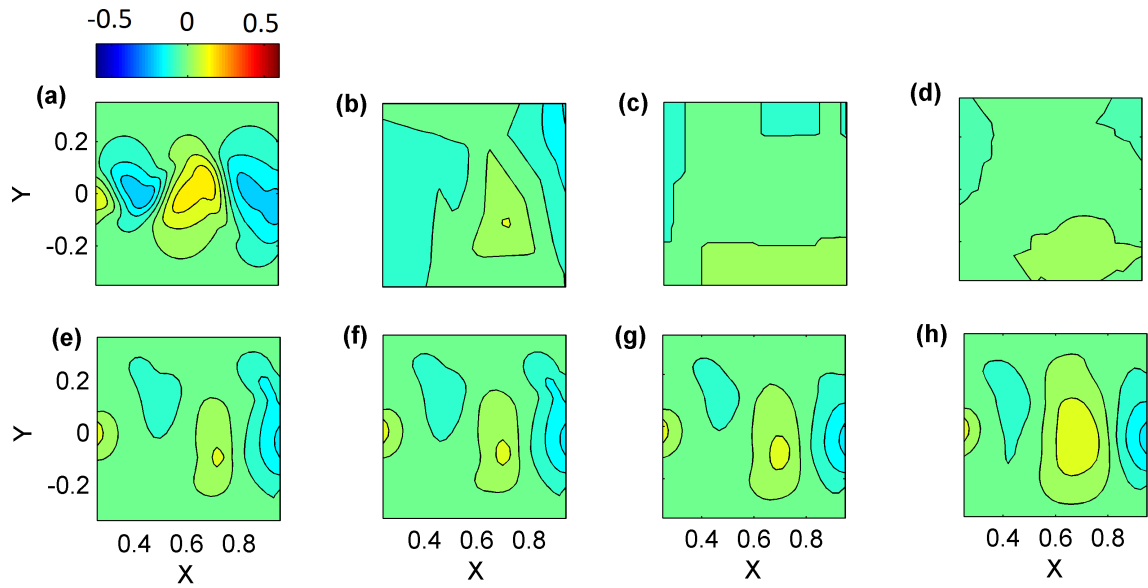


**Figure 7.6:**  $v$  velocity contours for 10 particles. (a) Numerical (b) Linear Interpolation (c) PIV (d) AGW and (e) to (h) VIC++ for  $N_t = 2, 5, 10, 20$  respectively

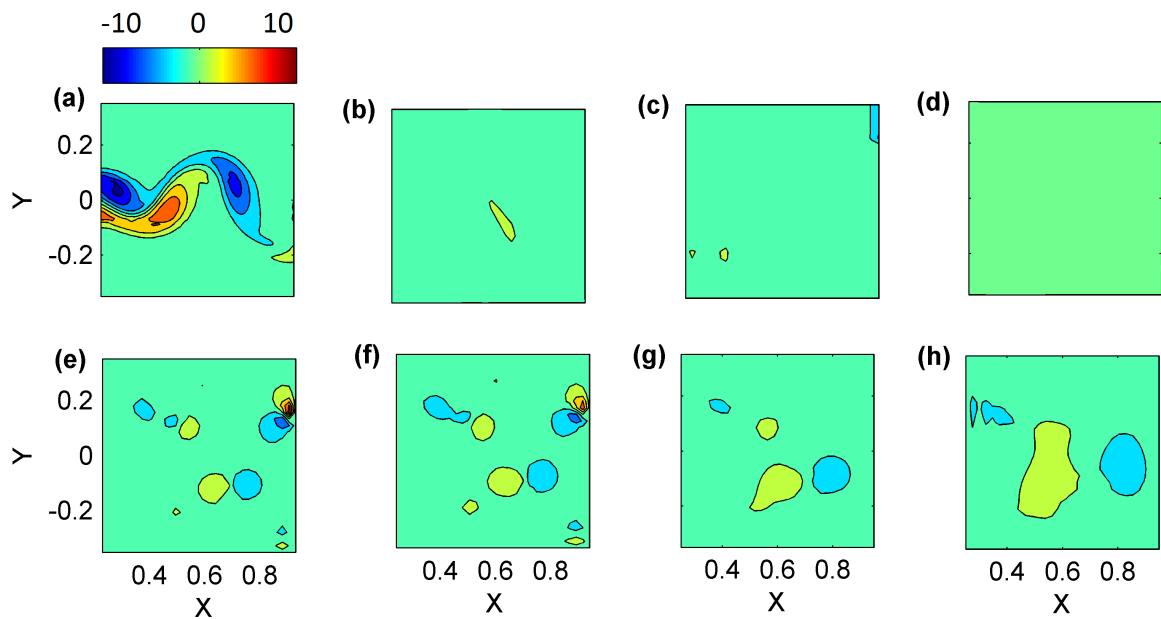


**Figure 7.7:** vorticity contours for 10 particles. (a) Numerical (b) Linear Interpolation (c) PIV (d) AGW and (e) to (h) VIC++ for  $N_t = 2, 5, 10, 20$  respectively

The qualitative inspection is again performed, with a test case having higher seeding density. In this case around 25 particles are introduced in the flow and the particle track data computed. Again the contours of the  $u$ ,  $v$  velocity fields and vorticity field are plotted, as shown in figures 7.8, 7.9 and 7.10 respectively. As the particle density is

higher, information at more points are available hence all the methods are expected to have better reconstructions as compared to the 10 particle test case.

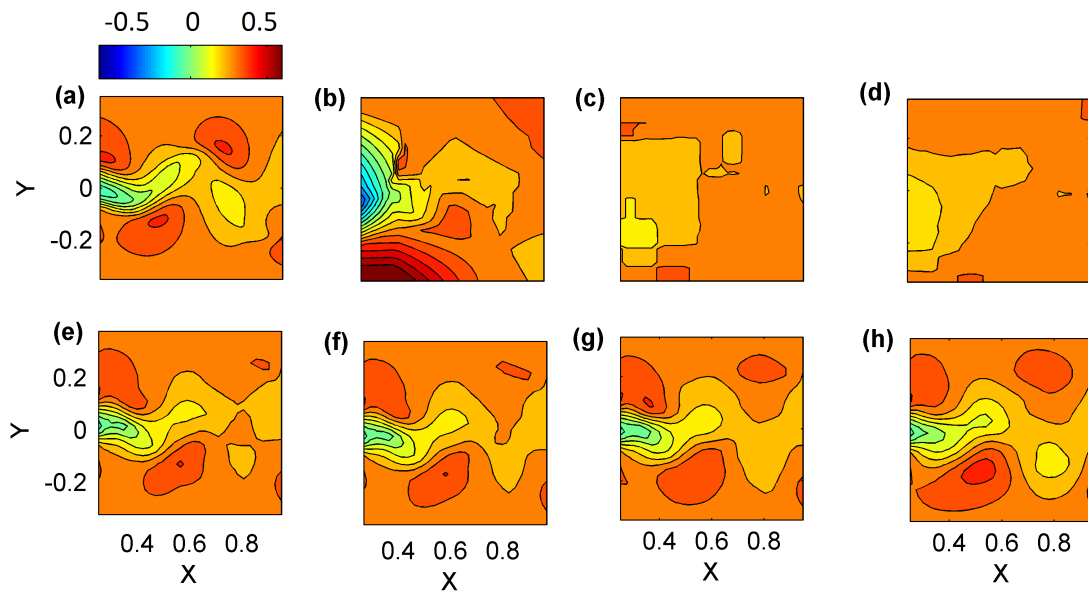


**Figure 7.8:**  $u$  velocity contours for 25 particles. (a) Numerical (b) Linear Interpolation (c) PIV (d) AGW and (e) to (h) VIC++ for  $N_t = 2, 5, 10, 20$  respectively

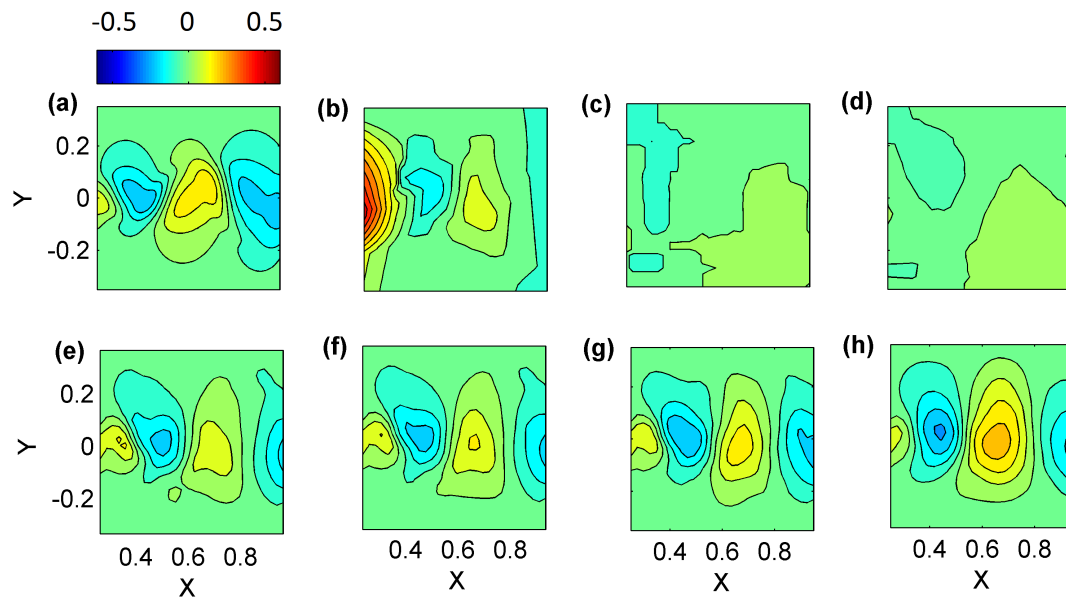


**Figure 7.9:**  $v$  velocity contours for 25 particles. (a) Numerical (b) Linear Interpolation (c) PIV (d) AGW and (e) to (h) VIC++ for  $N_t = 2, 5, 10, 20$  respectively

Looking at the  $u$  velocity contours the AGW method does the best amongst linear interpolation and PIV, but still is only able to capture half of the central low velocity contours. The VIC++ method with one time step (2 snapshots) reconstruct some high

velocity blobs along with the central low velocity structures. The contours again visually tend to improve with respect to the over all shape and resolution, with increasing time lengths. Again the similar trend is observed for the  $v$  velocity. There seems to be a slight overshoot of the velocity predictions in figure 7.9 (h), which can be attributed to the number of iterations allowed for the computation. When concerning the vorticity contours, more regularised blobs devoid of the local peaks is observed with VIC++ with long tracks.

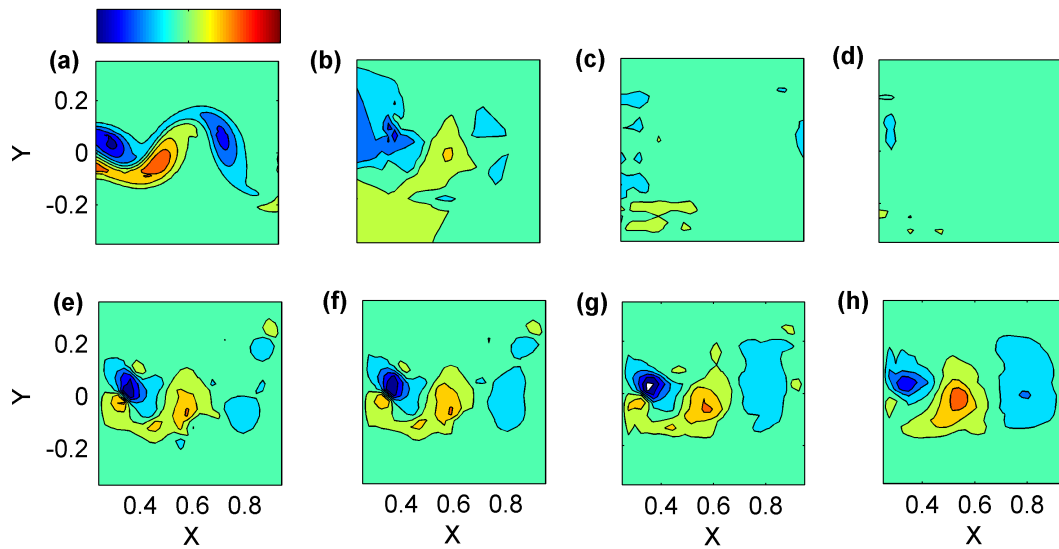


**Figure 7.10:** vorticity contours for 25 particles.. (a) Numerical (b) Linear Interpolation (c) PIV (d) AGW and (e) to (h) VIC++ for  $N_t = 2, 5, 10, 20$  respectively

For the quantitative analysis of the methods for the unsteady flow, the root means square (RMS) error of the velocity fields with respect to the reference velocity field is compute for 25 particles seeded in the flow. Table 7.2 presents the RMS error of the reconstructions of respective methods. It is observed that the RMS error of the linear interpolation method is highest followed by PIV, AGW and VIC++ method. For a better perspective all the methods are compared with the linear interpolation method. The error of PIV is around 7% lower than the linear interpolation while the AGW is 12% lower. On the other hand the VIC++ method with 2 snapshots displays significantly lower error, amounting to around 25% reduction with respect to the linear interpolation. VIC++ method incorporating longer tracks show further reduction of the error and hence the improvement of the reconstruction quality. VIC++ with 20 snapshots has almost 50% lower error than the linear interpolation.

**Table 7.2:** RMS error of different methods for 25 particles

Method	$\epsilon_{rms}$
Linear Interpolation	0.91
PIV	0.084
AGW	0.078
VIC++ $N_t = 2$	0.068
VIC++ $N_t = 10$	0.0572
VIC++ $N_t = 20$	0.0463

A comparison of the  $u$  velocity profiles along the the central x-axis ( $y=0$ ), for reconstruction of AGW method and VIC++ method is presented in figure 7.11. The black line represents the reference  $u$  velocity profile computed from the OpenFOAM simulations. The profile generated by the AGW method is shown in red colour while the VIC++ with  $N_t = 2$  and  $N_t = 20$  by green and blue respectively. The AGW method has been chosen for the comparison with VIC++ method in this case because it has the lowest error of the three conventional methods discussed above. It is observed that the velocity profile computed through AGW method hardly follows the reference velocity profile justifying the large RMS error observed above. The VIC++ method with 2 snapshots, follows the reference curve quite nicely in the first half of the domain but for later part deviates from the solution. The longer tracks used in the VIC++ with  $N_t = 20$ , enforces comparatively accurate profile throughout the domain. Still significant deviation is observed throught the domain. This can be mainly attributed to very low particle density(25 particle) utilised for the reconstruction.

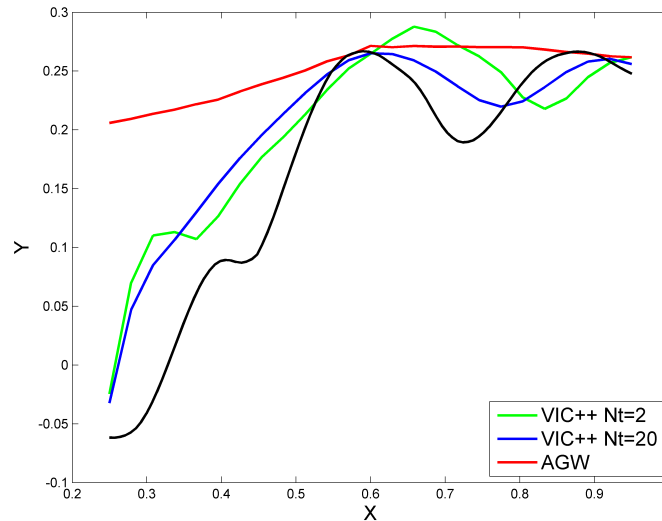


**Figure 7.11:** Mean  $u$  velocity profile along the x-axis (at  $y=0$ ) of AGW (red), VIC++  $N_t=2$  (green), VIC++  $N_t=20$  (blue) compared with the numerical solution (black). For 25 particles.

# Conclusions and Recommendations

A method has been proposed to increase spatial resolution of tomo-PIV in low seeding flows by incorporating full particle tracks using Vortex in Cell simulation. The proposed method is numerically implemented and validated using two synthetic test cases. The present section summarises the conclusion of the work done in this thesis. It is followed by the recommendations for future development of the method.

### 8.1 Conclusions

To understand the problem at hand the basic concepts of PIV are reviewed followed by the development of different methods, their limitations and the causes of those limitations. A literature survey on the state of the art processing techniques in PIV and PTV is done. Even though there exist some methods to increase spatial resolution of PIV and some on utilising the PTV tracks for getting super resolution in PIV, VIC+ method by Schneiders et al. (2015) is the only existing method specifically dealing with spatial resolution issues in low density experiments. VIC+ is a physics based method but does not incorporate the full temporal information available in the flow. It uses temporal information in the form of material derivative of velocity field. The present thesis investigates the idea that whether including more information by providing a velocity time series of the particles increases the spatial resolution of PIV generated flow field. It also investigates the effect of incorporating longer time horizon on the reconstruction of instantaneous flow field.

The VIC++ method is proposed which leverages the temporal information available in the Lagrangian particle tracks to increase the spatial resolution of Eulerian flow field. It uses full particle tracks available through the particle tracking algorithms (eg. 'shake the box' or tomo-PTV as reference). The PIV measurement data provides the initial condition to the problem as well as boundary conditions at all time instances. A gradient based optimisation problem is solved to minimise a cost function, ultimately resulting in computation of an optimised instantaneous flow field. The computation of gradient is done through the adjoint method

Validation of the method is done by creating a two dimensional synthetic test case of a translating vortex blob. Synthetic tracks are created acting as the reference velocity time

series. Velocity and vorticity fields are reconstructed from the particle distribution by using methods such as linear interpolation, AGW and approximate PIV. For the VIC++ method homogeneous padding type boundary conditions are used for the simulation. The reconstructed fields are highly sensitive to erroneous initial conditions. Hence zero initial conditions are used for the proposed method. The VIC++ with varying length of particle tracks ( $N_t = 2$  snapshots to 40 snapshots) are used for reconstructing the velocity and vorticity fields. All the methods are compared using qualitative as well as quantitative analyses. The qualitative investigation is done by comparing contour plots of instantaneous velocity and vorticity fields. This investigation is performed for very low seeding concentration by introducing only 10 particles in the flow. Inspecting the contour plots reveals that linear interpolation AGW and PIV completely fail to reconstruct any contours while the VIC++ method with 2 snapshots fares much better by reconstructing some contours with a regular shape, though some local peak do appear in the optimised field. Further contours appear and flow field becomes more regularised when using longer tracks. The mean  $u$  velocity profiles over 100 samples are compared for the linear interpolation and VIC++ with  $N_t = 2$ . It is observed that the VIC++ follows the analytical profile much better with low standard deviation indicating lower dependence on particle position. VIC++ also provides higher vorticity peak indicating that higher resolution is achieved. The profile introspection of the VIC++ short track and long tracks is also done which reveals that longer tracks produce much more accurate fields.

The quantitative analysis is performed by computing the root mean square error of the velocity fields with respect to the analytical case. The error is investigated for increasing particle densities. It is observed that the linear interpolation has lower error compared to AGW and PIV, which can be explained by the fact that the reference data is exact without any noise, also as the later two methods are based on averaging principles, for very low seeding they display large spatial filtering. The VIC++ method demonstrates lower error compared to the other methods. Increasing track lengths results in lower error values. For large seeding densities a flattening effect is observed which can be attributed to the finite grid size being used. This is proved by using larger and smaller grid size. For smaller grid size the flattening effect is more predominant. Another important observation is that the relative advantage gained with using longer tracks reduces over the time lengths. The computational cost increases with the longer time lengths which indicates that the selection of the length of time series to be used should be based on the accuracy desired, computational budget and the grid size.

Effect of noisy data on the reconstruction abilities of different methods is also investigated. It is found that even for very high seeding densities while other methods fail to significantly remove the noise, the physic-based approach of VIC++ method applying solenoidal filtering removes almost all the noise. With longer tracks the results are further enhanced.

An unsteady test case with evolving vortices is also used for validation of the method. Laminar Von-Karman vortex shedding ( $Re = 150$ ) due to flow over a long cylinder is investigated. The laminar case is specifically taken because it can be accurately represented by a two dimensional model. The analysis follows the same pattern as in the vortex blob case. The qualitative analysis clearly displays the superiority of the proposed method over the other methods by producing much better and regularised contours for even very low number of tracers (10 and 25). Longer tracks as in the previous case produce better

results. The RMS error for 25 particles is in accordance with the findings from the contour plots with the VIC++ using  $N_t = 2$  snapshots having 25% while  $N_t = 20$  having 50% lower error compared to linear interpolation .

Over all it can be concluded that the hypothesis concerning the improvement in instantaneous reconstruction by providing more temporal flow information is proven to be valid.

## 8.2 Recommendations for Future Work

The development of the technique has many aspects which can be explored in the future. Some of the recommendations for taking this work forward are discussed below.

The present work only explores the two dimensional realm due to the constraint on the thesis duration. The true application of the developed method is intended for the three dimensional domain and its extension to 3D is primarily recommended. This would enable experimental validation of the method using actual tomo-PIV and 3D PTV data. It should not be out of place to mention that when extending to 3D, a less expensive interpolation technique (such as CIC) is recommended to be used for the VIC simulations instead of the presently implemented  $M'_4$  interpolation technique.

The currently proposed method only uses the VIC time integration to march forward in time. Backward time integration can also be utilised to provide more robust solution by maintaining the temporal continuity between snapshots.

The viscous term was not incorporated in the present implementation due to the small time integrations considered. For temporally longer tracks the viscous dissipation can become more significant and hence assumption of inviscid flow may not be valid. It is thus advised to include the viscous term during the implementation of the VIC method.

The boundary conditions have not been sufficiently explored in the proposed method, rendering the reconstructions at the boundaries to largely rely on the information provided by tomo-PIV data. This aspect of the method can be studied in more detail for its potential improvement.



---

## References

- Abdolhosseini, R. & Milane, R. (1996). Prediction of growth of turbulence in a uniformly sheared flow using the vortex-in-cell method. *ESAIM Proc.*, *vo. 1*, pp. 387–400.
- Adrian, R. J. (1991). Particle imaging techniques for experimental fluid mechanics. *Annu. Rev. Fluid Mech.* *23* 261-304.
- Adrian, R. J. (1995). Limiting resolution of particle image velocimetry for turbulent flow. *Advances in Turbulence Research* pp 1–19.
- Adrian, R. J., Elsinga, G. E. & Westerweel, J. (2013). Particle image velocimetry for complex and turbulent flows. *Annu. Rev. Fluid Mech.* *45*:409–36.
- Agüí, J. C. & Jiménez, J. (1987). On the performance of particle tracking. *Journal of Fluid Mechanics*, *vol. 185*, pp. 447- 468.
- Amili, O., Atkinson, C. & Soria, J. (2009). Dhmpiv and tomo-piv measurements of three-dimensional structures in a turbulent boundary layer advances in turbulence. *Springer Proceedings in Physics vol 132, part 9*, pp 613–6.
- Arroyo, M. P. & Greated, C. A. (1991). Stereoscopic particle image velocimetry. *Meas. Sci. Technol.*, *vol. 2*, pp 1181–1186.
- Atkinson, C. H., Dillon-Gibbons, C. J., Herpin, S. & Soria, J. (2008). Reconstruction techniques for tomographic piv of a turbulent boundary layer. *14th Int. Symp. on Applications of Laser Techniques to Fluid Mechanics (Lisbon, Portugal)*.
- Azijli, I. & Dwight, R. (2015). Solenoidal filtering of volumetric velocity measurements using gaussian process regression. *Exp Fluids* *56*:198.
- Azijli, I., Dwight, R. P. & Bijl, H. (2014). Bayesian approach to physics-based reconstruction of incompressible flows. in: Numerical mathematics and advanced applications. *ENUMATH 2013, vol. 103* , pp. 529-536.
- Bernard, P. S. (1999). Turbulent flow modeling using a fast, parallel, vortex tube and sheet method. *ESAIM Proc.*, *vol. 7*, pp. 46-55.
- Birkhoff, G. & Fisher, J. (1959). Do vortex sheets roll up. *Circ. Mat. Palermo*, *vol. 8*, pp. 77-90.
- Burridge, D. & Temperton, C. (1979). A fast poisson-solver for large grids. *Journal Of Computational Physics*, *vol. 30*, pp. 145-148.

- Casa, L. D. C. & Krueger, P. S. (2013). Radial basis function interpolation of unstructured, three-dimensional, volumetric particle tracking velocimetry data. *Meas. Sci. Technol.*, vol. 24, 065304.
- Chorin, A. J. (1973). Numerical study of slightly viscous flow. *J. Fluid Mech.*, vol. 57, pp. 785-796.
- Chorin, A. J. & Bernard, P. S. (1973). Discretization of a vortex sheet with an example of roll up. *J. Comput. Phys.*, vol. 13, pp. 423-428.
- Christiansen, J. P. (1973). Numerical simulation of hydrodynamics by the method of point vortices. *Journal of Computational Physics*, vol. 13, pp.363-379.
- Corpetti, T., Heitz, D., Arroyo, G., Memin, E. & Santa-Cruz, A. (2005). Fluid experimental flow estimation based on an optical-flow scheme. *Exp. Fluids*, vol. 40: pp. 80-97.
- Cottet, G. H. & Koumoutsakos, P. (2000). *Vortex methods – theory and practice*. New York: Cambridge University Press.
- Cottet, G. H., Koumoutsakos, P. & Ould-Salihi, M. L. (2000). Vortex methods with spatially varying cores. *J. Comput. Phys.*, vol. 162, pp. 164,185.
- Cottet, G. H., Michaux, B., Ossia, S. & VanderLinden, G. (2002). A comparison of spectral and vortex methods in three-dimensional incompressible flows. *J. Comput. Phys.*, vol. 175, pp. 702-712.
- Couet, B., Buneman, O. & Leonard, A. (1981). Simulation of three-dimensional incompressible flows with a vortex-in-cell method. *J. Comput. Phys*, vol. 9, Issue 2, pp. 305-328.
- David, L., Jardin, T., Braud, P. & Farcy, A. (2011). Time-resolved scanning tomography piv measurements around a flapping wing. *Exp. Fluids*, vo. 52, Issue 4, pp. 857-864.
- de Kat, R. & van Oudheusden, B. W. (2012). Instantaneous planar pressure determination from piv in turbulent flow. *Exp. Fluids*, vol. 52, pp. 1089-1106.
- Elsinga, G. E., Scarano, F., Wieneke, B. & Oudheusden, B. W. V. (2006). Tomographic particle image velocimetry. *Experiments in Fluids* 41 933-947.
- Gao, Q., Ortiz-Duenas, C. & Longmire, E. K. (2010). Eddy structure in turbulent boundary layers based on tomographic piv. *15th Int. Symp. on Applications of Laser Techniques to Fluid Mechanics (Lisbon, Portugal)*.
- Ghaemi, S., Ragni, D. & Scarano, F. (2012). Piv-based pressure fluctuations in the turbulent boundary layer. *Exp. Fluids Volume 53, Issue 6, pp 1823-1840*.
- Ghaemi, S. & Scarano, F. (2010). Multi-pass light amplification for tomographic particle image velocimetry application. *Meas Sci Technol*, vol. 21, 127002.
- Greengard, L. & Rokhlin, V. (1987). A fast algorithm for particle simulations. *J. Comput. Phys.*, vol. 73, pp. 325-48.
- Gronskis, A., Heitz, D. & Memin, E. (2013). Inow and initial conditions for direct numerical simulation based on adjoint data assimilation. *Journal of Computational Physics*, vol. 242, pp. 480-497.
- Heine, B., Schanz, D., Schroeder, A., Dierksheide, U. & Raffel, M. (2011). Investigation of the wake of low aspect ratio cylinders by tomographic piv. *9th Int. Symp. PIV (Kobe, Japan)*.
- Hockney, R. W. (1970). The potential calculation and some applications in methods in computational physics. *Academic Press, New York* , Vol. 9, pp. 135-211.
- Humble, R. A., Elsinga, G. E., Scarano, F. & van Oudheusden, B. W. (2009). Three-dimensional instantaneous structure of a shock wave/turbulent boundary layer in-

- teraction. *J. Fluid Mech.*, vol. 622, pp. 33–62.
- Humphreys, W. M., Bartram, S. M. & Blackshire, J. L. (1993). A survey of particle image velocimetry applications in langley aerospace facilities. *Proc. 31st Aerospace Sciences Meeting 11-14 January, Reno, Nevada, (AIAA Paper 93-041)*.
- Keane, R. D., Adrian, R. J. & Zhang, Y. (1995). Super-resolution particle image velocimetry. *Meas. Sci. Technol.*, vol. 6, no. 6.
- Kudela, H. (1999). Application of the vortex-in-cell method for the simulation of two dimensional viscous flow. *TASK Quarterly*, vol. 3 no. 3 , pp. 343-360.
- Kudela, H. & Kosior, A. (2011). Modeling vortex rings dynamics with vortex in cell method. *Journal of Physics: Conference Series*, vol. 318, 062014.
- Kähler, C. J. & Kompenhans, J. (2000). Fundamentals of multiple plane stereo particle image velocimetry. *Experiments in Fluids*, Vol. 29, pp. S070-S077.
- Lemke, M. & Sesterhenn, J. (2013). Adjoint based pressure determination from piv-datavalidation with synthetic piv measurements. *10th International Symposium on Particle Image Velocimetry, Delft*.
- Leonard, A. (1980). Vortex methods for flow simulations. *Journal of Computational physics*, vol. 37, pp. 289-335.
- Liu, C. H. (2001). A three-dimensional vortex particle-in-cell method for vortex motions in the vicinity of a wall. *Int. J. Numer. Meth. Fluids*, vol. 37, pp. 501–523.
- Liu, D. & Nocedal, J. (1989). On the limited memory bfgs method for large scale optimization. *Mathematical Programming*, vol. 45, pp. 503-508.
- Lynch, K. & Scarano, F. (2012). Enhancing the velocity dynamic range and accuracy of time-resolved piv through fluid trajectory correlation. *16th Int Symp on Applications of Laser Techniques to Fluid Mechanics Lisbon, Portugal, 09-12 July*.
- Lynch, K. & Scarano, F. (2015). An efficient and accurate approach to mtemart for timeresolved tomographic piv. *Exp Fluids*, pp. 56=66.
- Malik, N. A., Dracos, T. & Papantoniou, D. A. (1993). Particle tracking velocimetry in three-dimensional flows. *Experiments in Fluids*, vol. 15, Issue 4, pp 279-294.
- Marta, A. C., Mader, C. A., Martins, J. R. R. A., der Weide, E. V. & Alonso, J. J. (2007). A methodology for the development of discrete adjoint solvers using automatic differentiation tools. *International Journal of Computational Fluid Dynamics*, Vol. 21, Issue 9-10.
- Meinhart, C. D., Prasad, A. K. & Adrian, R. J. (1993). A parallel digital processor system for particle image velocimetry. *Measurement Science and Technology*, vol. 4, pp. 619-626.
- Melling, A. (1997). Tracer particles and seeding for particle image velocimetry. *Meas. Sci. Technol.*, vol. 8, pp. 1406–1416.
- Melling, A. & Whitelaw, J. H. (1973). Seeding of gas flows for laser anemometry. *DISA Information*, vol. 15, pp. 5–14.
- Meynart, R. (1983). Instantaneous velocity field measurements in unsteady gas flow by speckle velocimetry. *Applied Optics*, vol. 22, no. 4: 535-40.
- Mohammadian, A. & Marshall, J. (2010). A “vortex in cell” model for quasi-geostrophic, shallow water dynamics on the sphere. *Ocean Modelling*, vol. 32, pp. 132–142.
- Monaghan, J. J. (1985). Particle methods for hydrodynamics. *J. Comput. Phys.*, vol. 3, pp. 71–123.
- Morghenthal, G. & Walther, J. H. (2007). An immersed interface method for the vortex-in-cell algorithm. *Computers and Structures*, vol. 85, pp. 712–726.

- Mullin, J. A. & Dahm, W. J. A. (2005). Dual-plane stereo particle image velocimetry (dspiv) for measuring velocity gradient fields at intermediate and small scales of turbulent flows. *Experiments in Fluids*, Vol. 38, pp. 185–196.
- Najm, H. N., B, M. R., Devine, K. D. & Kempa, S. N. (1999). A coupled lagrangian-eulerian scheme for reacting flow modeling. *ESAIM Proc.* vol. 7, pp. 304–313.
- Novara, M., Batenburg, K. J. & Scarano, F. (2010). Motion tracking-enhanced method for tomographic piv. *Meas. Sci. Technol.*, vol. 21, 035401(18pp).
- Novara, M. & Scarano, F. (2010). Performances of motion tracking enhanced tomo-piv on turbulent shear flows. *15th Int. Symp. on Applications of Laser Techniques to Fluid Mechanics (Lisbon, Portugal)*.
- Ploumhans, P., Winckelmans, G. S. & Salmon, J. K. (1999). Vortex particles and tree codes: I. flows with arbitrary crossing between solid boundaries and particle redistribution lattice; ii. vortex ring encountering a plane at an angle. *ESAIM Proc.*, vol. 7, pp. 335–348.
- Prasad, A. K. (2000). Stereoscopic particle image velocimetry. *Experiments in Fluids*, Vol. 29, pp. 103–116.
- Prasad, A. K. & Adrian, R. J. (1993). Stereoscopic particle image velocimetry applied to liquid flows. *Experiments in Fluids*, Vol. 15, pp. 49–60.
- Raffel, M., Willert, C. E., Wereley, S. T. & Kompenhans, J. (2007). Particle image velocimetry – a practical guide. *Springer, New York, 2nd edition*.
- Rajani, B. N., Kandasamy, A. & Majumdar, S. (1997). Numerical simulation of laminar flow past a circular cylinder. *Applied Mathematical Modelling*, vol. 33, pp. 1228–1247.
- Ribeiro, R. S. & Kroo, I. (1995). Vortex-in-cell analysis of wing wake roll-up. *Journal of aircraft*, vol. 32, 5.
- Rosenhead, L. (1931). The formation of vortices from a surface of discontinuity. *Proceedings of the Royal Society A: Mathematical, Physical and Engineering Sciences*, pp. 134–170.
- Ruhnau, P., Stahl, A. & Schnorr, C. (2007). Variational estimation of experimental fluid flows with physics-based spatio-temporal regularization. *Measurement Science and Technology*, vol. 18, no. 3.
- Savoie, R., Gagnon, Y., Ossia, S. & Mercadier, Y. (1996). Numerical simulation of the starting flow down a step. *ESAIM Proc.*, vol. 1, pp. 377–386.
- Scarano, F. (2003). Theory of non-isotropic spatial resolution in piv. *Experiments in Fluids*, vol. 35, issue 3, pp. 268–277.
- Scarano, F. (2013a). Experimental aerodynamics. *TU Delft Reader, Course AE4-180*.
- Scarano, F. (2013b). Tomographic piv : principles and practice. *Meas. Sci. Technol.* 24, 012001 (28pp).
- Scarano, F., Bryon, K. & Violato, D. (2010). Time-resolved analysis of circular and chevron jets transition by tomo-piv. *15th Int. Symp. on Applications of Laser Techniques to Fluid Mechanics (Lisbon, Portugal)*.
- Scarano, F., Ghaemi, S., Caridi, G. S. A., Bosbach, J., Dierksheide, U. & Sciacchitano, A. (2015). On the use of helium-filled soap bubbles for large-scale tomographic piv in wind tunnel experiments. *Exp Fluids*, 56:42.
- Scarano, F. & Poelma, C. (2009). Three-dimensional vorticity patterns of cylinder wakes. *Exp. Fluids*, vol. 47, 69–83.

- Schanz, D., Schröder, A. & Gesemann, S. (2014). ‘shake the box’ - a 4d ptv algorithm: Accurate and ghostless reconstruction of lagrangian tracks in densely seeded flows. *17th International Symposium on Applications of Laser Techniques to Fluid Mechanics Lisbon, Portugal*.
- Schmid, P. J., Violato, D. & Scarano, F. (2012). Decomposition of time-resolved tomographic piv. *Exp. Fluids, vol 52, Issue 6, pp. 1567-1579*.
- Schneiders, J. F. G. (2014). Time-supersampling 3d-piv measurements by vortex-in-cell simulation. *TU Delft Repository*.
- Schneiders, J. F. G., Azijli, I., Scarano, F. & Dwight, R. P. (2015). Pouring time into space. *11TH International Symposium On Particle Image Velocimetry – PIV15 Santa Barbara, California*.
- Schneiders, J. F. G., Dwight, R. P. & Scarano, F. (2014). Time-supersampling of 3d-piv measurements with vortex-in-cell simulation. *Exp Fluids, 55:1692*.
- Schneiders, J. F. G., Pröbsting, S., Dwight, R., van Oudheusden, B. W. & Scarano, F. (2016a). Pressure estimation from single snapshot tomographic piv in a turbulent boundary layer. *Experiments in Fluids, 57:53*.
- Schneiders, J. F. G., Singh, P. & Scarano, F. (2016b). Instantaneous flow reconstruction from particle trajectories with vortex-in-cell. *18th International Symposium on the Application of Laser and Imaging Techniques o Fluid Mechanics. Lisbon, Portugal. July 4-7*.
- Sciacchitano, A. (2014). Uncertainty quantification in particle image velocimetry and advances in time-resolved image and data analysis, phd thesis. *TU Delft Repository*.
- Sciacchitano, A., Caridi, G. C. A. & Scarano, F. (2015). A quantitative flow visualization technique for on-site sport aerodynamics optimization. *7th Asia-Pacific Congress on Sports Technology, APCST*.
- Sciacchitano, A., Dwight, R. P. & Scarano, F. (2012). Navier stokes simulations in gappy piv data. *Experiments in Fluids, vol. 53, pp. 1421-1435*.
- Sitou, A. & Riethmuller, M. L. (2001). Extension of piv to super resolution using ptv. *Meas. Sci. Technol., vol. 12, no. 9*.
- Stüer, H. & Blaser, S. (2000). Interpolation of scattered 3d ptv data to a regular grid. *Flow, Turbulence and Combustion, vol. 64, pp. 215-232*.
- Sumer, B. M. & Fredsøe, J. (1997). Hydrodynamics around cylindrical structures. *World Scientific Publishing Co. Pte. Ltd.*
- Theunissen, R., Scarano, F. & Riethmuller, M. L. (2007). An adaptive sampling and windowing interrogation method in piv. *Meas. Sci. Technol., vol. 18, pp. 275-287*.
- Tryggvason, G. (1989). Simulation of vortex sheet roll-up by vortex methods. *J. Comput. Phys., vo. 80, pp. 1-16.*
- Uchiyama, T. & Yoshii, Y. (2015). Numerical simulation of bubbly flow by vortex in cell method. *Procedia IUTAM, vol. 18, pp. 138-147*.
- Uchiyama, T., Yoshii, Y. & Hamada, H. (2014). Direct numerical simulation of a turbulent channel flow by an improved vortex in cell method. *International Journal of Numerical Methods for Heat Fluid Flow, vol. 24, Issue 1, pp. 103-123*.
- Vedula, P. & Adrian, R. J. (2005). Optimal solenoidal interpolation of turbulent vector fields: application to ptv and super-resolution piv. *Exp. Fluids, vol. 39, pp. 213-221*.
- Violato, D. & Scarano, F. (2011). Three-dimensional evolution of flow structures in transitional circular and chevron jets. *Phys. Fluids, vo. 23, 124104*.

- Vlasenko, A. & Schnörr, C. (2008). Physically consistent variational denoising of image fluid flow estimate. *Proc. Pattern Recognition 30th DAGM Symp.*
- Vlasenko, A. & Schnörr, C. (2010). Physically consistent and efficient variational denoising of image fluid flow estimates. *IEEE Transactions On Image Processing*, vol. 19, no. 3.
- Vlasenko, A., Steele, E. C. C. & Nimmo-Smith, W. A. M. (2015). A physics-enabled flow restoration algorithm for sparse piv and ptv measurements. *Meas. Sci. Technology*, vol. 26, 065301.
- Westerweel, J. (1997). Fundamentals of digital particle image velocimetry. *Meas. Sci. Technol.* 8: 1379-1392.
- Wieneke, B. (2012). Iterative reconstruction of volumetric particle distribution. *Meas. Sci. Technol.*, vol. 24, 024008.
- Wieneke, B. & Pfeiffer, K. (2010). Adaptive piv with variable interrogation window size and shape. *15th Int Symp on Applications of Laser Techniques to Fluid Mechanics*.
- Willert, C. (1997). Stereoscopic digital particle image velocimetry for application in wind tunnel flows. *Meas. Sci. Technol.*, vol. 8, pp. 1465-1479.
- Williamson, C. H. K. (1989). Oblique and parallel modes of vortex shedding in the wake of a circular cylinder at low reynolds numbers. *J. Fluid Mech.*, vol. 206, pp. 579-627.
- Worth, N. A. & Nickels, T. B. (2008). Acceleration of tomo-piv by estimating the initial volume intensity distribution. *Exp. Fluids*, vol. 45, pp. 847-56.
- Yegavian, R., Leclaire, B., Champagnat, F. & Marquet, O. (2015). Performance assessment of piv super-resolution with adjoint-based data assimilation. *11TH International Symposium On Particle Image Velocimetry - PIV15, At Santa Barbara, California, USA*.
- Zdravkovich, M. (1997). Flow around circular cylinders. *Oxford Science Publication*, vol. 1.